



FRIEDRICH-SCHILLER- UNIVERSITÄT JENA

Crystallographic Influences on the Nanomanipulation of Gold Nanoclusters on Molybdenum Disulfide

Dissertation zur Erlangung des akademischen Grades

Doctor rerum naturalium (Dr. rer. nat.)

vorgelegt dem Rat der Physikalisch-Astronomischen Fakultät der Friedrich-Schiller-
Universität Jena von

Dipl.-Min. Felix Cassin

Geboren am 13.03.1989 in Gera

Betreuer

Prof. Enrico Gnecco

Otto-Schott-Institut für Materialforschung, Friedrich-Schiller-Universität Jena

Gutachter

1. Prof. Dr. Enrico GNECCO, Jena
2. Dr. Dirk Dietzel, Göttingen
3. Prof. Dr. Carsten Ronning, Jena

Tag der Disputation: 26.01.2021

For my wife, my parents and Hazelene

Abstract

With the invention of the atomic force microscopy (AFM) a whole new field of science developed to study the mechanical workings of friction on the nanoscale. For the last years one main focus of the nanotribology community is the manipulation of nano-objects to create structures for applications ranging from biosensors to nano-optoelectronics. For this, the formation of nano- to micrometer large individual gold nanostructures on crystalline surfaces is an important steppingstone.

This work investigates the manipulation behavior of thermally deposited gold nanoclusters with tens of nanometers in size on monocrystalline Molybdenum Disulfide (MoS_2) surfaces. Using scan raster patterns in the order of several μm , dozens of Au islands can be displaced with a single scan, revealing a directional locking effect caused by the epitaxial nature of the nanoparticle growth on the MoS_2 surface. Statistical analysis of tapping mode manipulation scans using pyramidal and conical AFM tips along with MD simulations lead to the conclusion that frictional anisotropy governs the direction of displacement, with the preference to move along the zigzag- or armchair direction of the hexagonally structured surface.

Chemical vapor deposition (CVD) grown monolayer and bilayer MoS_2 on Si/SiO₂ wafer as a substrate for Au island manipulation in contact mode not only shows the same directional locking phenomenon but also exhibits the formation of striation of gold nanoparticles when the critical width of displaced material along the y direction is reached and further manipulation prevented. Gold crystals forming these μm long strips show a spacing of around 1 nm between the nanoparticles, prohibiting the fusion of Au islands into a single gold nanowire through re-annealing with temperatures up to 700 °C.

Surface modification through nanoscratches of around 40 nm in width with a single crystal diamond tip is explored to understand the influence on the formation of gold nanostructures. Again, the crystallographic direction of the modified material must be considered when scratching bulk or monolayer MoS_2 . While the surface damage due to scratches along armchair- or zigzag direction appears to be minimal, providing stopping points for agglomeration of Au islands, other directions of scratches show nanoexfoliation and wrinkling of the surface for monolayer and bulk material.

Zusammenfassung

Mit der Erfindung des Rasterkraftmikroskops (AFM) öffnete sich ein neues Feld der Wissenschaft zur Untersuchung mechanischer Effekte von Reibung im Nanobereich. In den letzten Jahren legte die Forschungsgemeinschaft rund um Nanotribologie einen Fokus auf die Manipulation von Nanoobjekten zur Kreation von Strukturen nützlich für Nanotechnologie, von Biosensoren bis Nanooptoelektronik reichend. Für dieses Ziel ist die Bildung von nano- bis mikrometergroßen individuellen Goldstrukturen auf Kristalloberflächen ein wichtiger Schritt.

Diese Arbeit beschäftigt sich mit dem Manipulationsverhalten von thermal gewachsenen Goldnanokristallen auf monokristallinen Molybdändisulfid (MoS_2). Mittels großen Scanrastern in der Größenordnung von mehreren μm können dutzende Goldnanopartikel in einem Scan bewegt werden, was wiederum den „*directional locking*“ Effekt zum Vorschein bringt, verursacht durch die epitaxiale Beziehung beim Wachstum der Nanopartikel auf der MoS_2 Oberfläche. Die statistische Auswertung von Tapping Mode Manipulationssequenzen mittels pyramidalen und konischen AFM-Spitzen, kombiniert mit MD Simulationen, führt zu der Schlussfolgerung, dass die Reibungsanisotropie kristalliner Oberfläche die Bewegungsrichtung bestimmt, mit Bevorzugung der Hauptkristallrichtungen.

CVD gewachsene MoS_2 Mono- und Doppellagen mit aufgewachsenen Goldkristallen zeigen im Contact Mode den gleichen „*directional locking*“ Effekt, aber zusätzlich tritt eine Streifenbildung von Goldnanopartikeln auf, nachdem eine kritische Breite von manipulierten Material entlang der y Richtung erreicht ist. Dies sorgt für Abstände von ca. 1 nm zwischen den Nanokristallen, wodurch die Fusion von der Partikel durch Erhitzen mit Temperaturen bis zu $700\text{ }^\circ\text{C}$ zu einem mikrometerlangen Nanodraht verhindert wird.

Die Oberflächenmodifikation mittels Nanokratzen mit Breiten um die 40 nm durch eine einkristalline Diamantspitze bietet eine Möglichkeit diese Probleme zu umgehen. Unter Beachtung der Kristallrichtung des mehr- oder monolagigen MoS_2 können Kratzer die Oberfläche modifizieren und einen Ankerpunkt für die Bildung von Agglomerationen von Goldkristallen bilden.

Contents

1	Introduction.....	3
2	Concepts and Models of Nanotribology	6
2.1	Prandtl-Tomlinson Model.....	6
2.2	Friction Dependence on Contact Area	8
2.3	Contact Aging and Static Friction	9
3	Basic Principles of the AFM	10
3.1	History of the AFM.....	10
3.2	Basic Principles of Operation.....	12
3.3	Calibration Methods	16
3.4	Contact Mode Measurements.....	18
3.4.1	Normal Force Measurements	20
3.4.2	Lateral Force Measurements	21
3.5	Tapping Mode Measurements	22
4	Concepts of Nanomanipulation	23
4.1	Manipulation in Contact Mode	26
4.2	Manipulation in Tapping Mode	27
4.3	Manipulation in Quantitative Imaging-Mode (QI)	28
5	Materials.....	29
5.1	Molybdenum Disulfide (MoS_2)	29
5.1.1	Growth of Monolayer and Bilayer MoS_2	32
5.2	Gold Nanoparticle Growth on Bulk MoS_2	35
5.3	Gold Nanoparticle Growth on Monolayer and Bilayer MoS_2	39
6	Gold Nanoparticle Manipulation.....	43
6.1	Nanomanipulation of Au islands on bulk MoS_2	44
6.2	Theoretical Investigations and Simulations of the Au Island Pathways.....	53
6.3	Nanomanipulation on Monolayer and Bilayer MoS_2	57
7	Gold Nanowire Formation.....	63
7.1	Re-Annealing of Manipulated Au Islands	63
7.2	Nanoscratch-based Surface Modification	64
7.3	Au Island Manipulation on Patterned MoS_2	69
8	Discussion	74

9	Conclusion and Outlook	77
	List of Figures.....	79
	List of Tables.....	82
	Bibliography.....	82
	Acknowledgements	90
	Eigenwörtliche Erklärung	91

1 Introduction

Throughout the history of mankind friction played a major role in the understanding of the physical world around us and the development of technologies from the ancient civilizations to the postmodern global society nowadays. Even most basic tasks, such as walking, holding objects or tactile sensing, are fundamentally based on the existence of friction [1], [2]. The Greek statesman and philosopher Themistius is one of the first known people to have studied friction in an academic fashion by stating that “it is easier to further the motion of a moving body than to move a body at rest” [3], [4]. Other philosophers were also interested in the function of friction, such as Aristotle, Pliny the Elder or Vitruvius [1].

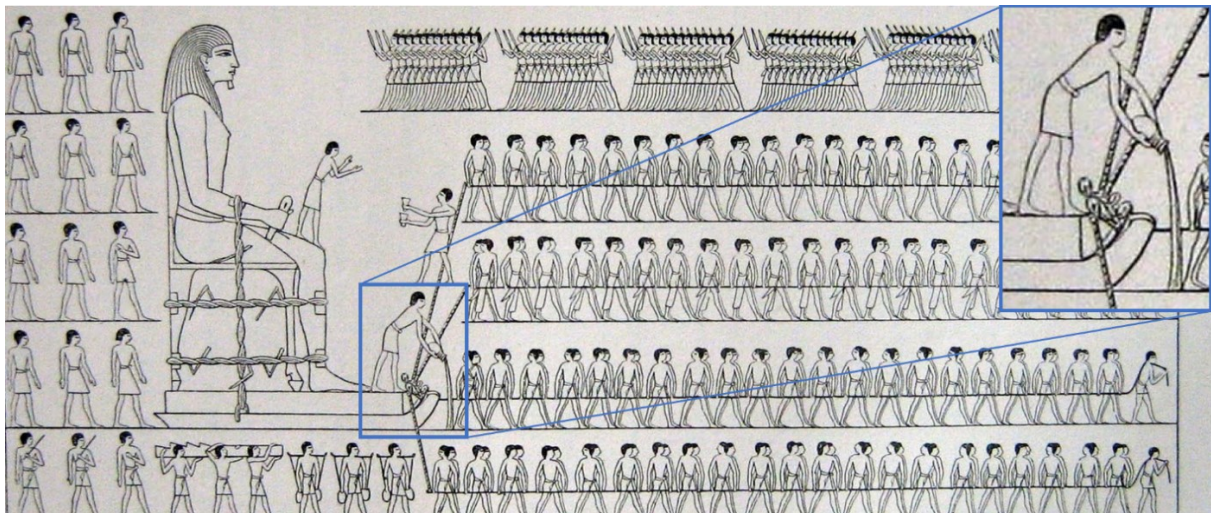


Figure 1: Egyptians pulling a statue on a wooden sled. One worker pours water in front of it to lubricate the sand (close-up). After a photograph of a painting in the tomb of Djehutihotep from Newberry et al. (1894) [5]

A good indicator of humanity’s understanding and manipulation of friction forces by humanity is a wall painting from the tomb of Djehutihotep where a massive statue is transported with a wooden sleigh. By watering the sand underneath the friction force can be significantly reduced, which can be also proven with modern friction experiments as done by Liefferink et al. [6] measuring the minimum pulling force and the maximum in penetration hardness of the sand water mixture at around 10% water volume fraction.

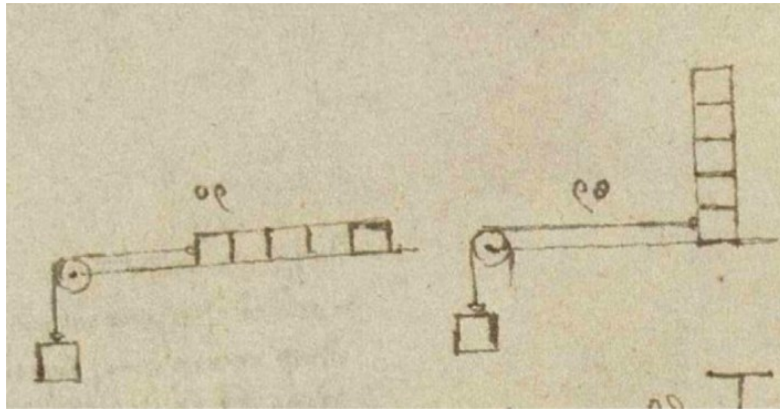


Figure 2: A sketch by Leonardo Da Vinci illustrating the relationship between contact area and normal load (Madrid I 173v, c. 1493–7, Biblioteca Nacional, Madrid) [7]

The first recorded methodical study of friction was done by Leonardo da Vinci (1459-1519) [8] who studied the topic extensively for over 20 years. He observed the effects of friction of different surfaces and materials, lubrication with help of mechanical systems and simple measurement systems to varying success. He understood important connections of the most important factors defining friction experienced by bodies and was able to translate this knowledge into model sketches and simple calculations, which makes him to a pioneer in the field of tribology.

However, these findings remained unpublished for centuries until Guillaume Amontons rediscovered them with his own experiments in 1699 [9]. Amontons was able to formulate two out of three laws of dry friction, which are:

- The force of friction is directly proportional to the applied load.
- The force of friction is independent of the apparent area of contact [9].

Later in the second half of the 18th century Charles Augustin de Coulomb (1736 – 1806) discovered the third law of dry friction which states:

- Kinetic friction is independent of the sliding velocity.

These discoveries gave an insight view how friction works but puzzled many scientists for the next centuries due to the limitations of the technology and scientific method of the time. Since only macroscopic experiments were possible, many effects like adhesion force between surfaces, surface roughness, frictional anisotropy and surface elasticity were not understood [10]. In (post)modern times friction is considered the main mechanism responsible for energy dissipation [1]. A third of the fuel energy produced by a car is lost due to friction between

moving parts and air resistance, 32% of the energy needed to produce paper is transformed into friction [11]. Nowadays it is estimated that ~23% of the worldwide energy consumption originates from tribological contacts, whereas 20% are used to overcome friction and 3% to remanufacture worn parts or wear-related failures [12].

The scientific field of friction on the nanoscale, called nanotribology, becomes of greater and greater interest for technological advancements in the last decade. With electronic devices steadily decreasing in size while simultaneously becoming more powerful, the need of understanding and manipulating frictional effects on micro- and nanoelectronics and their production inspires new research into the creation of nanowires. The standard procedure for the production of nanoscale electrodes has been electron beam lithography (EBL) [13–15] developed in the 1960s [16]. Here, a polymer mask is deposited onto the sample surface and with the help of a computer-controlled focused electron beam a custom circuit can be drawn onto the surface by cracking the polymer chains. Afterwards the marked regions are exposed to an organic solvent removing the mask. Finally, a layer of metal is deposited on the now exposed areas and the rest of the mask is detached from the sample. While this method provides a tool for the creation of nano circuits it comes with the cost of an expensive computer-controlled SEM, the exposure of the sample to UHV and chemical agents potentially harmful to nano objects and the inability to modify circuits after deposition.

This work attempts a different method of the creation of gold nanowires by utilizing the growth of geometrically defined crystalline gold nanoparticles onto the surface of the transition metal dichalcogenide Molybdenum Disulfide (MoS_2), a dry lubricant known for its low friction, robustness and semiconductor properties. Firstly, the growth behavior of the gold islands will be discussed with a strong focus on the crystallographic properties and the relation to the substrate. Equipped with the understanding of the Au- MoS_2 setup, systematic nanomanipulation sequences with varying displacement direction in regard to the crystal orientation will give an insight in the frictional behavior during manipulation of dozens of nano objects at the same time. Since two-dimensional materials become increasingly important in applications such as photovoltaics, water purification and especially semiconductors, synthetic monolayer and bilayer MoS_2 will be included as a substrate for Au island deposition with the aim to study the influence of 2D-specific phenomena on the manipulation and formation of gold structures. Lastly, first steps into surface modification via nanoscratching

will provide an insight into future solutions to obstacles uncovered along the process of the creation of nanostructures with the help of manipulation of gold nanocrystals on MoS₂.

2 Concepts and Models of Nanotribology

2.1 Prandtl-Tomlinson Model

This model is used as the basis for many investigations of atomic scale friction mechanics in the field of nanotribology. Contrary to the widespread belief, this model was introduced by Ludwig Prandtl in 1928 and not by Tomlinson [17], however the name is kept for historical reasons. Prandtl described the arising friction produced by a single asperity contact in a dry environment after suggesting this simplified model for describing the plastic deformation in crystals. In this Prandtl considered only the one-dimensional movement of a point of mass attached to a spring being dragged over a corrugated surface with a constant velocity. The mathematical description of the PT model contains a sinusoidal periodic surface potential $V_{surface}$ with a corrugation amplitude V_0 and a tip at position x . The tip itself is connected elastically to a support with the with spring constant k , which is dragged across the periodic surface potential with the relative velocity v [18].

$$V_{PT} = V_{surface} + V_{spring},$$

where the $V_{surface}$ is
$$= \frac{V_0}{2} \sin\left(\frac{2\pi x}{a}\right),$$

and V_{spring} is
$$= \frac{1}{2}k(x - vt)^2.$$

The corresponding equation of motion reads

$$\begin{aligned} Mx'' &= -\eta x' - \frac{\partial V_{PT}}{\partial x} \\ &= -\eta x' - \frac{V_0\pi}{a} \cos\left(\frac{2\pi x}{a}\right) - k(x - vt), \end{aligned}$$

where M is defined as the tip mass and η as the viscous damping constant. Most of the time the tip is located in one of the local potential minima, but for finite v every minimum

disappears eventually. The tip position x^* where the local minimum vanishes can be determined by following equation

$$\frac{\delta^2}{\delta x^2} V_{PT} = 0$$

With the solution [19]:

$$x^* = \frac{a}{2\pi} \arccos\left(-\frac{1}{\xi}\right),$$

where the parameter ξ is defined as

$$\xi = \frac{2\pi^2 V_0}{ka^2}$$

Thu, this parameter depends on the ratio of spring stiffness and the surface potential corrugation for a given periodicity a . If $\xi < 1$ only one local minimum exists at all times and therefore the tip follows a continuous trajectory. For $\xi > 1$ multiple minima can exist at the same time. This makes the tip perform a *stick-slip* motion where the tip gets stuck in a local minimum and the energy barrier prevents another slip, similar to $k_B * T$ where k_B is the Boltzmann constant and T the temperature. Afterwards the tip moves to the next local minimum repeating the aforementioned process again. During this discontinuous movement energy is dissipated due to the viscous damping term during the high-velocity slip phase.

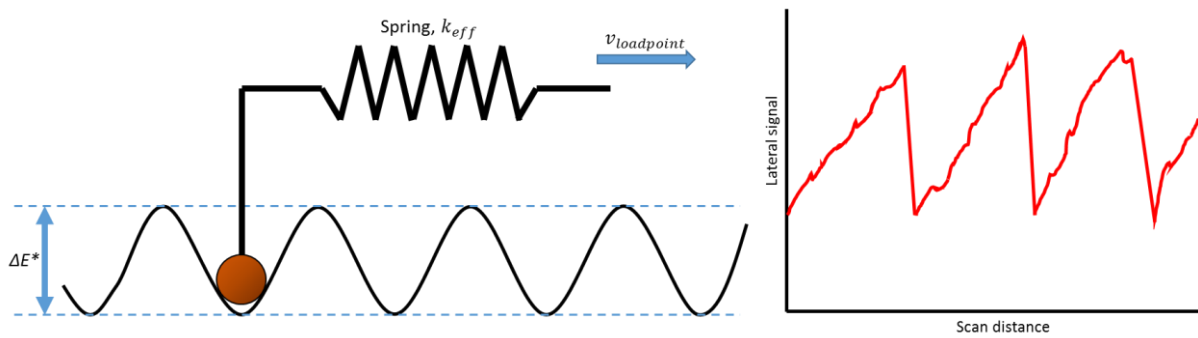


Figure 3: Prandtl-Tomlinson model. The tip is attached to a spring with the stiffness k_{eff} and is being dragged over a periodic surface potential. The tip is stuck in the local potential well until the spring force increases enough to induce a jump to a higher potential. Once the barrier height of a single potential well ΔE^* is overcome the tip jumps to the next local potential energy minimum. The resulting lateral deflection signal is in a so-called hacksaw tooth pattern typical for stick-slip phenomenon (right side)

Bowden et al. [20] first described the phenomenon of stick-slip motion in dry friction on many different scales, ranging from atomic friction, creation of sound in violin play to earthquakes [19], [21]. Depending on ξ and η the tip can jump over multiple minima, as investigated by Gnecco et al. [22] with help of systematic calculations with fitting measurements by [23]. Since the PT model is not specific about the channels of energy dissipation and simply modeled as viscous dissipation somewhat like a dashpot. The actual physical loss of energy could be permitted over phononic and on conductive materials electronic dissipation channels [24].

2.2 Friction Dependence on Contact Area

On a macroscopic level friction does not depend on the nominal area of contact but linearly on the normal load, which is stated in Amontons law. A very different picture is presented of the real contact area, where contact spots can be in the nm² regime. Bowden et al. [25] has shown that there is a mostly linear scaling of friction and the contact area A_n , which is only a small fraction of the macroscopic contact area A_m due to surface roughness. It is created by asperities of the contact surfaces and represents atomically smooth contacts. In recent times there is the consideration that A_n might not reflect the true contact size of the interfaces. Instead only a small fraction of atoms of both surfaces form covalent bonds and contribute to the surface interaction [26–28]. The same complexity is assumed for van-der-Waals-bound interfaces and its corresponding contact area.

Both experiments and theories have shown that the contact area on the nano level A_n of a macroscopically rough surface pressing into a flat surface correlates linearly with the applied normal load F_N [29]. The Greenwood-Williamson model [30] considers a multi-asperity contact with each individual elastic asperity cap are of equal curvature and also shows a Gaussian distribution of height. By applying elastic contact mechanics, the asperity contact mechanics are tractable, proposed by Heinrich Hertz [31]. These contacts resemble an elastic sphere in contact with an elastic half space. Ignoring adhesion effects this single contact point yields the relation of $A_n^{(i)} \propto F_N^{2/3}$. For the whole contact the uneven distribution of normal loads onto different asperities approximate to a linear relation of $A_n \propto F_N$. Persson was able to prove mathematically that this is expected for all surfaces no matter the roughness, if forces do not exceed a certain point. AFM tips also can be modeled by a single Hertzian contact when in

contact with a flat surface. Although the contact area $A_n^{(i)}$ is not linear with F_N , the friction force F_F is proportional to F_N for amorphous tips [32]. Mo et al. [33] demonstrated the linear correlation of the atomic contact area A_a and the applied load of an amorphous carbon tip on a diamond sample using MD simulations, where A_a represents the number of atomic bonds in the interface. This was supported by quantized heat transport measurements of AFM tips by Gotsmann et al. [27].

2.3 Contact Aging and Static Friction

Static friction is a phenomenon observed when a contact between two interfaces is kept for an extended amount of time. A large scale interface exhibits multiple true contact points in which these asperities experience a broad range of complex physical-chemical interactions including bond-forming [28], [34], capillarity [35] and plastic flow [36]. To initiate sliding, the force F_S is usually larger than the kinetic friction force F_F during relative motion. On larger scales static friction is commonly observed [24] and believed to be an integral part of the dynamics of earthquakes [21]. The effect of static friction is not of binary nature but develops gradually over the hold time t_{ht} of a stationary counter-body on a surface. This build-up of static friction and the dependency of time can be easily observed by initiation of sliding after a range of hold times to measure $F_S(t_{ht})$. The first investigations of this effect were done by Charles-Augustin de Coulomb, when he measured friction between two with tallow lubricated oak boards and explained the time-dependent increase of F_S with the gradual interlocking of wood fibers of the two boards in contact¹. The power law behind static friction can therefore be described with

$$F_S(t_{ht}) = K_1 + K_2 \times t_{ht}^{0.2}$$

The contact aging effect and its increase in friction was also observed in interfaces between rocks by Ruina [37] and Scholz [21] and described in an exemplary formulation of a rate-and-state theory [38] as:

$$\mu(v, \phi) = \mu_0 + B \ln\left(\frac{\phi}{\phi_0}\right) + A \ln\left(\frac{v}{v_0}\right),$$

where $\mu = F_F / F_N$ is the friction coefficient, v is the relative velocity and ϕ is a state variable, which shows the contact aging development since the previous slip. A , B and μ_0 represent

phenomenological fit parameters, while φ_0 and ν_0 are reference constants. When $\nu = 0$ the theory predicts a logarithmic increase of static friction over hold time. For systems with stick-slip type kinetic or static friction contact aging can have a significant influence on the overall observed friction, as stated by Persson [24]. Similar to contacts at larger length scales, a single asperity contact and the associated contact aging lead to an increase in static friction with the logarithm of the hold time t_{ht} [39]. However, over time two processes attribute to contact aging. Quantitative aging represents an increase in contact area while qualitative aging describes the strengthening of the already developed contacts through interfacial bonding. MD simulations and accompanying FFM measurements by Vorholzer et al. [40] emphasizes the utilization of the lateral contact stiffness k as a marker for contact aging compared to static friction.

3 Basic Principles of the AFM

3.1 History of the AFM

First modern experimental work in the field of nanotribology was made possible with the invention of the Surface Force Apparatus (SFA) by Tabor and Winterton in 1969, which was used to measure van der Waals forces between two smooth mica surfaces [41]. Two cylinders placed perpendicular to each other are approached and the forces exerted on surface interface are being measured while both surfaces move with respect to each other. In 1981 Binnig and Rohrer developed the Scanning tunneling microscope (STM) [42], which was awarded with the Nobel Prize of Physics in 1986 together with the invention of the first electron microscope by Ernst Ruska. The main principle behind the STM is the tunneling effect, where an electron flow is achieved between two conductive surfaces by keeping a constant voltage between the substrate surface and a tip made from tungsten or platinum. With the help of a scan pattern this method is able to produce topographic maps of conductive surfaces up to the sub-nanometer scale.

The Atomic Force Microscope was first introduced by Binnig, Gerber and Quate in 1986 [43] building on the STM as a measurement of the motion of a cantilever beam of ultra-small mass

while also monitoring the elastic deformations of the cantilever as a measurement of force. In the first iteration of this new microscope a diamond tip was fixed onto a piece of gold foil as a cantilever beam. When brought in contact with the AFM sample any force acting upon the foil and the inherent elastic deformations was monitored by an STM sitting above the tip position. A closed feedback loop system keeps the normal force at a constant level. Key factor for sensitive measurements in the nano Newton regime is the stiffness and mass of the cantilever acting as a spring

$$f_0 = (1/2\pi)(k/m_0)^{1/2},$$

where k is the spring constant and m_0 the mass that loads the spring. This leads to the revelation that a cantilever beam for precise measurements in the nanoregime requires a large k/m_0 ratio to soften the spring to become sensitive enough to even the most minimal changes in forces. Nowadays, commercial AFMs deploy a different method of measuring the bending and twisting of the tip. A laser beam is focused on the cantilever which then is reflected onto a position sensitive detector that records changes in the laser position in x- and y-axis.

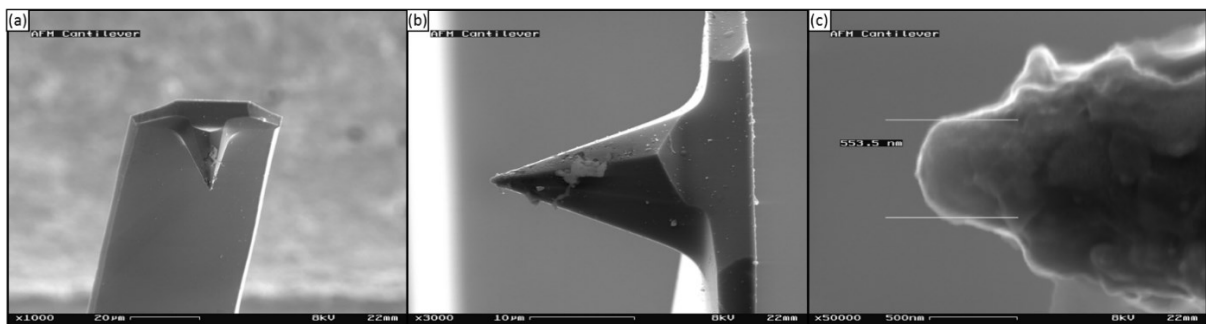


Figure 4: (a) modern cantilever with tip under the SEM (b) used pyramidal tip (c) close-up of a used tip with a diameter of 553 nm; By SecretDisc – own work, CC BY-SA 3.0 [44]

Modern commercial cantilevers are usually made of Si wafers using etching techniques to shape length, width, thickness of the cantilever beam and, in addition, sharpen the tip from generic 10 to 15 nm in radius and up to 3 nm for ultra-sharp tips. A coating of gold or aluminum on the opposite cantilever face increases the reflectivity of the laser beam and therefore increases the signal amplitude obtained by the PSD.

With the invention of the Friction Force Microscope (FFM) in 1987 by Mate et al. [19] scientists were finally able to study the properties of friction on true nanoscale which led to the

emergence of the field of Nanotribology. In Mates original work the instrument operated on similar principles as the AFM but utilized a fixed tungsten wire with an etched tip point of around 300 nm. Once brought in contact sample then was moved in a scan raster in x- and y-axis while the change in intensity of the reflected light from the tungsten tip was being recorded. Since friction in general is very sensitive to changes in geometry and interface composition it becomes imperative to work with very defined samples on nanoscale areas to avoid multi-asperity contacts, wear or contamination. The FFM then can achieve single-asperity contacts, where a tip is moved across the substrate sample. Unlike the AFM, this method not only measures the bending deflection of the cantilever but also the torsional twisting which is caused by friction forces acting upon the tip in the lateral direction. One of the most important results obtained with this instrument is the observation of stick-slip behavior of atomic scale friction where the tip gets stuck on single atoms until the spring stiffness of the cantilever equals the local slope of the surface potential of the atomically smooth surface [45], as explained in chapter 2.1. This tool is not only useful for determining lattice distances and orientation of crystal structures but also provides a method to detect irregularities in the surface such as defects when operated in ultra-high vacuum and/or low temperature measurements. Modern AFM setups include most FFM functions and can be easily utilized to study friction forces while also gaining knowledge about the topography of the sample.

3.2 Basic Principles of Operation

To assess the physical qualities of a surface an AFM uses a probe positioned in close proximity to the sample of interest. This probe is made from a very sharp tip (tip radius usually around 5 nm), which is attached to a flexible cantilever beam of various lengths, depending on the mode of operation. These AFM sensor probes are usually made out of silicon and can be equipped with different material tips like diamond or cantilever coatings such as gold or aluminum for better reflection properties.

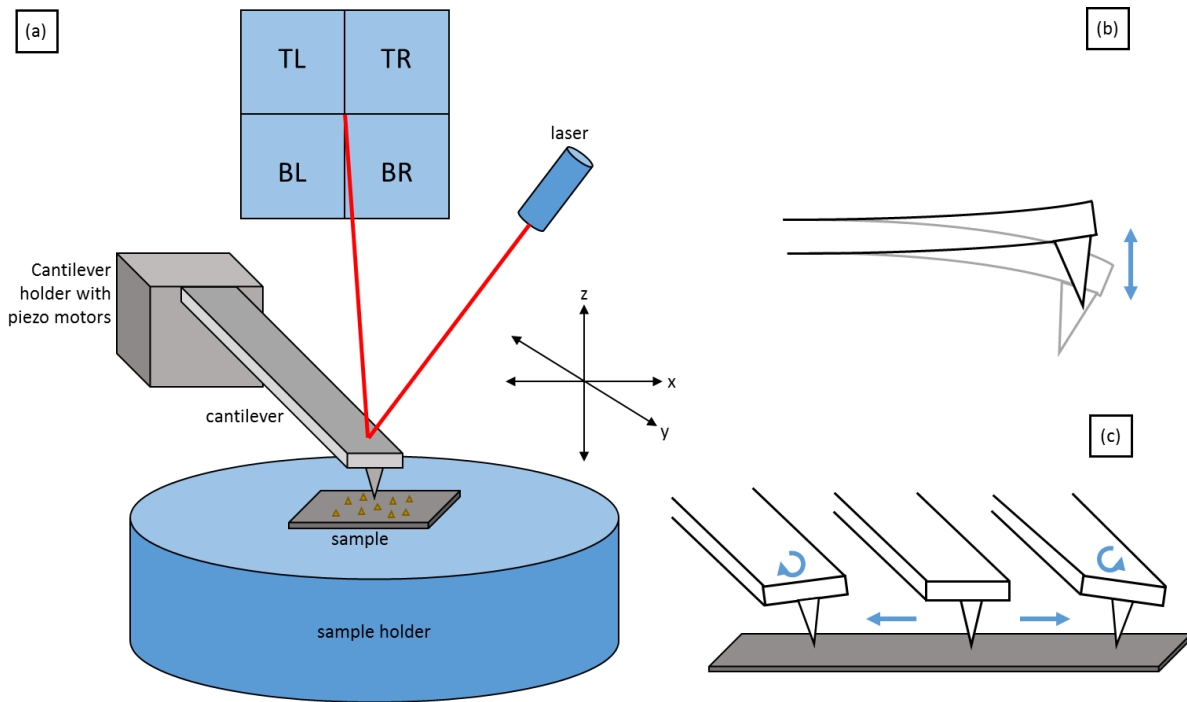


Figure 5 (a) Basic working principle of the AFM used in this work. The cantilever is fixed to piezo motors acting as actuators. A laser is reflected on the probe onto a position sensitive detector recording the deflection angles caused by bending and twisting of the cantilever (b) normal bending experienced by the cantilever in correlation to the normal force F_N . In tapping mode the bending is induced through excitement to oscillations. This vertical deflection is recorded by the PSD top (T) to bottom (B) (c) torsional bending of the cantilever proportional to the lateral force F_L recorded by the PSD as lateral deflection left (L) to right (R)

A laser beam is positioned atop of the cantilever, reflecting the beam onto a position sensitive photo detector with a four-quadrant photodiode. An optical camera is placed directly above the glass cantilever holder, which has a window to allow a top view of the cantilever beam, the laser point position and the sample surface. Using the inverse piezo-electric effect, motors can be used to move the sample or the tip in all three spatial dimensions with a precision as low as an angstrom ($1 \text{ \AA} = 10^{-10} \text{ m}$). When the tip is brought in contact with the surface a force is applied to the cantilever which leads to bending and twisting of the cantilever beam. This displacement can be recorded by the change of the two angles of reflection of the laser towards the position-sensitive detector. Other techniques exploit the piezo-electric effect using sensors to extract piezo-electric voltages when a force is applied to the tip or detect the normal cantilever deflection with the help of optical interferometry [46].

A four-quadrant photo sensor allows easy conversion of laser displacement and the correlating forces acting on the tip due to the linear relation. Therefore, the normal and torsional bending is calculated as

$$U_{T-B} = (U_{TL} + U_{TR}) - (U_{BL} + U_{BR})$$

$$U_{L-R} = (U_{TL} + U_{BL}) - (U_{TR} + U_{BR}),$$

with T-B defined as top/bottom and L-R as left/right. To reveal the actual force values calibration factors θ_z and θ_x have to be determined by using a calibration procedure for each sensor before the measurement, typically with a disengaged tip by repositioning the laser on the detector [47].

$$F_N = \theta_z * U_{T-B} - F_{N,ref}$$

$$F_L = \theta_x * U_{L-R} - F_{L,ref}$$

To keep the separation between tip and sample constant the AFM operates in a feedback loop. This is achieved by comparing the defined set point with the normal force signal and adjust the displacement of the tip in z-direction through the motors of the scan head. When the sample surface is scanned by the AFM the cantilever is moved perpendicular to the cantilever beam, the so-called fast axis or x-axis. Once the end of the to-be-scanned area is reached, the tip returns on the same path to close the loop (retrace) and moved in y-axis (slow axis) to the next line. To rule out undesirable effects of the tip approaching the surface for each line of the fast axis, an over-scan of typically 10% is applied in measurements in this work. The combination of each scanned line and the recorded change in z-coordinates with the recorded change in x- and y-coordinates allows for the reconstruction of a plane of constant normal force which is a good approximation of the surface of the sample.

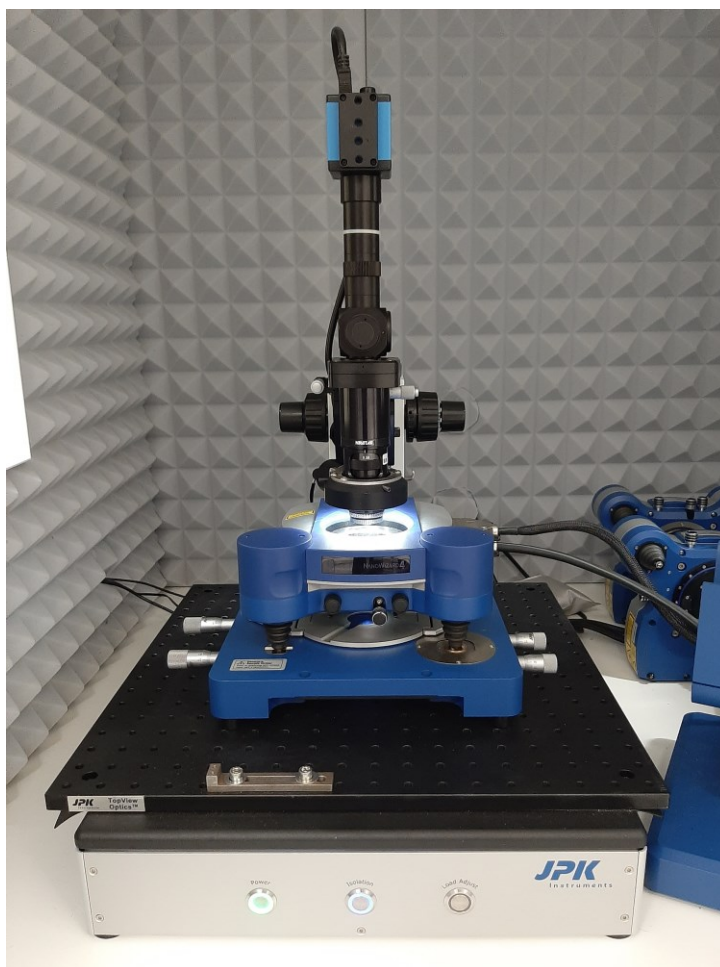


Figure 6: JPK NanoWizard 4 standing on its table-top vibration isolation system, all housed in an insulated soundproof chamber. The interchangeable scan head sits on top of the sample stage while an optical microscope observes the sample and the cantilever position through the scan head and the glass cantilever holder.

The AFM NanoWizard 4 used in this work differs in its operational principle from other commercial AFMs available. While the majority instruments keep the cantilever fixed and move the sample holder with piezo motors. This gives a high grade of stability to achieve even lattice resolution at room temperature in ambient condition. However, the Nanowizard 4 takes a different approach by keeping the sample stationary in its holder and the tip is being moved with help of piezo motors. Originally designed for characterization of soft matter like living or dead cells this change provides a lot of advantages in the field of nanomanipulation. It allows the user to modify the sample holder with different accessories like an ultrasound stage or a motor stage for moving the sample very precisely without changing the measurement conditions of the cantilever itself. This asset is used in this work extensively as discussed later in chapter 6.1. The so-called hover mode is an additional feature that can be utilized in contact mode nanomanipulation where the tip is retracted from surface contact to

an adjustable distance on retrace lines and therefore does not provide any forces to displace nanoparticles. The topography data from the previous trace line is used to keep the tip-sample distance constant.

Another advantage of this machine are the interchangeable scan heads provided by JPK. While the normal scan head provides a range of 100 x 100 μm in x and y with and a maximum height range of 15 μm for the cantilever movement the user can also choose a so-called ultra-speed scan head with a maximum line rate of 100 lines/sec or a so-called ultra-lateral scan head specifically built to be highly sensitive to changes in the lateral signal. Those special scan heads allow the user to perform accurate measurements in the regime of tens of nanometers by sacrificing some range of motion for the cantilever to 30 x 30 μm and a z range of 6.5 μm . Especially the ultra-lateral head was useful to this work, achieving lattice resolution on MoS_2 in an image size of 5 x 5 nm as can be seen in chapter 5.1.

3.3 Calibration Methods

To determine the forces experienced by the tip of the cantilever the signals recorded of the deformation of the cantilever (bending and twisting) must be converted by calibration with help of the bending stiffness k and the lateral force calibration factor, Since there is a correlation between the voltage signals of U_{T-B} and U_{L-R} from the position sensitive detector and the normal forces and lateral forces experienced by the tip, absolute quantitative measurements of actual normal force F_N and lateral force F_L are possible with the help of calibration constants θ_z and θ_x . Each constant can be viewed as product of stiffness k of the cantilever and detection sensitivity β :¹

$$\theta_z = k_z \cdot \beta_z$$

$$\theta_x = k_x \cdot \beta_x$$

While the constants k are determined for each sensor, the sensitivities β shall be measured every time after replacement of a sensor or optics readjustment. The geometry of the cantilever plays a big role in the stiffness and can be calculated as such:

$$k_x = \frac{Gwd^3}{3Lh_{tip}^2} = k_z \cdot 2 \left(\frac{L}{h_{tip}} \right)^2$$

Where G is the shear modulus and h_{tip} represents the tip height of the used cantilever [47]. Both formulations are based on the application of the so-called Euler-Bernoulli elastic beam theory and only apply for very small displacements, which are in general not exceeded in AFM measurements. For rectangular cantilever beams, as used in this work, the force constant k_z can be determined after a formula by Bhushan et al. [47]:

$$k_z = \frac{Ewd^3}{4L^3}$$

with the Young's modulus E , cantilever width w , length L and thickness d .

However, the Nanowizard4 AFM in this work uses a different calibration method to determine the forces. With the so-called *Sader method* [48] the geometric properties of the cantilever along with its resonance frequency are used to calculate the cantilever stiffness k following the formula

$$k = M_e * b * h * L * \rho_c \omega_{vac}^2,$$

where M_e is the effective mass of the cantilever, b , h and L are the width, thickness and length of the cantilever beam, along with ρ_c for the density of the cantilever material. Lastly, ω_{vac} is the angular resonance frequency of the cantilever in vacuum. Since all AFM experiments in this work were executed in ambient conditions, the cantilever beam experiences a damping effect caused by air molecules which has to be taken into account with a correction factor.

Table 1: Used cantilevers and their characteristics

AFM tip	Company	Material	Cantilever shape	Normal spring constant [N/m]	Free resonance frequency range [kHz]	Tip radius [nm]
ContAIG	Budget Sensors	Silicon with reflective Al coating	Rectangular	0.07 – 0.4	9 – 17	< 10
PPP-NCHAu	Nanosensors	Silicon with reflective Au coating	Rectangular	10 – 130	204 – 497	< 10
CT300	Team Nanotec	Silicon with reflective Al coating	Rectangular with conical tip	20 - 95	208 - 392	< 10
D300	SCDprobes	Silicon with single crystal diamond tip	Rectangular	20 – 75	265 – 400	< 10

3.4 Contact Mode Measurements

This form of normal load measurement utilizes the linear relation between the normal force F_N and the vertical deflection of the laser on the position sensitive detector to control the tip-sample distance and interface. For calibration of the relation between normal force and deflection on the detector a force-distance measurement is performed, where the tip is positioned away from the surface. Piezo motors incrementally reduce the distance while the z position and the vertical deflection is recorded. Once the tip enters the regime of long-range forces, attractive forces can be detected by the decreasing values of U_{T-B} . When the tip snaps into contact with the sample, short-range repulsive force linearly increase with the increase of the normal load to a previously defined amount. Eventually the cantilever gets retracted, reducing the tip-sample force. Once the adhesion force between tip and sample equals the restoring force, the tip snaps off and loses contact with the sample. This force can be used as a measure for the adhesive force interaction in the contact interface. Therefore, plotting the z position of the tip against the normal force F_N reveals a hysteresis in the force-distance curve.

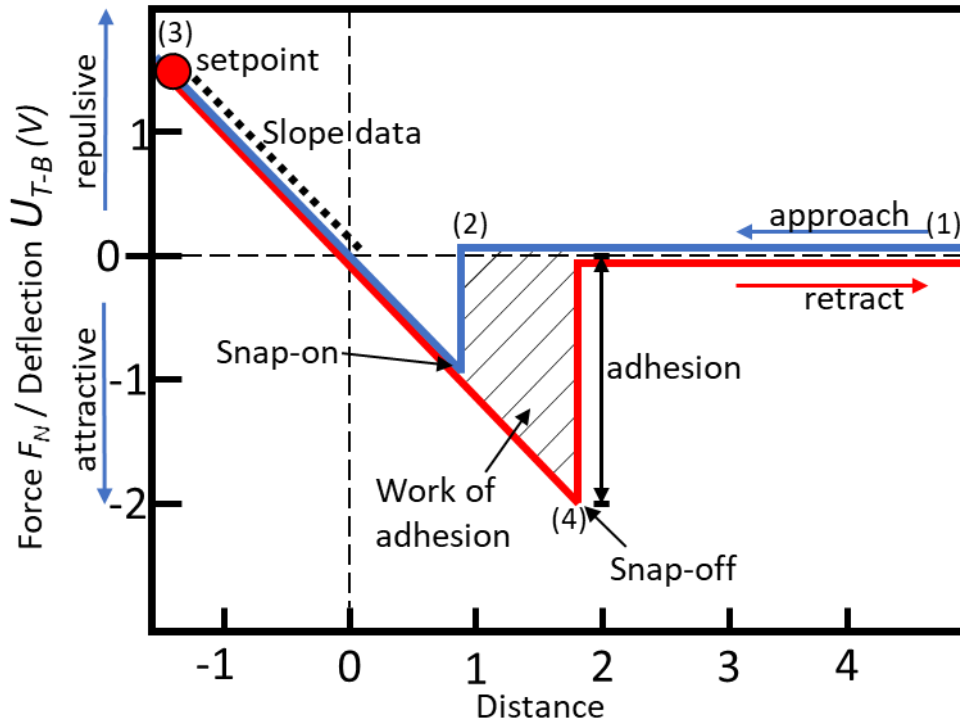


Figure 7: A sketch of a typical force-distance curve (hysteresis). In the beginning of the measurement the tip is separated from the surface with U_{T-B} of the PSD adjusted to zero (1). With the approach of the tip towards the surface the tip apex eventually come into the long-range force regime, attracting the tip which will lead to the snap-on (2). Further reduction of the distance leads to a linear increase in vertical deflection until the predetermined setpoint is reached (3). The slope of the deflection represents the stiffness of the sample and can be visualized using QI-mode. Afterwards the tip will move away from the surface until the pulling force exceeds the adhesion force at the snap-off point (4). The area created between snap-on and snap-off points is defined as the work of adhesion.

When scanning in contact mode the normal force set point is kept in positive values outside of the hysteresis area to avoid sudden tip jumps due to changes in V_L . On the other side even relatively small set point forces can lead to undesirable surface modifications, such as manipulation of nanoparticles or even destruction of surface features. Two methods can counteract snap-in instabilities to avoid aforementioned problems. Using a cantilever with a high spring constant eliminates one of the minima, therefore the tip cannot jump between those. Unfortunately, this technique lowers the sensitivity of the lateral force, since k is coupled to factors like cantilever length and material elasticity. For nanotribological investigations, this becomes an obstacle since a high lateral force resolution is essential for understanding tip-surface interactions. This can be avoided by using soft cantilevers with a low spring constant k in the range of 10 to 20 kHz using tapping mode, as described in chapter 4.2.

3.4.1 Normal Force Measurements

When measuring a surface with an AFM tip in constant contact a multitude of forces act upon the interface of tip and substrate, such as Pauli repulsion, van-der-Waals-, elastic-, friction-, electrostatic and/or magnetic forces [47]. Furthermore, the most influential forces to consider can be constrained to interactions with a Lennard-Jones-type potential V_{LJ} :

$$V_{LJ}(z_{tip}) = \epsilon \left[\left(\frac{z_0}{z_{tip}} \right)^{12} - 2 \left(\frac{z_0}{z_{tip}} \right)^6 \right].$$

In this equation the minimum value of V_{LJ} is signified by $-\epsilon$ when the tip position is a $z_{tip} = z_0$. Short-range forces like Pauli-repulsion are described in the first summand, while long-range van-der-Waals forces and dipole interactions are included in the second summand.

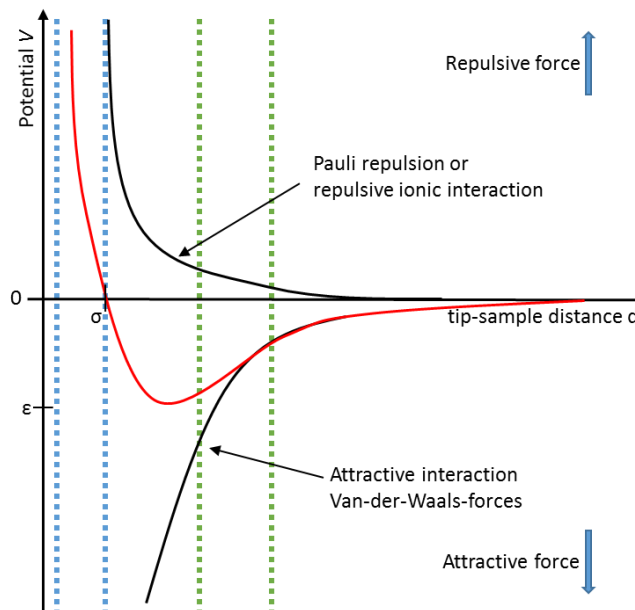


Figure 8: Lennard-Jones potential shows the interaction between long range van-der-Waals forces attracting the tip to the surface with $d > 2 \text{ \AA}$ and short range Pauli-repulsion repelling the tip due to overlapping electron orbitals with $d < 2 \text{ \AA}$. In contact mode the tip is experiencing interatomic repulsive forces highlighted by the blue dotted line, while in tapping mode the tip barely touches the surface while oscillating and therefore being exposed to attractive long-range van-der-Waals forces.

The interaction between the cantilever support at position z and the tip position z_{tip} is defined through a potential, taking the stiffness of the cantilever k_z according to Hooke's Law into account as a first approximation of the LJ potential around the minimum:

$$V_{Cant}(z_{tip}) = \frac{1}{2}k_z(z_{tip} - z)^2$$

When the AFM is operating the tip experiences a superposition of these two potentials. When imaging a surface, the tip-sample interaction is kept constant in normal direction while the tip traces the topography. With help of different control variables, the feedback loop can be used to achieve different ways of measuring the normal force. In this work three different operational modes were used, namely *contact mode*, *tapping mode* and *QI-mode*, which will be discussed below.

3.4.2 Lateral Force Measurements

Mate et al. [19] first modified the original concept of the AFM [43] making it possible to measure the lateral forces F_L parallel to the surface. The so-called Friction Force Microscope (FFM) is nowadays a common extension to commercial AFMs. The position sensitive detector with its four quadrants measures the lateral forces F_L through a quantity U_{L-R} proportional to the torsion experienced by the cantilever beam when dragged over a surface in a perpendicular angle to the driving motion. When inserting a cantilever into the cantilever holder it is generally not placed in a perfect 90° angle leading to a non-constant zero-force reference $F_{L,ref}$ when the tip is moved or a different normal force is applied. A friction loop addresses this issue by recording the lateral force of each scan line in both directions (trace & retrace). The value of $F_{L,ref}$ can therefore be determined as the mean of the signal vectors of both trace and retrace of the lateral signal. Since the lateral force sensitivity is the highest along the x-axis due to bending and twisting of the cantilever beam, these line signals can be used to calibrate and measure lateral force changes. For calibration the value of $F_{L,ref}$ can be determined by the mean of the signal vector measurements of both directions

$$F_{L,ref}/\theta_x = [U_{L-R,trace}, U_{L-R,retrace}].$$

The calibration factor θ_x is determined in a separate step which takes the cantilever stiffness k and the sensitivity β into account for both normal force and lateral force measurements. After the correction of the zero point by subtracting $F_{L,ref}$ the mean kinetic friction F_F can be calculated:

$$F_F = \langle |F_{L,trace}|, |F_{L,retrace}| \rangle$$

With the total dissipated energy E_{diss} equal to the area enclosed between trace and retrace

$$E_{diss} = \left| \int F_{L,trace}(x) - F_{L,retrace}(x) dx \right|.$$

3.5 Tapping Mode Measurements

This method of measurement utilizes a self-oscillating cantilever to operate in a frequency-modulated dynamic mode, also referred to as non-contact (NC) mode. A piezo shaker excites the cantilever beam at the current resonance frequency f by the measurement of the normal deflection sign U_{T-B} , consecutive amplification and adding a frequency shift of $\pi/2$ [49]. To keep the oscillation amplitude constant, the amplification gain is continuously adjusted by an automatic gain feedback control unit. With help of a phase-locked loop (PLL) detector the oscillation frequency f is measured. While retracted from the surface, f equals the free resonance frequency f_0 of the cantilever beam, since only the harmonic spring potential of V_{cant} is available. By gradually approaching the surface while the cantilever oscillates the tip will eventually experience a deformation of the total potential due to the normal surface potential. This leads to a characteristic resonance frequency shift Δf which is used as a variable for the feedback circuit to control the tip-sample distance [50]. This allows the tip to break the contact to the surface completely in each oscillation cycle, imaging of the surface topography with greatly decreased lateral forces. This is especially useful, if the surface features delicate structures, nanoparticles or even living cells. With the help of ultra-sharp tips, the cantilever can stay within the attractive force regime, thus allowing measurements without even getting in contact with the surface.

4 Concepts of Nanomanipulation

The experimental realization of frictional contacts in the nanoscale relies heavily on means of reproducibility and well-defined conditions. The method of choice for experiments has been the FFM [19] for its precision of force measurements down to the pico newton range and the ability to quantifiably measure friction of contacts of just a few atoms. On the other hand, contacts realized with an FFM tip are not as well-defined as desired, since there is no direct channel to observe the actual contact area and its change during the experiment. Schwarz et al [51] reports a large margin of error due to alignment issues and wear-induced changes in the contact area, even with *ex situ* SEM measurements of the tip in combination with models of elastic contact mechanics of an idealized tip geometry.

This problem becomes more prevalent if one is interested in the friction of extended nanocontacts with regard to the contact area. A flattening of the tip may be achieved through wear, but prone to errors, because of the difficulty to align a flattened tip with the substrate surface. One solution proposed by Schwarz [51] is the usage of large spherical tips, thus avoiding the necessary alignment of the interface. However, this method relies of idealized geometries for contact size estimation again. Also the nanoroughness of the surfaces measured creates another obstacle. To avoid multiple contact points in the interface Özoğul et al. [52] performed scans with a large spherical probe to create a single nano asperity to be in contact with the surface.

To overcome these obstacles, the manipulation of nanoparticles has proven itself to be a very potent technique in the field of frictions measurements [32], [53–56]. A nanoparticle is pushed or dragged over the substrate by an AFM tip, while the lateral force needed during the translation of the particle is recorded, yielding the friction force between substrate and said particle. Compared to traditional friction experiments using a direct contact of a FFM tip and the substrate or SFA, this offers a number of advantages. First, it eliminates uneven pressure distributions when curved surfaces are used, as it is the case with AFM tips with large tip radii or SFA experiments. Furthermore, nanoparticles grown onto the substrate using thermal evaporation or similar methods result in nanoscopically smooth extended contacts, thus eliminating the tilt effect of an AFM tip in contact with the surface. With an estimation of the contact area and knowledge about the contact geometry the shear strength (friction / area)

can be calculated. Additionally, many nanoparticles can be found and probed within a single scan frame. This allows manipulation of many particles with different contact areas, configurations and shapes in quick succession. Finally, the choice of materials in contact with each other is much greater with regard to nanoparticles. While AFM tips are constrained by the class of materials that allow mass production of tips and SFA experiments are limited to mica-on-mica interfaces, nanoparticles offer a wide variety of different materials in contact with each other.

Looking back at earlier research in the field of nanomanipulation, much can be learned for the experiments conducted in this work. To truly understand the behavior of friction and adhesion, scientists started to focus crystalline materials due to their predictable structures and the availability of growth processes in the nanoregime for particle deposition like PVD or CVD. Already in 1996 Sheehan et al. [54] found a strong friction anisotropy when sliding MoO_3 crystals on a single crystal MoS_2 surface and attributes this phenomenon to the commensurability of the interface. This work was built on the studies of friction anisotropy measured in muscovite mica by Motohisa et al. [57] where four preferential directions of low friction aligning with the crystal orientation have been found.

For better understanding of the forces influencing the movement of nanoparticles and the influence of tip – particle interaction Rao et al. [58] analyzed the outcome of a raster path-like moving pattern of the tip during scanning versus a zigzag path. While the zigzag motion scatters nanoparticles with an increasing angle of deflection from left to right in the manipulation image, a raster pattern leads to mostly parallel displacement pathways of particles. From this a model arises to describe the collision between tip and nano object in contact and tapping mode in relation to tip size and line spacing. However, the model assumes the particle as a sphere moving over an isotropic surface leaving out any directional locking effects of the interface.

Another comprehensive study by Mougín et al. [59] investigated the manipulation of coated gold spheres on silicon in tapping mode. They observed different displacement behavior depending on the angle of trajectory with abrupt jumps along the fast scan direction (x-axis) and smooth translation close to the slow scan direction (y-axis). The power dissipation during manipulation shows an initial higher value of stationary particles which lowers once the object is being moved by the tip. With increase of temperature in ambient conditions there is also a

significant decrease of power dissipation on the particles since temperature can be seen as an obstacle to forming stable water bridges and intermolecular bonds that leads to a reduction in adhesion.

A closer investigation into the translation – rotation relationship of nanoparticles was done by Nita et al. [60] on 300 to 600 nm large flat antimony particles on MoS₂. Results of the experiments and numerical simulations show low shear stresses for Sb particles of $\tau \sim 0.2$ MPa. The work also highlights the spinning motion of the irregular flower shaped nano objects during displacement in manipulation images which reveals itself in curve-shaped trajectories and the varying friction during this process which is a valuable indicator for further work with different nanoparticles. As already mention by Mougín et al. ambient conditions and room temperature play a role in the decrease of friction and adhesion for such experiments.

Discussing the role of epitaxial growth, commensurability and manipulation of particles Pimentel et al. [61] focused on grown calcite crystals on dolomite and kutnahorite surfaces in a liquid environment. They achieved the detachment of particles from their initial growth position by gradually increasing the normal load in contact mode until displacement while recording the lateral signal to estimate the shear strength required for movement. The results show a clear influence of commensurability between the grown crystal and the substrate. While the calcite / dolomite interface with a large mismatch of $\sim 4.78\%$ required a shear stress of $\tau \sim 7$ MPa, the more commensurate system of kutnahorite – dolomite with a mismatch of $\sim 3.17\%$ leads to a need shear stress of $\tau \sim 130$ MPa. This is an indication that the mismatch of crystalline interfaces of epitaxially grown interfaces is a controlling factor in the forces needed for manipulation.

Another interesting study into the formation and manipulation of gold nano objects with the goal to create conductive nanowires was done by Moreno-Moreno et al. [62]. While standard techniques for metal electrode deposition using polymer masks can connect objects with sizes below 30 nm, the whole process involves multiple steps from the deposition of the polymer mask, computer-controlled focused electron beam patterning to crack the polymer chains, removal of the marked region with organic solvents, deposition of metal and finally the removal of the polymer layer. However, this multi-step procedure comes with drawbacks such as the exposure of the sample to vacuum and chemical agents, polymer residue left over from the mask removal and finally the work- and time intensive process of reconfiguration or

upgrading existing nano circuits. To overcome these difficulties, the researchers in this study chose to deposit gold nanowires from a suspension in water by drop casting onto the substrate. With help of AFM manipulation in contact mode nanowires could be moved along predefined trajectories and even fuse wires together due to mechanical cold welding as a consequence of the high surface-area-to-volume ratio [63]. While this method avoids many difficulties like the exposure to vacuum and different organic chemicals and in addition provides a way to alter existing nano circuits after deposition, it inherently comes with its own drawbacks. The deposition of nanowires with this method leads to a rather unorganized pattern of nanowires in random orientation, which then have to be manipulated to connect the desired objects on the substrate and also to clear left-over wires away from the created connection. Due to the spontaneous cold welding mentioned above this can be a time-consuming process with the risk of assembling a “net” of remaining gold wires. The constructed conductive wire also appears in a dendritic shape which is undesirable for future applications in mass-scale production of nano electronics.

4.1 Manipulation in Contact Mode

The AFM can be utilized not only for imaging topography but also to manipulate the surface of a sample or nanoparticles on said surface. For this the tip of a cantilever is used to exert forces sufficient enough to induce modifications of the surface while at the same time measuring the acting forces.

After imaging the topography and locating nanoparticles in the scan area, the cantilever is brought into contact with the substrate in contact mode. When the tip on its previously chosen path comes into contact with a particle, opposing lateral forces act on tip and the nanoparticle. With the cantilever continuing the path the forces increase in a linear fashion to the point the nanoparticle starts to move. This happens when the lateral force eventually overcomes the static friction experienced between the particle and the substrate. The particle now will travel in unison with the tip for a short amount of time. By increasing the set point F_N^{SP} the maximum of exorable lateral force also rises, since through the sloped contact of tip and particle normal and lateral force are bound together.

With this technique, nanoparticles are prone to move to either side of the tip when manipulated. The reason for that is the fact that the tip most likely will not engage the particle at the exact center of mass which can lead to a loss of contact, as shown by Dietzel et al. [64]. In the reality of an experiment the adhesion between a nanoparticle and the tip counteract this problem and can even be used to drag a particle behind the tip if the static friction is low enough. One downside of this method is the time intensive sequence of imaging-manipulation-imaging for a single particle. This can be circumvented by scanning a single frame of the whole area with the chosen set point for manipulation. Multiple particles will be manipulated in the same image which can be used for statistical analysis of movement patterns and particle behavior in case of the collision of two or more manipulated particles. On the other side a tip used for manipulation might experiences a decent amount of wear during the process, depending on used forces and materials.

4.2 Manipulation in Tapping Mode

This technique offers multiple advantages to the typical contact mode manipulation mentioned above. After imaging the area in tapping mode with a high relative set point and therefore a high drive amplitude, the same cantilever can be used for the manipulation step. By decreasing the amplitude to a very small value the tip still oscillates but with a smaller distance to the surface leading to a strong tip-sample interaction. Once the vibrating tip reaches a nanoparticle it transfers energy to the particle without staying in constant contact which leads to the excitement of said particle its displacement. Through regulation of the set point and its gradual reduction the threshold for manipulation can be found [65]. This depends on the static friction between the nanocluster and the substrate, the contact area of the interface and other properties like superlubricity.

While tapping mode manipulation cannot reveal the lateral forces need to move a particle directly it brings certain advantages with it. However, if the contact area of the displaced particle can be estimated the power dissipation during the manipulation process can be calculated [59]. Beside the aforementioned reduce of tip wear and increase of sequencing speed, a big asset is the interrupted contact between tip and nanocluster during the manipulation. While in contact mode the tip acts as a plow moving nanoparticles to the side,

in tapping mode manipulation energy still gets transferred to the cluster without dragging it along or blocking the movement in the direction of the oncoming tip. Contrary to the typical contact mode “kicks” of nanoparticles along the scan line, displaced nano objects tend to move perpendicular to the fast axis.

4.3 Manipulation in Quantitative Imaging-Mode (QI)

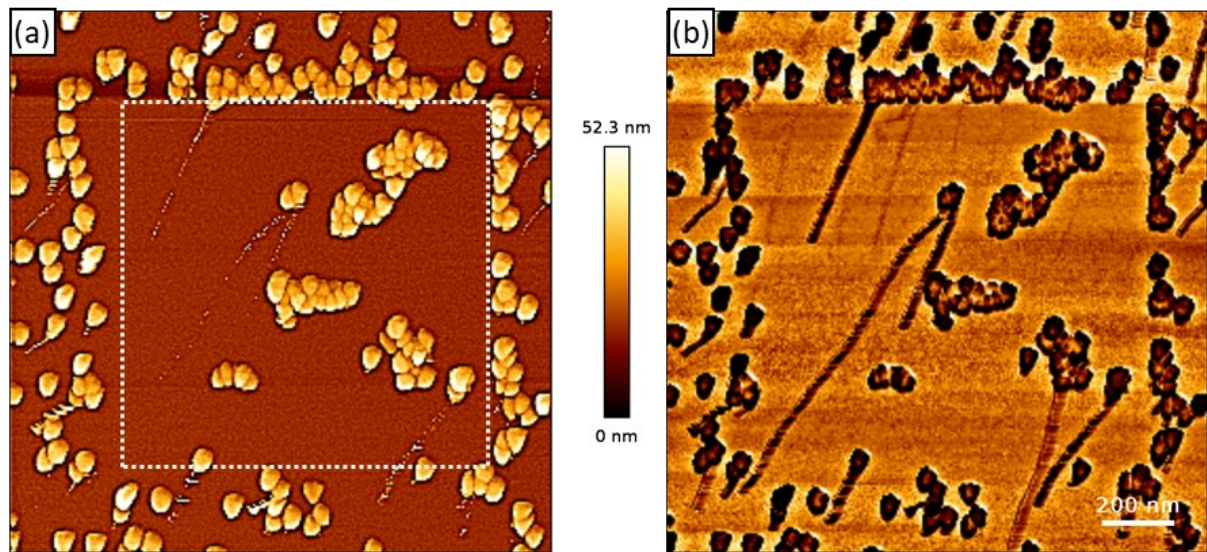


Figure 9: QI mode manipulation image of Au islands into an already cleaned area (dotted square). (b) corresponding adhesion map of the manipulation reveals the trajectories of displaced particles with a high contrast between the low adhesion gold islands and the MoS₂ substrate

This mode of operation takes a series of force-distance curves in a measurement grid of 256x256 locations on the surface, where later in the image each point represents a pixel in the height, adhesion and stiffness map [66]. The tip approaches each point to measure its height while simultaneously measuring the stiffness of the sample from the slope of the force-distance curve during the approach to the surface and also the adhesion force from the snap-off of the tip when retracting from the surface. This not only allows to map adhesive regimes and the stiffness of surface and particles, but also gives a force-distance measurement for every pixel of the created image. Although this system is less stable than contact or tapping mode and can easily degrade the tip quality due to the higher forces used, it provides great contrast in the generated adhesion images to visualize particle movements.

5 Materials

5.1 Molybdenum Disulfide (MoS_2)

Molybdenum disulfide belongs to the Transition Metal Dichalcogenides (TMD) which consist of a layered crystal structure, where within one monolayer the atoms are covalently bonded. These layers are just connected by a weak van der Waals interaction [67], [68]. A single layer of MoS_2 is formed by layer of molybdenum atoms sandwiched between two layers of sulfur atoms. It has become quite an attraction to researchers for its potential applications in catalysis, valleytronic applications, optoelectronics and nano electronics. Its abilities as semiconductor change with the number of layers. Whereas a monolayer has a direct band gap of ~ 1.8 to 1.9eV , bulk MoS_2 shows an indirect band gap with 1.2eV [69], [70]. This makes monolayer MoS_2 a competitor with graphene, which has a zero-band gap. While the material counts as very promising for applications in electronics and optoelectronics, it is hard to connect to metal electrodes due to a high interface resistance. This is an indication for a high Schottky barrier at the interface [71]. This could be caused by strong interface bonding which creates states of the interface that pin the Fermi level or by weak bonding creating a potential step due to Pauli repulsion at the interface [72], [73].

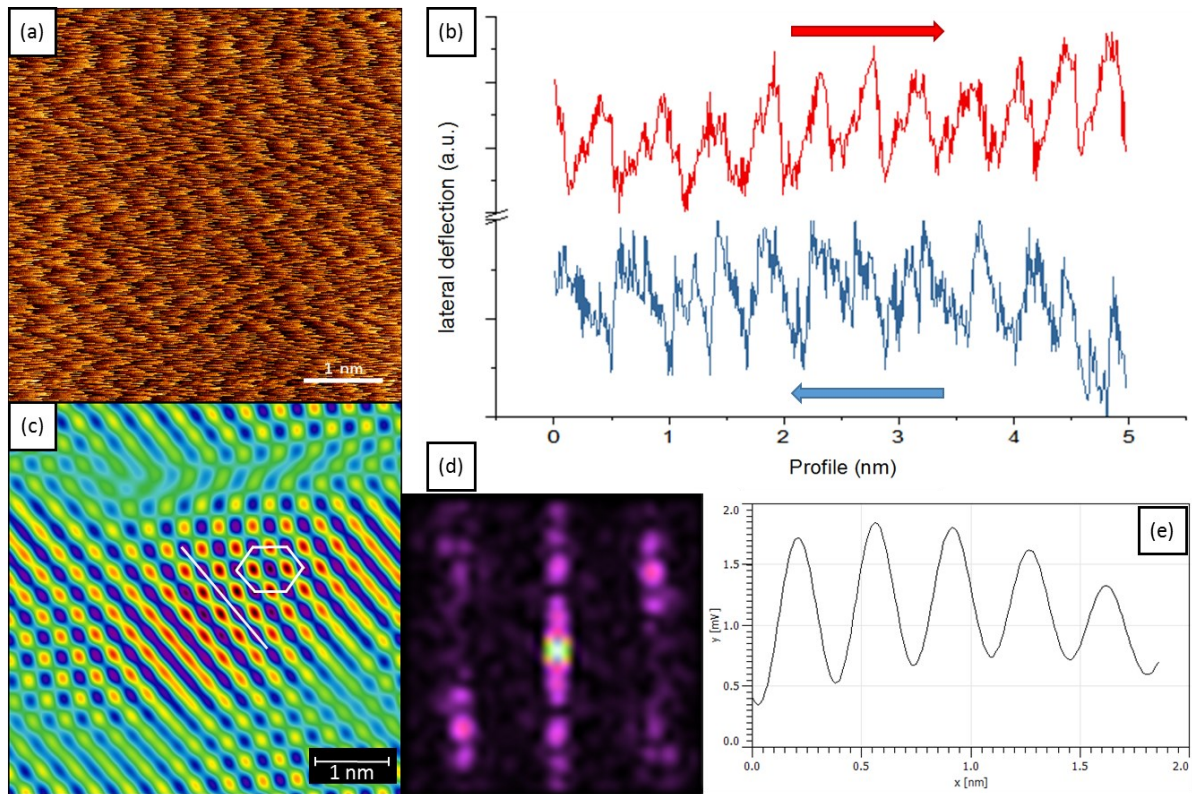


Figure 10: (a) lateral deflection image with a size of 5x5 nm of contact mode measurements using ContAIG with visible thermal drift (b) trace (red) and retrace (blue) profile of the lateral signal on the same scan line show the typical hacksaw tooth pattern for stick-slip events. (c) 2D autocorrelation map highlighting atomic position of the MoS₂ surface with its highlighted hexagonal crystal structure. (d) Fast-Fourier-Transformation (FFT) transforming X-Y representation of the signal into polar representation highlighting the periodicity and angle of the lateral signal data (e) Profile of the 2D autocorrelation map (white line) showing a periodic interatomic spacing of $\sim 3.5 \text{ \AA}$

In the Industry MoS₂ is widely used as a solid lubricant due to its atomically thin layers that can easily slide against each other. Applications can be as an additive in greases and oil, as a component in composite coatings or as dry lubricant by itself. But unlike graphite, which has a similar lamellar structure and lubrication properties, MoS₂ does not require a humid environment and it has been shown that its lubrication efficiency drastically improves in oxygen-deficient conditions [74]. This ultra-low friction between layers of crystal was explored with different methods over the years. In the early 1990s Martin et al. [75], [76] studied the behavior with help of TEM, providing images of the sliding process exhibiting low wear and friction. Another study investigating the friction of MoS₂ coatings by Fleischhauer et al. [77] does not only show a friction coefficient in the ultra-low regime (in order of 0.001) but also the significant variability depending on the rotational structural mismatch of the two basal planes in contact with each other. To observe the sliding process between layers in situ,

Oviedo et al. [78] performed experiments utilizing cross section TEM to record the displacement of a layer of MoS₂ from a few-layer stack with help of a tungsten tip which quantifies the shear strength between two commensurate layers to be 24.8 ± 0.5 MPa. The sliding of a single layer over its bulk parent substrate in the incommensurate regime was observed by Wang et al. [79] using a silicon nanowire inside a SEM as a mechanical force sensor. The measurements obtained support the original proposition by Martin et al., show an ultra-low friction coefficient of 0.0001. Molecular dynamics simulations of sliding between two individual MoS₂ sheets have also shown the super-lubricity phenomenon in relation to the rotation of the crystals and therefore commensurability, with a 100-fold decrease in friction force when transitioning from the commensurate to the incommensurate state [80] with the highest energy barriers to sliding located on top of the S atoms of the crystal structure. In addition, Coulombic repulsion between the layers provides the reduction of energy barriers induced by the structural mismatch.

The study of friction on 2D materials, including MoS₂, paints a different picture. While the easy shear between basal planes in their bulk form has been responsible for the lubricity, monolayers of MoS₂ have still been recorded to have very low friction compared to typical substrates like SiO₂ the materials has been deposited on. This can be attributed to the atomic-scale smoothness, chemical inertness and mechanical strength of the 2D crystal [81]. However, it has been shown that a single layer of the material exhibits more friction than bulk material. According to Lee et al. [82] friction on mechanically exfoliated MoS₂ decreases monotonically with increasing number of layers until a total number of ~ 5 is reached, lowering friction to 40% of the friction of a monolayer. This effect can be explained with a mechanical process called puckering where the tip apex of the probe deforms the surface locally around itself (puckers), increasing the contact area and therefore the friction experienced. With growing number of layers, the bending stiffness in the vertical direction also increases which then counteracts the deformation enacted by the tip. In contrast, CVD grown polycrystalline samples of single-layer and few-layer material display an oscillating layer-dependence of friction, whereby even numbers of layers demonstrate lower friction relative to samples with an odd number. The authors of the study contribute this effect to the existence of permanent dipoles in samples with odd layer numbers which leads to an enhanced adsorption of charged species in interaction with the tip apex [83].

5.1.1 Growth of Monolayer and Bilayer MoS₂

For the growth of the synthetic molybdenum-disulfide crystals, silicon substrates with a thermally grown silicon oxide layer of 300 nm were used as a base. These wafer pieces by Sil'tronix are exceptionally smooth with a root mean square (RMS) roughness of <0.2 nm. Before the growth process the substrates were cleaned in an acetone ultrasound bath for 5 minutes followed by flushing in isopropanol and blow drying with argon gas. Once prepared a two-zone split tube furnace with a tube diameter of 55 mm (Carbolite Gero) was utilized to grow the MoS₂ crystals onto the Si wafers which allows for individual heating of the precursor materials. The outer tube was loaded with a smaller inner quartz tube of 15 mm diameter containing the growth substrates and precursors. A quartz Knudsen cell filled with sulfur powder (99.98%, Sigma Aldrich) was placed in the inner tube and positioned in the center of the first zone of the tube furnace. A piece of wafer was placed in the inner quartz tube and positioned in the second zone of the furnace. Sprinkled on top of the Si/SiO₂ wafer were approximately 1 to 5 μg of MoO₃ powder (99.97%, Sigma Aldrich). All growth substrates were placed next to the inner tube on the downstream side. After the evacuation of the quartz tube to a pressure of 5x10⁻² mbar it was refilled with argon (5.0, Linde). The growth process was carried out at atmospheric pressure with an argon flow rate of 100 cm³/min, which allows to carry the sulfur atoms down to the high temperature reaction area containing the MoO₃ precursor and substrates. This second zone is heated to the growth temperature of 770 °C at a rate of 40 °C/min and then held at the target temperature for 20 minutes. The first zone containing sulfur was heated separately to reach 200 °C once the second zone approaches a temperature of 750 °C. At this point a hydrogen (5.0, Linde) flow of 10 cm³/min is introduced to the furnace for the entire 20 min of growth time. After the growth process is completed the samples were allowed to cool down to 350°C in an argon atmosphere with a flow rate of 100 cm³/min. Finally, the body of the split furnace was opened to rapidly cool down to room temperature.

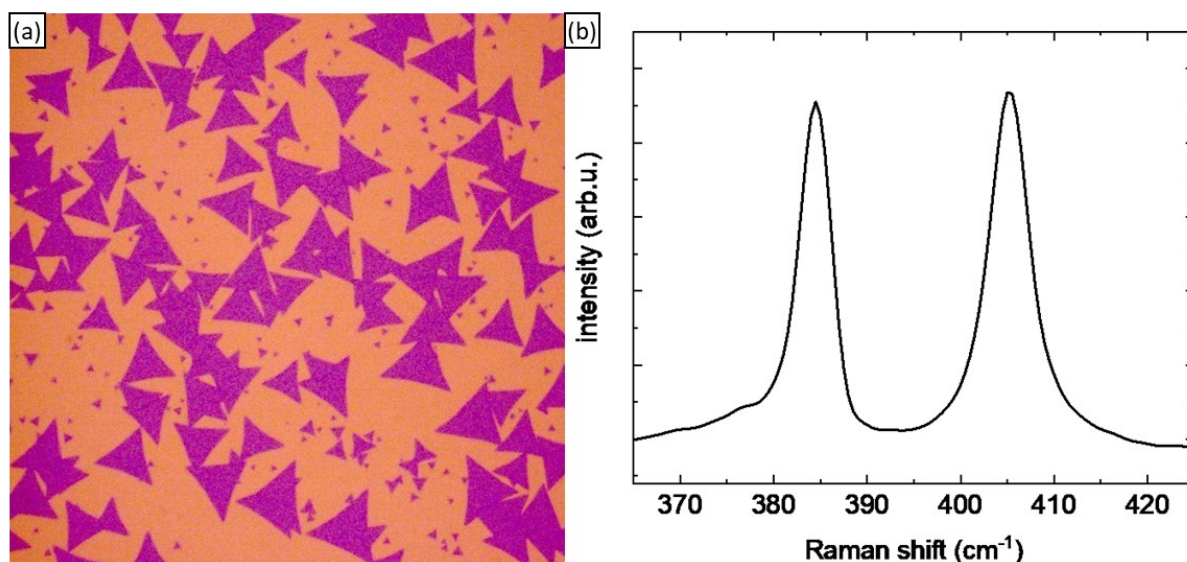


Figure 11: (a) optical microscope image of grown MoS₂ on SiO₂/Si substrates showing a high density of randomly oriented and sometimes intergrown triangular monolayers. (b) Raman spectrum measured on a crystal of MoS₂. The difference of peak positions is 21 cm⁻¹ corresponding to a monolayer

The few layer MoS₂ crystals were sampled using Raman Spectroscopy (Bruker Senterra Spectrometer) in backscattering mode. With help of a frequency-doubled Nd:YAG Laser, a 50x objective and a thermoelectrically cooled CCD detector measurements were obtained at 532 nm with a spectral resolution of 2-3 cm⁻¹. The Si peak at 520.07 cm⁻¹ was used for peak shift calibration of the instrument. To analyze the characteristic MoS₂ peaks the background was subtracted and the data fitted with Lorentzian functions to determine peak positions, FWHM and maximum intensity of the peaks. The Raman spectrum shows peaks characteristic for monolayer MoS₂, which are E₁2g at (384.4 ± 0.5) cm⁻¹ (FWHM = 3.6 ± 0.2) and A₁g at (405.3 ± 0.5) cm⁻¹ (FWHM = 4.6 ± 0.3). These originate from the in-plane vibrations of the Mo-S bonds on the E₁2g band and out-of-plane vibrations of S-atoms on the A₁g band. With a difference of 21 cm⁻¹ between the peaks the monolayer properties of the substrate can be confirmed.

The image above (Figure 11 (a)) was obtained using a Zeiss Axio Imager Z1.m microscope equipped with a 5 megapixel CCD camera (AxioCam ICc5) in bright field mode. It shows the growth of mostly monolayer MoS₂ crystals with random orientation on the SiO₂/Si substrate with a mean size of 10 to 20 μm although super large triangles with a size of up to 70 μm have been observed. Many crystals are joined together in random angles not aligned with the crystallographic axes of both triangles with no apparent boundaries at the connection point. With help of the more height sensitive AFM MoS₂ triangles show a second layer grown in the center of the crystal with a height difference of approximately 1.5 nm which corresponds to

the lattice distance of 1.489 Å in c direction of the unit cell [84]. This second layer influences the growth of gold islands on the crystal, which will be discussed in the chapter 5.1.1.

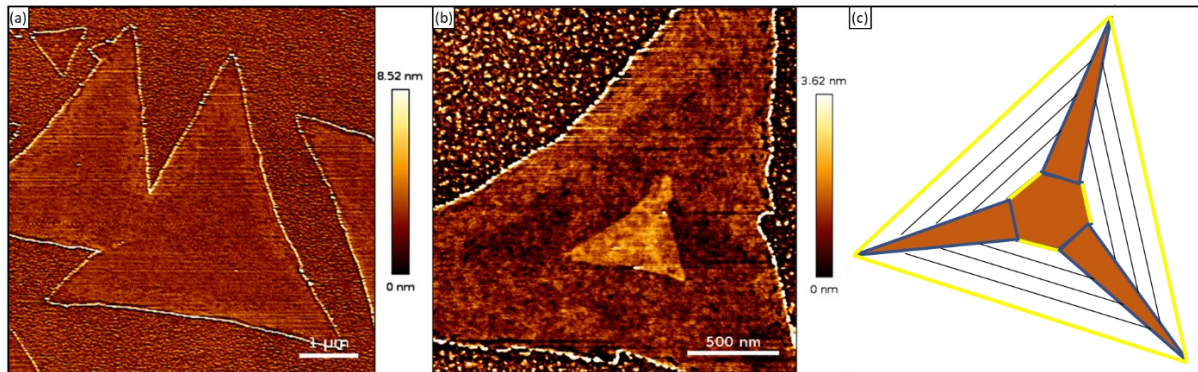


Figure 12: (a) height image of different monolayer MoS₂ crystals in random orientations, partially grown together. The concave borders signal a Mo : S ratio of slightly above 1 : 2 (b) example of a MoS₂ triangle with developed second layer grown from the center (height image) (c) schematic growth model showing the preferential growth directions (faces) developing the monolayer from a hexagonal structure to a triangle. After Wang et al. [85]

The shape of the MoS₂ crystals observed tends to show irregular triangles with concave sides and edge structures in a zigzag fashion. According to the basic principles of crystal growth [86] the shape of a crystal is determined by the growth rate of the different crystal faces. While the fastest growing faces disappear or become smaller, slower growing faces tend to grow the largest. The rate of growth is usually dependent on the surface free energy and in the case of 2D materials this corresponds to the edge free energy. Therefore, low-energy faces of a crystal tend to be also the slowly growing faces. For the case of monolayer MoS₂ the final shape is determined by the different growth rate of edge terminations. Two cases arise for the observed zigzag edges (as seen in Figure 12(b)) depending on the element forming the edge for the crystal. If a sulfur atom is exposed at the edge, forming a s-zz edge, the S atom has only two bonds with two Mo atoms, while saturated S atoms within the crystal structure form three bonds with three different Mo atoms. If a molybdenum atom is exposed, the bonds formed with Sulfur atoms drops from six bonds with six different S atoms in the case of a saturated Mo atom to only four bonds. This structural difference leads to different levels of chemical activity which eventually influences the growth rate and domain shape of the crystal [85]. Depending on the ratio of Mo and S during the growing process, different shapes of monolayer MoS₂ can

be the outcome. The samples discussed in this work show mostly truncated triangles which would correspond to a growth environment with a Mo : S ratio of slightly above 1:2.

5.2 Gold Nanoparticle Growth on Bulk MoS₂

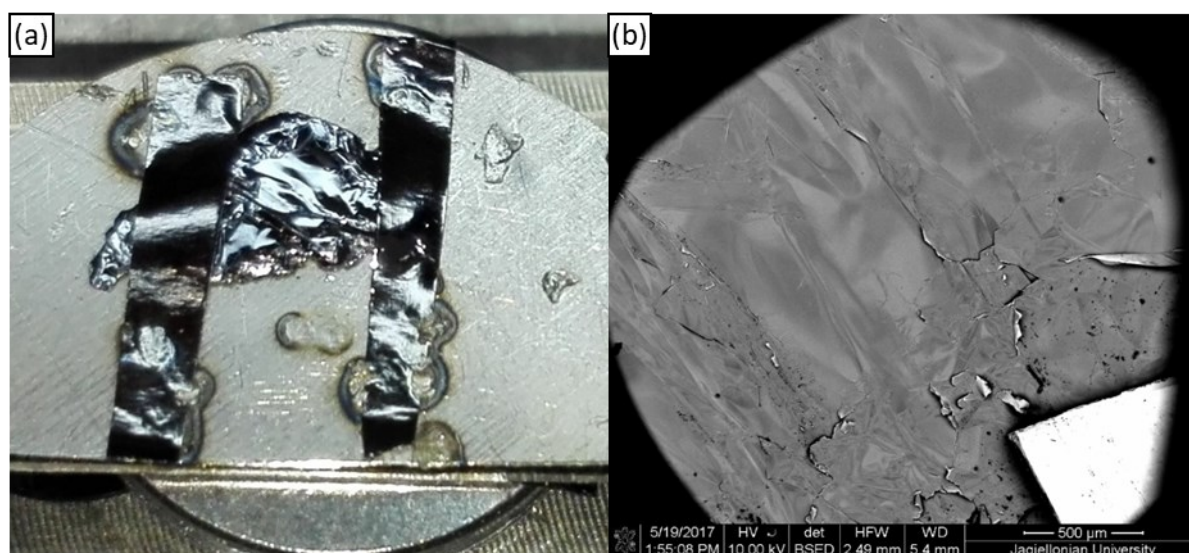


Figure 13: (a) MoS₂ sample mounted on the Molybdenum plate for gold deposition. (b) SEM backscattered electron image showing a wavy surface due to detachment of some layers from the bulk material caused by the sample preparation.

For the gold deposition the single crystal MoS₂ sample was mounted on a molybdenum plate. Using a Scotch tape, the first layers of the mineral were peeled off to obtain a fresh clean surface. Afterwards the sample was introduced into the lock-load chamber of the UHV system consisting of three interconnected chambers for sample preparation, STM imaging and surface analysis. The base pressure during the preparation was 10⁻¹⁰ mbar. With help of a pyrometer (LumaSense, IGA 100, with emissivity $\epsilon = 0.5$) the target temperature for the deposition was maintained in the chamber. After a 2 h period of outgassing at a temperature of 623 K, gold was introduced to the surface at a rate of 0.1 monolayers per minute (ML/min) until the required amount of monolayers was reached for the specific sample. After depositing the gold, the sample is subsequently kept at the deposition temperature for another 30 min to allow for migration of gold atoms to form nano crystals. After this process the MoS₂ crystal cools down to room temperature and is removed from the UHV chamber.

Table 2: Gold deposition conditions and properties of grown Au islands

	bulk MoS ₂	bulk MoS ₂	Monolayer MoS ₂
Amount of Au [monolayers, ML]	2	2	1.5
Deposition temperature [°C]	250	350	550
Au particle size [nm]	22.6 ± 0.5	13.79 ± 0.6	19.8 ± 0.3
Particle density [1/μm]	176 ± 14	310 ± 28	73.2 ± 1.2

While gold in crystalline form grows in a face-centered cubic structure, the nanostructures formed on top of the both natural and monolayer MoS₂ appear in a triangular shape with a size of around 15 to 25 nm with a thickness of 2 to 6 nm, depending on the growth conditions. This is explained by the unique physical and chemical properties of metal nanoparticles, where unlike to their bulk counterparts the chemical and crystallographic parameters of the substrate grown upon plays a major role in the growth of the nanoparticle. SEM and AFM measurements show clearly the crystalline nature of the gold particles often with truncated corners approaching a hexagonal geometry as reported by Dietzel et al [87]. The particles are able to connect with the MoS₂ substrate by (111) plane with a lattice distance of $a = 2,88 \text{ \AA}$. Note that due to the relatively large tip size of <10 nm and the inherent tip convolution the corners of gold islands in AFM measurements appear to be rounded.

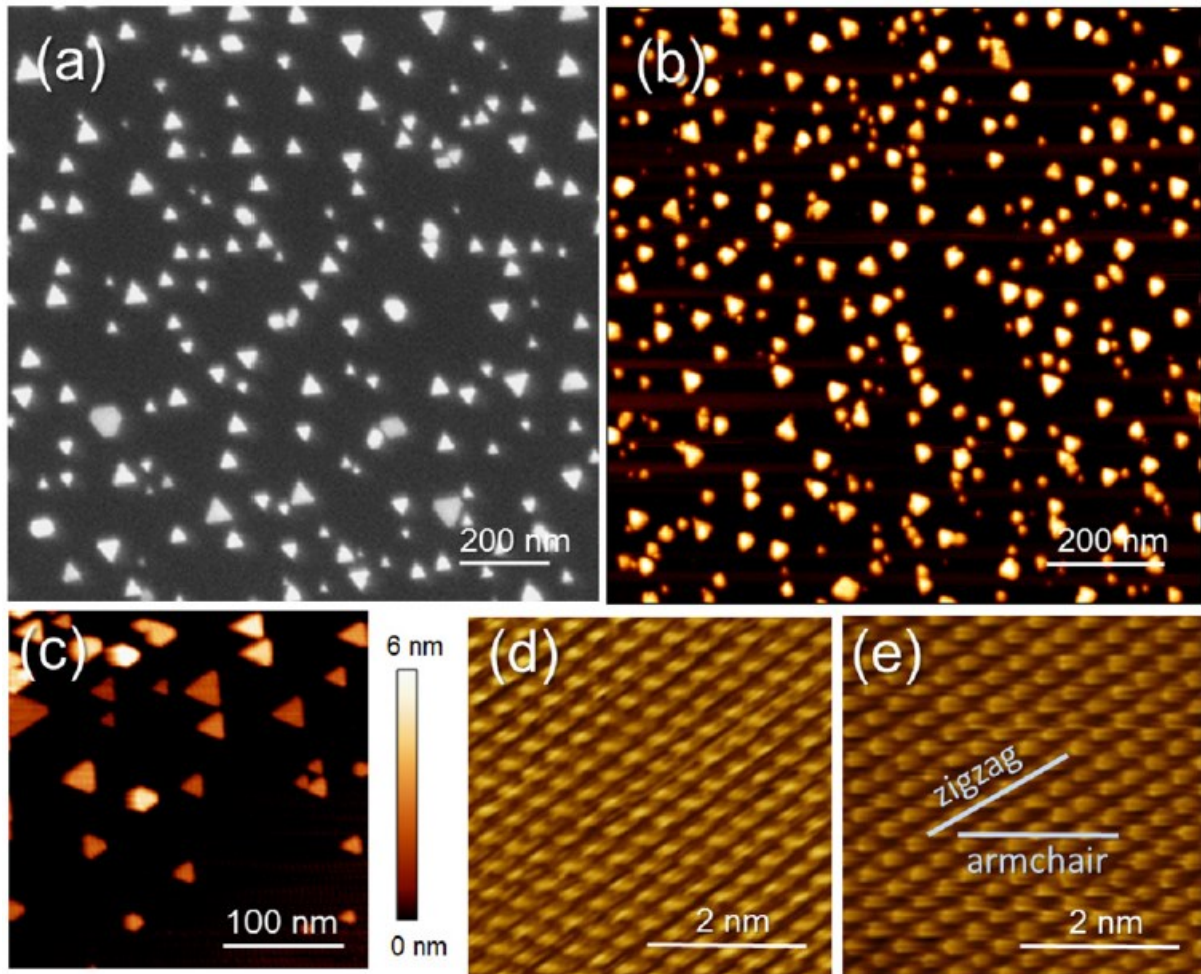


Figure 14: (a) SEM, (b) AFM tapping mode, and (c) STM images of different areas of the Au/MoS₂ sample in regions chosen for manipulation experiments. Scan parameters for STM: $V_{bias} = 1$ V and current $I = 100$ pA. (d), (e) Atomic resolution of an Au island and the MoS₂ substrate ($v_{bias} = 2.5$ V, $I = 400$ pA).

The images obtained with STM confirm the crystallinity of both gold and MoS₂ as seen in Figure 14 (d) and (e). The simultaneous imaging of both island and substrate with comparable resolution was not possible since the tip starts moving the gold nanoparticle when climbing up the side of island at $I = 150$ pA. It is also noteworthy that the STM tip detects only half of the hexagonal vertices since the placement of molybdenum atoms in the crystal lattice on different planes (heights) makes it quite difficult to reveal the true hexagonal structure. The microscope images of Figure 14 (a) and (b) also reveal an epitaxial growth pattern of the gold particles on MoS₂ which leads to a distribution of approximately 70 to 80% of the triangles facing upwards in the same crystallographic orientation.

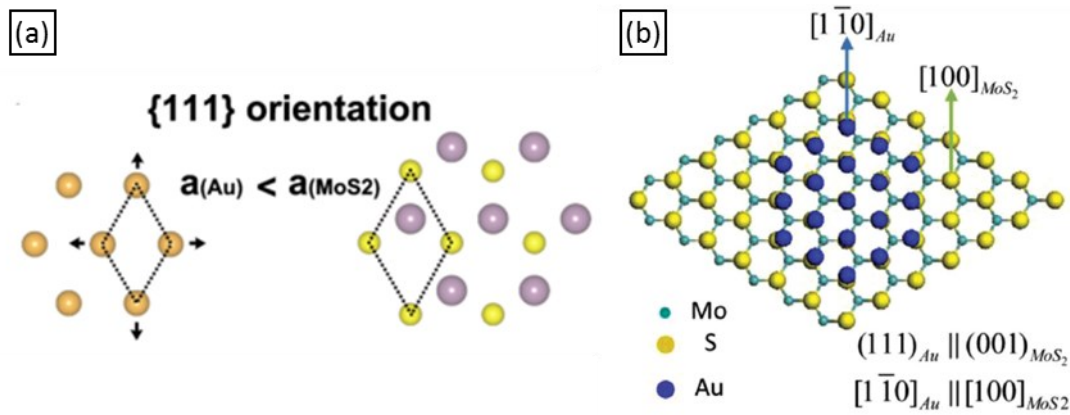


Figure 15: (a) The strain of Au atoms and MoS₂ in {111} respectively where Au is represented by orange circles, Mo by purple and S by yellow circles. After Zhou et al. [88] (b) Schematic model of atomic mismatch of the epitaxial growth of gold on MoS₂. After Junpeng et al. [89]

In the simplest models of epitaxy, the substrate is assumed to be infinite and can subsequently not relax in the growth process. This leads to a biaxial stress experienced by the gold atoms of approximately 8%. Even though a configuration of {001} with a misfit of -6 to 8% or a configuration of rotated {111} with -6% strain seem more favorable, {111} orientation growth is predominantly observed in experiments.

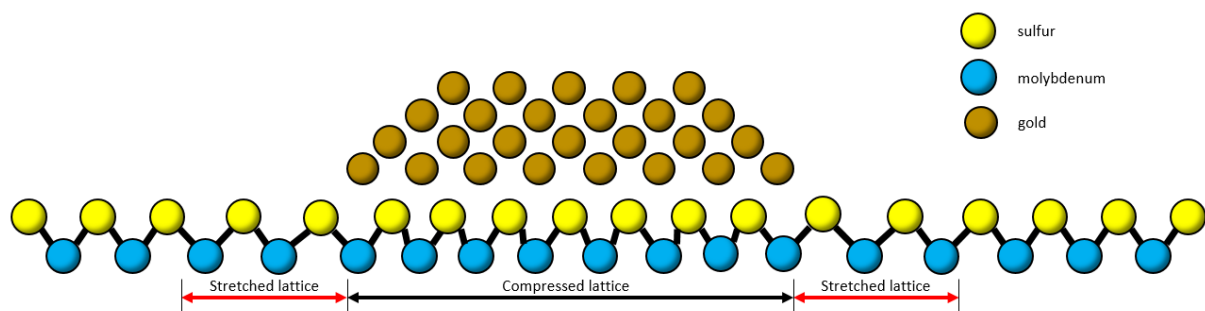


Figure 16: Au - MoS₂ system showing compression of the substrate lattice underneath the grown Au crystal, while the immediate area around the island experiences stretching in its lattice

The much larger elastic energy observed in this configuration comes down to the weak van der Waals bonding between MoS₂ layers which allow the surface layer of the substrate to relax nearly independently of the layers underneath. This leads to a lower formation energy in the Au growth process, considering surface and interface energies and misfit dislocations. It should be also noted that a compliant substrate leads to a reduction of dislocation density compared to traditional epitaxial growth since the substrate partially relieves any mismatch strain. This means that the MoS₂ substrate underneath the Au island will be strained in compression which is naturally accommodated by a tensile strain surrounding the island [88].

5.3 Gold Nanoparticle Growth on Monolayer and Bilayer MoS₂

Crystalline two dimensional materials have established themselves as a promising substrate for electronic applications due to their inherent order and symmetry, 2D properties like the Quantum-Hall-Effect and other peculiar phenomenons. Monolayer MoS₂ is no different with its hexagonal structure, low friction coefficient and semiconductor abilities. In addition, an indirect-to-direct band gap transition and strong photoluminescence occurs when thinned out to a single layer, making it an ideal candidate for applications in the field of nano-optoelectronics [90].

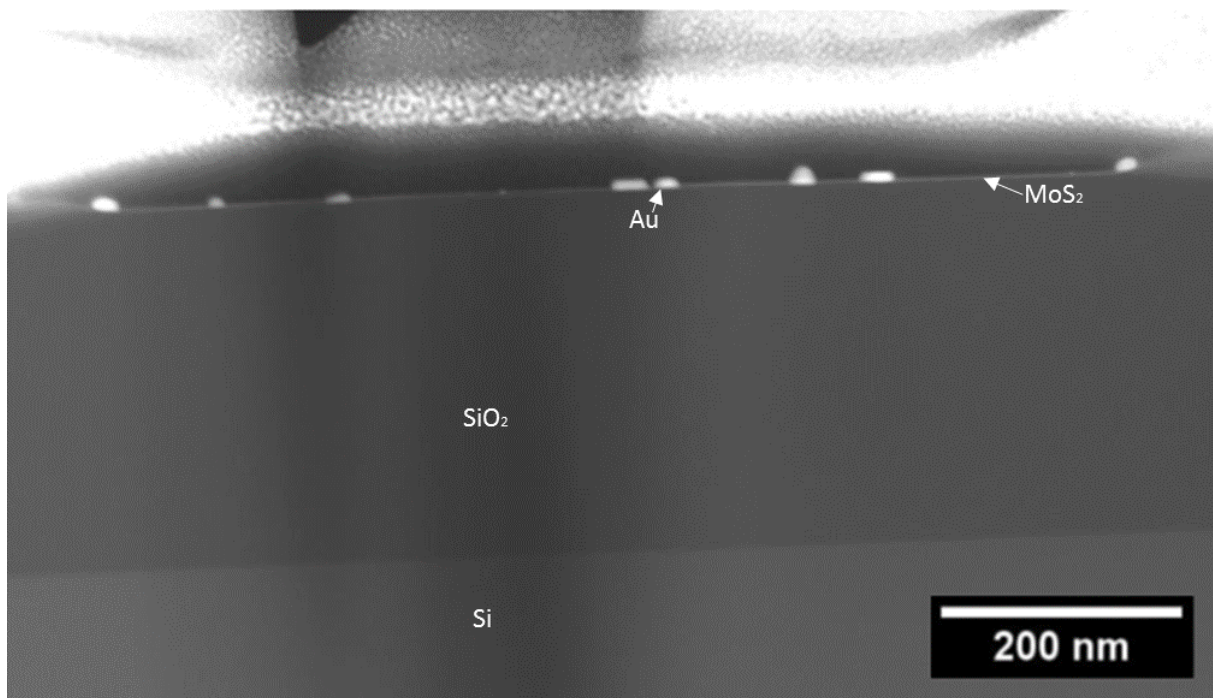


Figure 17: Dark field cross section achieved with HAADF-STEM of the monolayer MoS₂ system with CVD grown Au islands on top of a Si/SiO₂ wafer with a 300 nm thick SiO₂ layer.

The TEM cross section above created with Focused Ion Beam (FIB) shows the structure of the materials used for the nanomanipulation experiments. The monolayer MoS₂ sits on top of the 300 nm SiO₂ layer of the Si wafer. The grown gold particles have been crosscut by the FIB for later imaging to confirm their crystallinity and epitaxy with the substrate. Above the monolayer system the carbon coating needed for the TEM sample preparation can be seen with its grain-like structure.

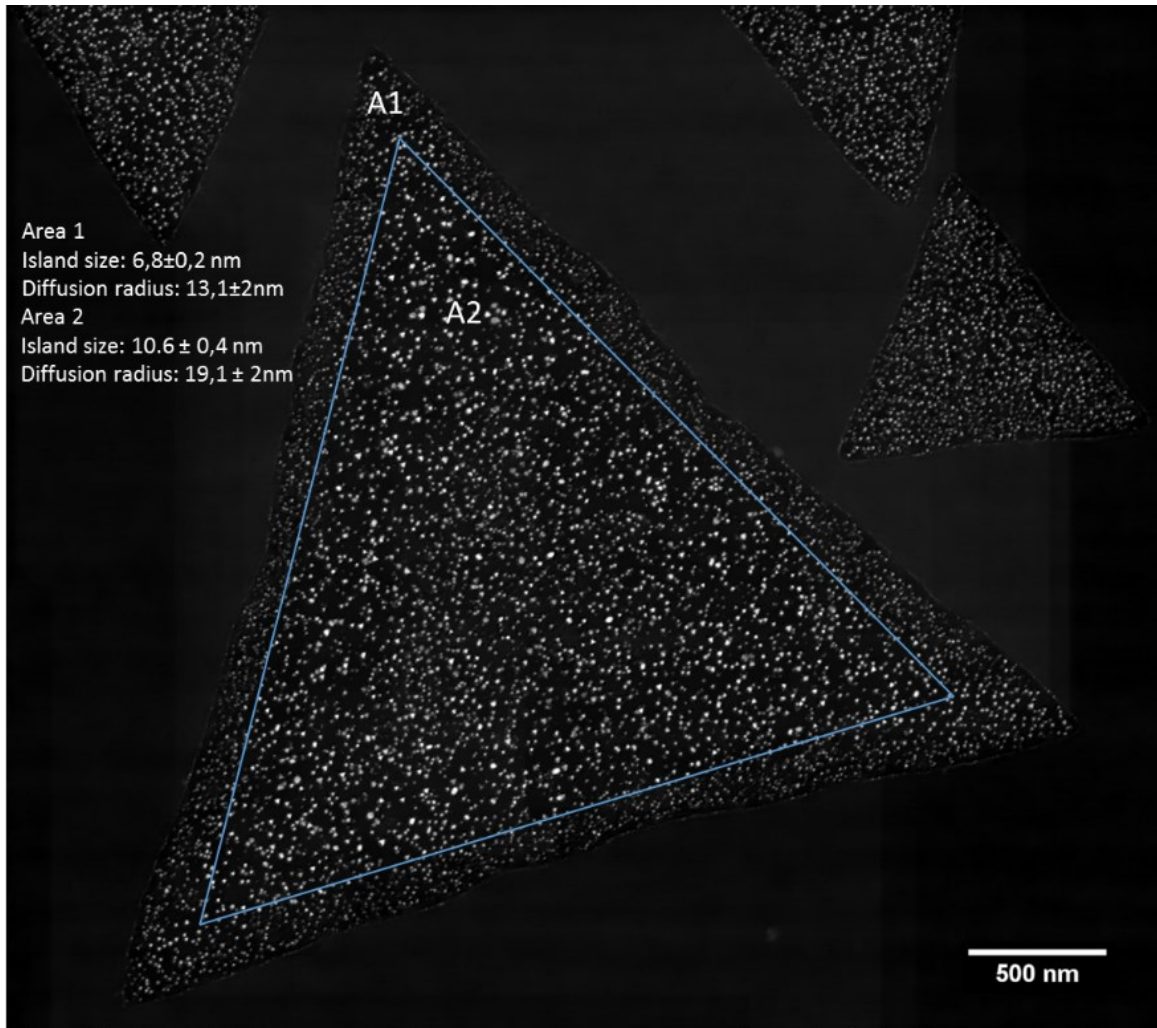


Figure 18: SEM image of monolayer MoS₂ triangles after Au deposition (1.5 ML) at 723 K. The center triangle exhibits different size and density of grown Au islands with smaller islands of around 6.8 nm in the border regions while Au nanoparticles in the middle tend to be larger with ~10.6 nm in average size.

The grown gold clusters are generally spread homogenously on monolayered islands with a broad size distribution of 10 to 20 nm and a diffusion radius approximately twice their size. However, especially larger islands with a size of 3 to 20 μm are divided into two areas with different Au island sizes and diffusion radii. While the border area (referred as A1 in Figure 18) with a width of 200 to 500 nm, depending on the size of the MoS₂ crystal, is decorated with Au islands smaller than 10 nm and a higher density distribution, the inner area of the island (referred as A2) displays bigger islands of 10 to 20 nm in size with a lower island density. This phenomenon is an indicator of the mobility of gold on the crystalline surface of MoS₂. Although crystals with a size of under 3 μm do not develop a border of smaller Au islands the effect can still be visible in the corners of the triangular flake, as can be seen in Figure 19 (a) below.

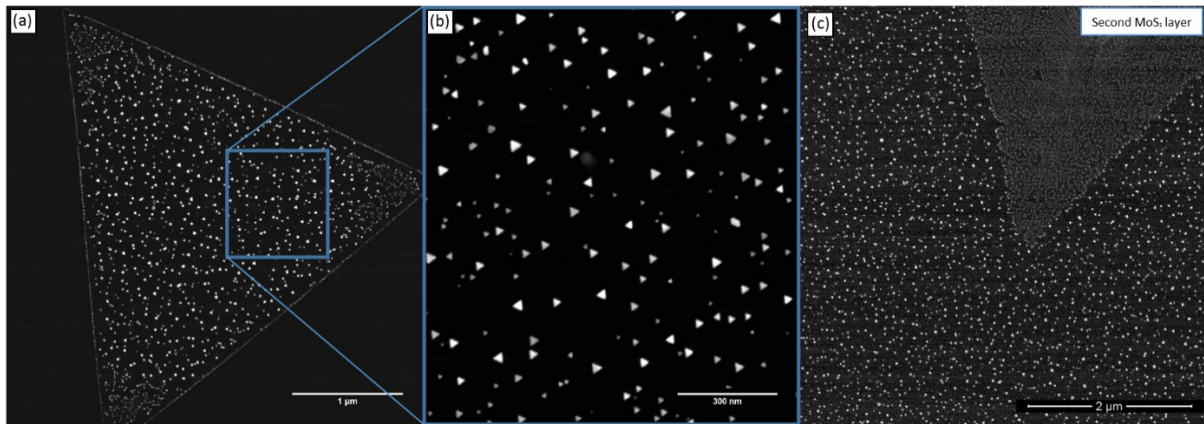


Figure 19: (a) SEM image of a smaller MoS₂ triangle with a size of $\sim 5 \mu\text{m}$ and CVD grown Au islands on top. (b) close-up of gold nanoparticles showing well-ordered orientation due to the epitaxial growth. (c) SEM image of another MoS₂ crystal with a second layer in its center after Au deposition (1.5 ML) at a temperature of 823 K. Au islands decorate the crystal edge to the second layer and exhibit a higher particle density and smaller particle size as a result of lower gold mobility during the annealing process in UHV.

As with bulk MoS₂, the grown gold nanoparticles on the substrate show clear signs of epitaxial growth which materializes itself in the ordered orientation of the triangles. With the MoS₂ triangles apex pointing downwards, the distribution of particle direction is heavily leaning to an upward orientation with about 80 to 85% of all accounted Au islands depending on the MoS₂ flake analyzed. Since the substrate triangles are distributed in a random orientation on the SiO₂ and every MoS₂ triangle shows a similar orientation distribution of Au nanoparticles, it can be ruled out that the angle of the beam used for the gold growth has an influence on the gold island orientation. Figure 19 (c) shows the gold growth on a second layer of MoS₂ which developed from the middle of the triangle. Due to the higher degrees of freedom along the edge of the layer gold nanoparticles are more prone to grow there, developing a decorated edge easy to see with AFM and SEM. Au islands grown on top of the layer show a much larger density distribution while the crystals themselves have a size of below 10 nm. This effect is a well-known result of the CVD growth process, as stated by Wang et al. [85]. This leads to the assumption that the mobility of Au atoms during the annealing process is much lower on the bilayer compared to the monolayer on the same MoS₂ crystal. Nevertheless, these gold nanoparticles appear to grow in an epitaxial fashion with hexagonal to triangular shapes as well.

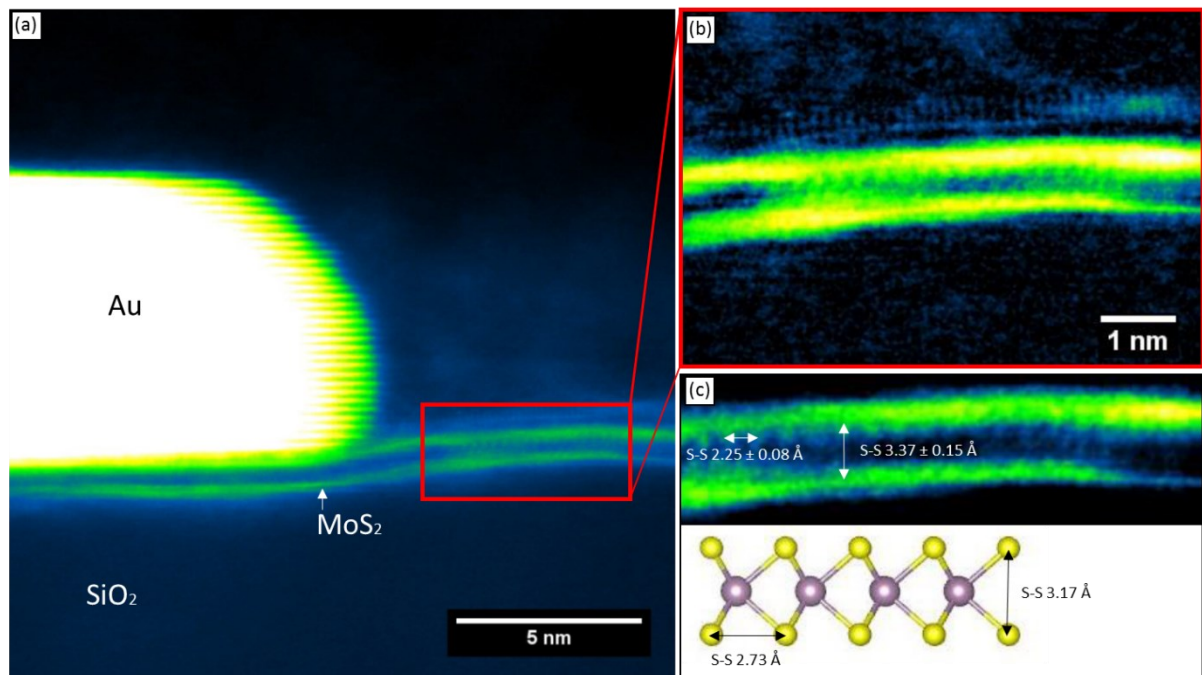


Figure 20: (a) Cross section HAADF-STEM image of a single Au island with visible crystalline atomic structure sitting on top of a monolayer of MoS₂ grown on a Si/SiO₂ wafer. (b) Close-up of the monolayer consisting of two bands of Sulfur atoms (green) with Molybdenum in between. (c) In-plane distance between S atoms shows a distance of $\sim 2.25 \text{ \AA}$ and $\sim 3.37 \text{ \AA}$ between the Sulfur bands. The discrepancy between measured and modeled interatomic distances is a result of the different crystallographic orientation.

With help of the High-Angle Annular Dark-Field Scanning Transmission Electron Microscope (HAADF-STEM) the crystallinity of the monolayer MoS₂ and also the gold islands are clearly visible. The close up image of Figure 20 (c) shows measurements of the distance between sulfur atoms in the Y- and Z-direction in comparison to the modelled distances of a monolayer of the substrate. While the gap between the atoms in z-direction is close to the model, the S atoms parallel to the monolayer show a much smaller distance. The reason for discrepancy is the crystallographic orientation of the MoS₂ which was not cut exactly along the Y-axis but in an undetermined angle due to the limitations of the Focused Ion Beam technique used for the sample preparation.

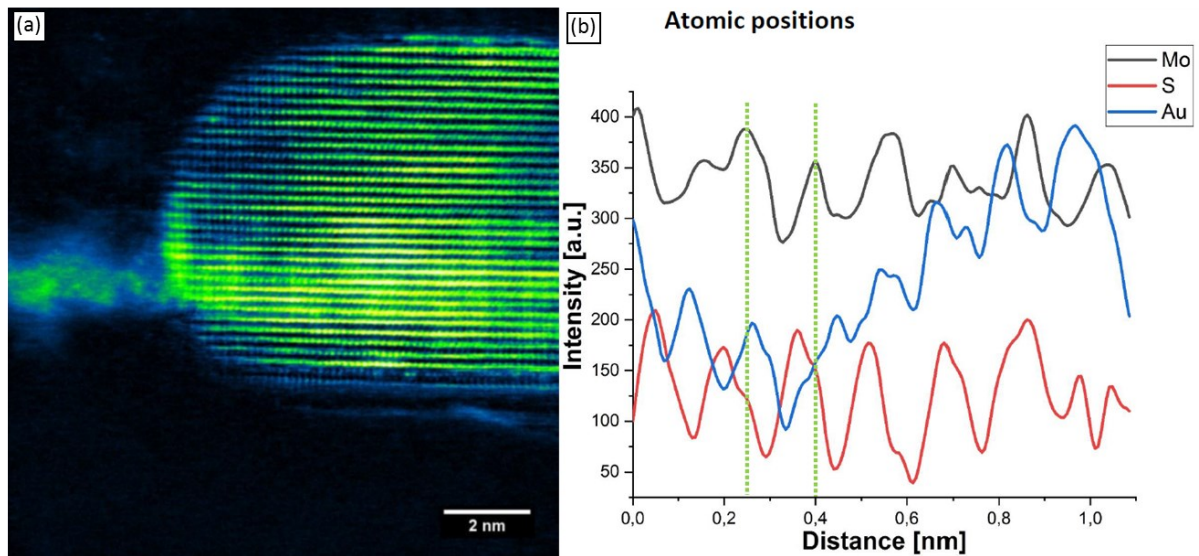


Figure 21: (a) High resolution HAADF-STEM image showing Au atoms well-structured in the crystal lattice of a gold island with 32 layers of atoms, sitting on top of a monolayer of MoS₂. Note the apparent roughness of the Si/SiO₂ wafer creating a not atomically smooth surface. (b) Intensity profile of the electron probe showing the atomic positions of Au, S and Mo.

TEM microscope images and measurements of atomic positions confirm the crystallinity of grown Au nanoparticles on the substrate, showing a well-ordered structure of gold atoms. It is noteworthy that the used smooth Si wafer with a RMS roughness of around 886 pm appears quite rough compared to atomically smooth systems on the nanoscale cross section. This possibly influences the growth of the Au islands whereas all nanoparticles imaged with cross section TEM sit in depressions of the with MoS₂ coated Si wafer.

6 Gold Nanoparticle Manipulation

First step of a nanomanipulation experiment is the characterization of the sample topography without disturbing and manipulating the surface covered with nanoparticles. This can be achieved with a tapping mode scan, which comes with the difficulty of finding the exact area again after changing the cantilever to a contact mode tip. Another technique requires a scan in contact with the sample, but at the minimal stable normal force set point. In this case the static friction of the particles is higher than the force acting upon it through the lateral tip movement [55]. Therefore, the nanoparticles stay in their initial location. Interfaces experiencing superlubricity between the surface and the particle might exhibit very low static friction, which makes the minimal stable normal force set point unreachable. This can be

averted by using tapping mode for the imaging of the initial topography and position of the nanoparticles, but this work around requires a cantilever change back to a contact mode tip which comes with the problem of the repositioning of the new tip onto the same exact area. On the other side the manipulation sequence can be done using the tapping mode cantilever, sacrificing the ability to read out the force needed to move a particle since the stiffness of said tip is too high for accurate measurements and imaging when used in contact mode.

6.1 Nanomanipulation of Au islands on bulk MoS₂

After establishing the basic properties of Au islands grown on bulk MoS₂, a systematic comparison of manipulation behavior of the particles between different scan directions was carried out. To allow the most freedom of movement manipulation sequences were carried out in tapping mode in ambient conditions. While in contact mode the tip is in constant contact with the surface and restricting the possible directions of particle movement by simply being in the way, tapping mode only transfers kinetic energy to the Au island for a very short amount of time. This gives the particle enough energy to move freely. It is also possible to image the position of the islands beforehand with a lower set point of around 1 nN in the present case, before switching to manipulation by simply increasing the normal load to 1.5 nN or higher. The vertical deflection channel (see Figure 22 (b)) provides an excellent tool to analyze manipulation trails of manipulated nanoparticles. 2D autocorrelation was used to determine the prevailing angle of displacement θ and later put in correlation to the angle of attack α . With this mathematical technique changes in the measured signals can be studied to analyze systematic variations. While topography images usually provide enough data for the autocorrelation, the vertical deflection shows sharper features at the manipulation pathways which makes it easier to separate actual displacement trails from stationary and already manipulated particles.

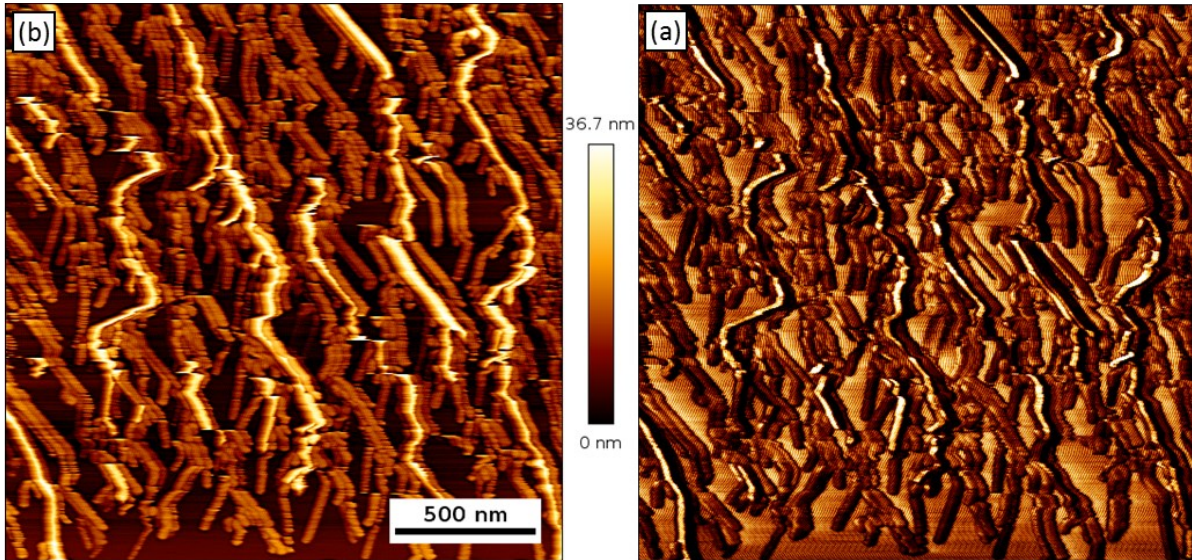


Figure 22: (a) Tapping mode topography image of a manipulation sequence at 60° sample rotation (b) vertical deflection image of the same sequence shows manipulation trails clearly for later statistical trajectory analysis.

With the initial positions of the nanoparticles mapped using a very low set point of around 1 nN, the exact movement and destination of the Au islands can be mapped during and after the manipulation process.

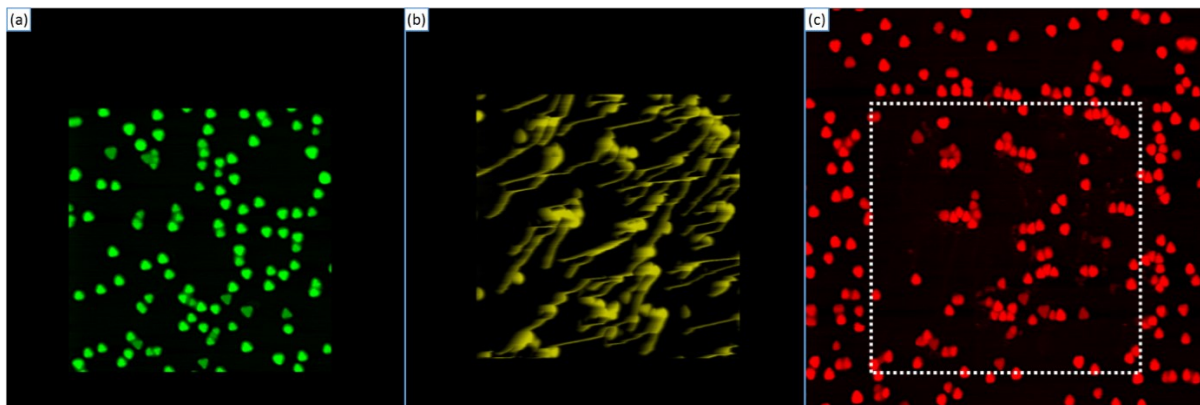


Figure 23: Nanomanipulation sequence in tapping mode with (a) 2x2 μm image to record the initial positions of Au islands (b) Tapping mode manipulation image with a rel. set point of 8% and hover mode (c) Overview of the manipulated area recording displacement positions.

Figure 23 provides all three stages of the manipulation. It is apparent that displaced particles predominantly stick to their starting orientation, even when pushed into other particles. This leads to the conclusion that Au islands do not rotate during manipulation but rather translate over the substrate in an epitaxial fashion with MD simulations confirming this thesis, as discussed in chapter 6.2.

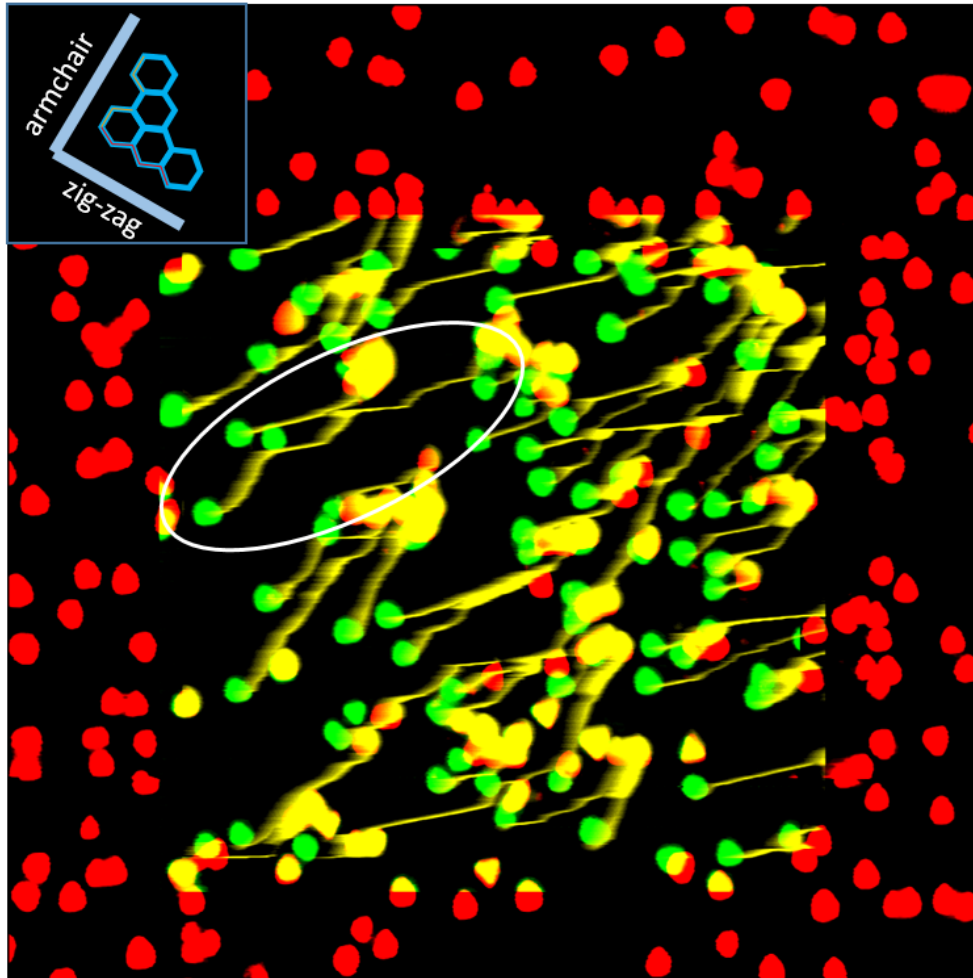


Figure 24: Combination of the sequence from Fig. 23. Green highlighted particles show the initial position of the Au islands, yellow pathways show the manipulation directions and red particles mark the resulting displacement. Note the particle in the highlighted area (white) manipulated along the armchair direction until the collision with another Au island, changing to zigzag direction multiple times to move around the obstacle.

When compiled into one image the pattern of displacement does not only show the prevailing direction along two directions differing by about 60° matching the crystallographic directions of the substrate, but also display what happens in case of particle collision. While some Au islands get stuck next to others, forming an immovable pile, others avoid a pile-up by changing their displacement angle to the armchair direction to get around the obstacle. After passing, the nanoparticle is able to change back to the original angle with the preferred lower friction force associated with it. Piled up islands predominantly stay in within their original epitaxial orientation from the growth process. Close up SEM images, as discussed in chapter 6.3, can provide more information about the agglomeration of Au islands as the result of the nanomanipulation.

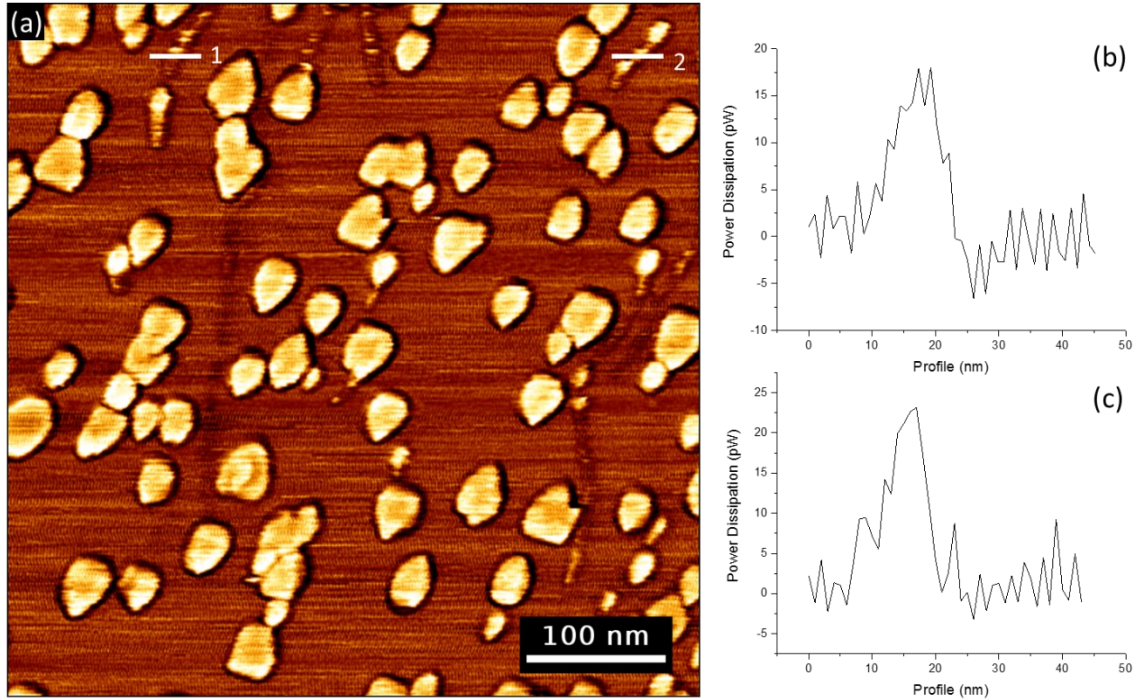


Figure 25: (a) Lock-in Phase image during manipulation 500 x 500 nm (b) Normalized power dissipation of the profile 1 (see (a)) showing power dissipated to the particle with respect to the substrate (c) Normalized power dissipation of profile 2 (see (a)).

The image above shows a phase image of a manipulation experiment in tapping mode. During the manipulation the oscillation amplitude of the tip A_{set} was kept constant in a closed feedback loop. Therefore, the power dissipation associated with the tip-sample interaction can be calculated using following formula [91]:

$$P_{dis} = \frac{kf_0}{4\pi} \left(A_{piezo} A_{set} \sin\phi - \frac{A_{set}^2}{Q} \right)$$

With A_{piezo} as the oscillation amplitude of the piezo element exciting the cantilever, the resonance frequency f_0 , the quality factor Q of the free cantilever and ϕ as the phase shift caused by tip-sample interaction. Analyzing the phase shift during the manipulation of a nano island leads to an estimated power dissipation of around 15 to 25 pW, depending on the particle when the background signal is adjusted to zero. This regime is consistent with previous measurements reported by Ritter et al. in manipulation experiments of flat antimony islands [32] and tapping mode experiments of 25 nm gold particles on Si wafers by Mougin et al. [59]. As can be seen in the image above (Figure 25) the power dissipation on stationary particles is also around the same pW regime which leads to the assumption that the grown particles are not rigidly fixed on the substrate and rather dissipate energy through vibrations induced by the tip. While some trails of displaced clusters show a similar power dissipation to

stationary islands other manipulation paths appear darker in the phase signal relating to a power dissipation of around 5 pW. This corresponds to the energy needed to move an island. The difference of dissipation can be explained by the interaction of tip and particle. Some particles are moving by the first contact with the tip hence leaving almost no signal in the topography and showing a low amount of dissipated power. Contrarily, other particles stay in their position until the tip is on top of the Au island, imagining and exerting energy, until the dissipated power is enough for the island to disengage from the substrate, jumping to its new position before being manipulated again in the next line.

While the Nanowizard 4.0 by JPK is able to change the angle of scanning with its software, the cantilever with its tilt of 10 to 15° will not move over the surface parallel to the long axis which influences normal and lateral deflection. The sample must be turned physically to the required angle to maintain the same movement directions and therefore forces acting upon the tip.

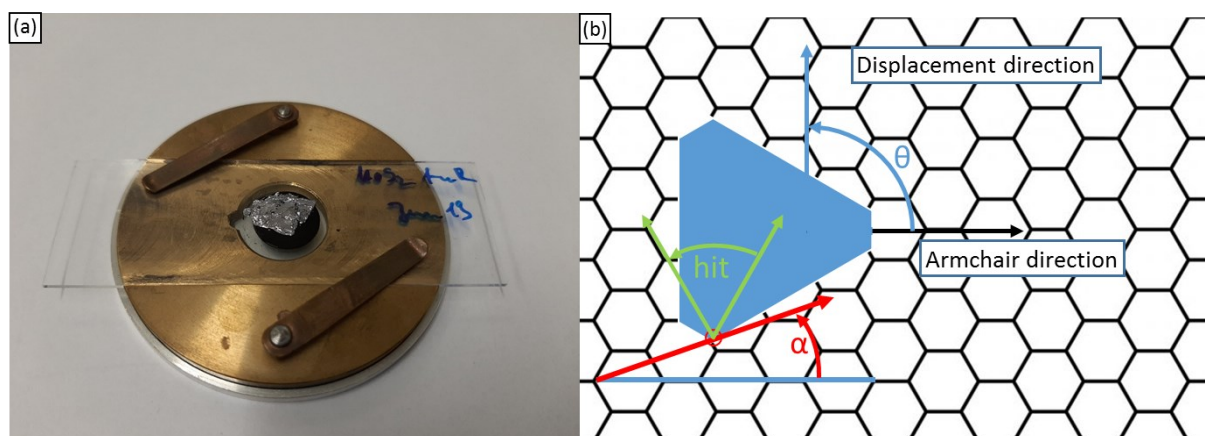


Figure 26: (a) Rotatable sample holder with mounted MoS₂ sample with free 360° rotation (b) Schematics of the manipulation experiment. The tip approaches the nanoparticle with a certain angle α which then is displaced with a generally different angle θ . Both angles are in reference to the armchair direction of the MoS₂ substrate. It is notable, that in a “scan-hit-move” sequence, the oscillating tip hits the corner region of the island and pushes it in an unpredictable direction identified by an angle γ , with $60^\circ < \gamma < 120^\circ$ (in green).

With help of a freely rotatable sample holder (Figure 26 (a)) the user is capable of turning the MoS₂ crystal full 360° without changing the tip movement direction thus allowing normal and lateral forces to act the same for every 10° difference in respect to scan angle and crystallographic angle of the sample. These measurements were done in ambient conditions using the same image size to maintain a line distance of 4 nm while scanning in a parallel line pattern recorded trace and retrace. Every scan was performed in a fresh area on the surface

with islands still located in their growth position. The half circle created by the 19 images separated by 10° cover all possible angles given by the hexagonal nature of the substrate lattice. From the substrates lattice point of view as a reference the angle of attack α defined in Figure 26 (b) now changes with respect to the MoS_2 lattice. The displacement direction θ is

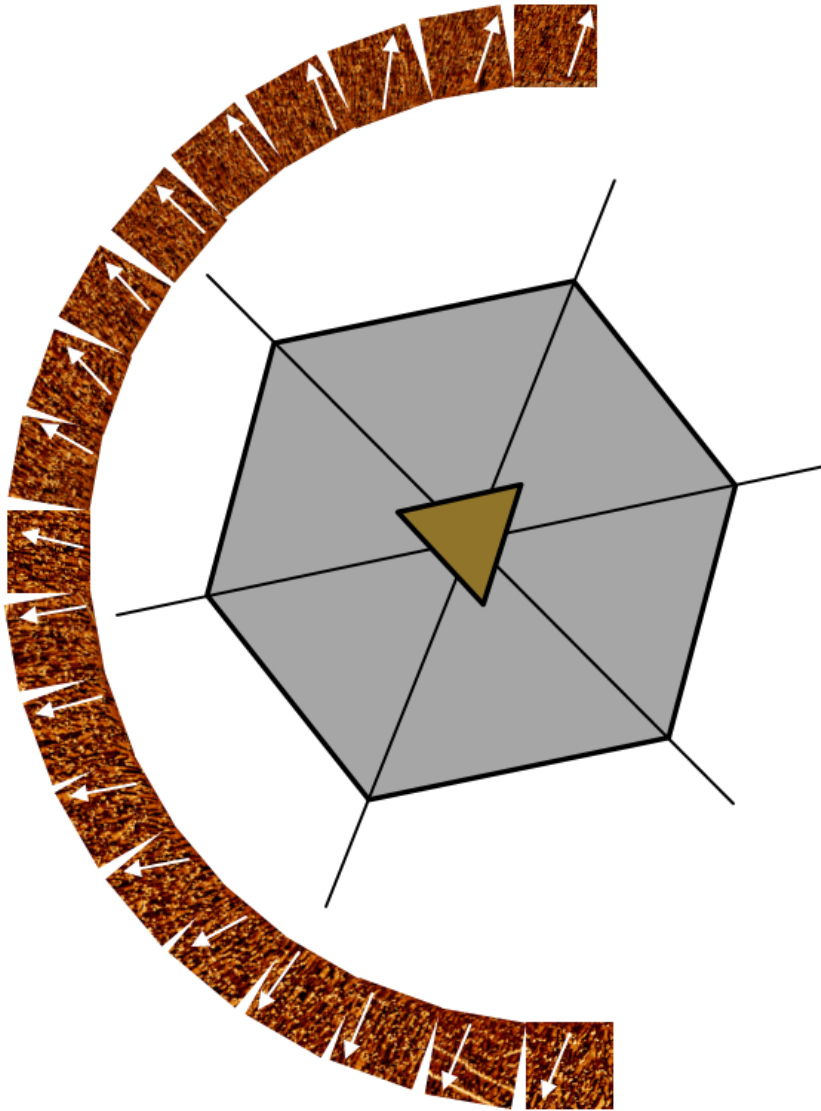


Figure 27: Manipulation images arranged with respect to the crystallographic orientation and the dominating displacement directions (white arrows). Note the change in displacement angle θ once the angle of attack α is closer to the next preferential crystallographic direction of the particle-substrate system.

recorded in the manipulation images visible as displacement trails of the moving particles.

Figure 27 illustrates the manipulation behavior of the Au islands in reference to the crystal orientation of the underlying lattice of MoS_2 . The white arrows in the vertical deflection images along the half circle indicate the prevailing direction of displacement. When put in perspective with the crystal lattice of MoS_2 and

its repeating angles of zigzag and armchair directions every 60° , it is clearly visible that the

displacement direction follows either the zigzag or armchair direction of the substrate underneath even when the angle α is changing. At certain points manipulated particles will change in an abrupt manner to the next crystallographic direction suitable for displacement. In the case of a point mass driven by an elastic spring the has been discussed several times in the literature, for example by Gnecco et al. [22] and Li et al. [92]. In the present case of

extended contact area, it also appears that the epitaxial relationship between Au islands and substrate is preserved during manipulation process.

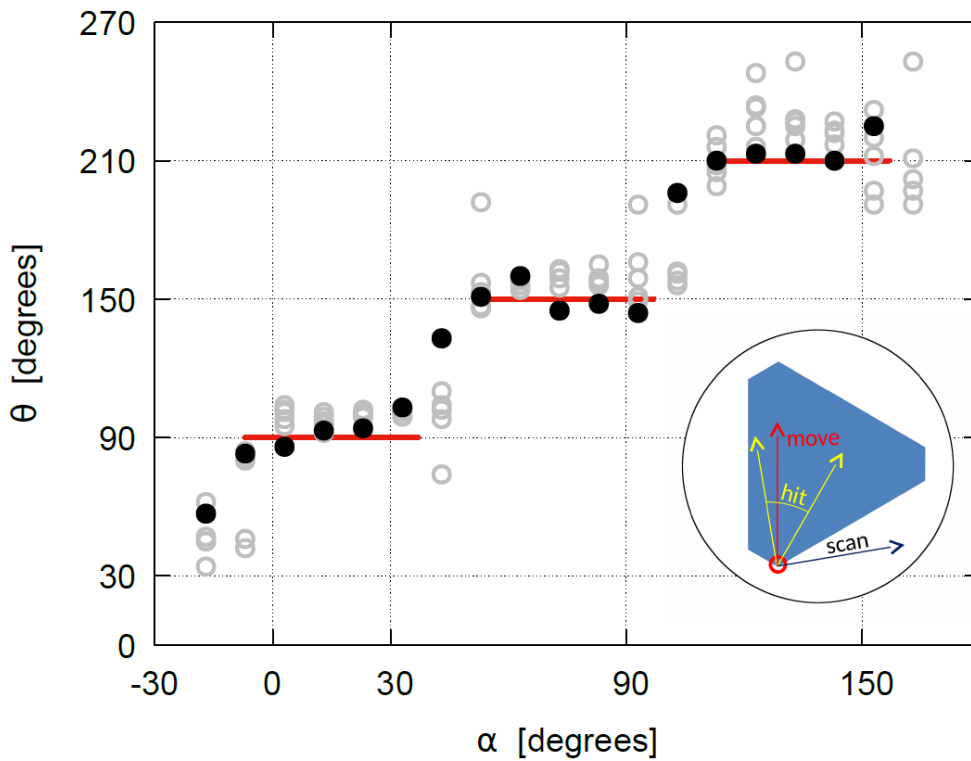


Figure 28: Preferential sliding direction of Au islands in tapping mode manipulation experiments as a function of the scan direction, defined by the angles θ and α from Fig. 19. The red segments highlight the locking directions every 60° .

Compiled into a graph this angular locking mechanism is clearly visible (see Figure 28). Every 60° the displacement direction is locked by the lower friction forces of the Au island sliding across the epitaxial hexagonal lattice of the MoS_2 substrate. In between the locking states of the zigzag and armchair direction the island is contested by both lower friction regime directions, leading movement behavior less straight, switching between different locking angles. This can lead to manipulation trails that do not comply with the established crystallographic directions.

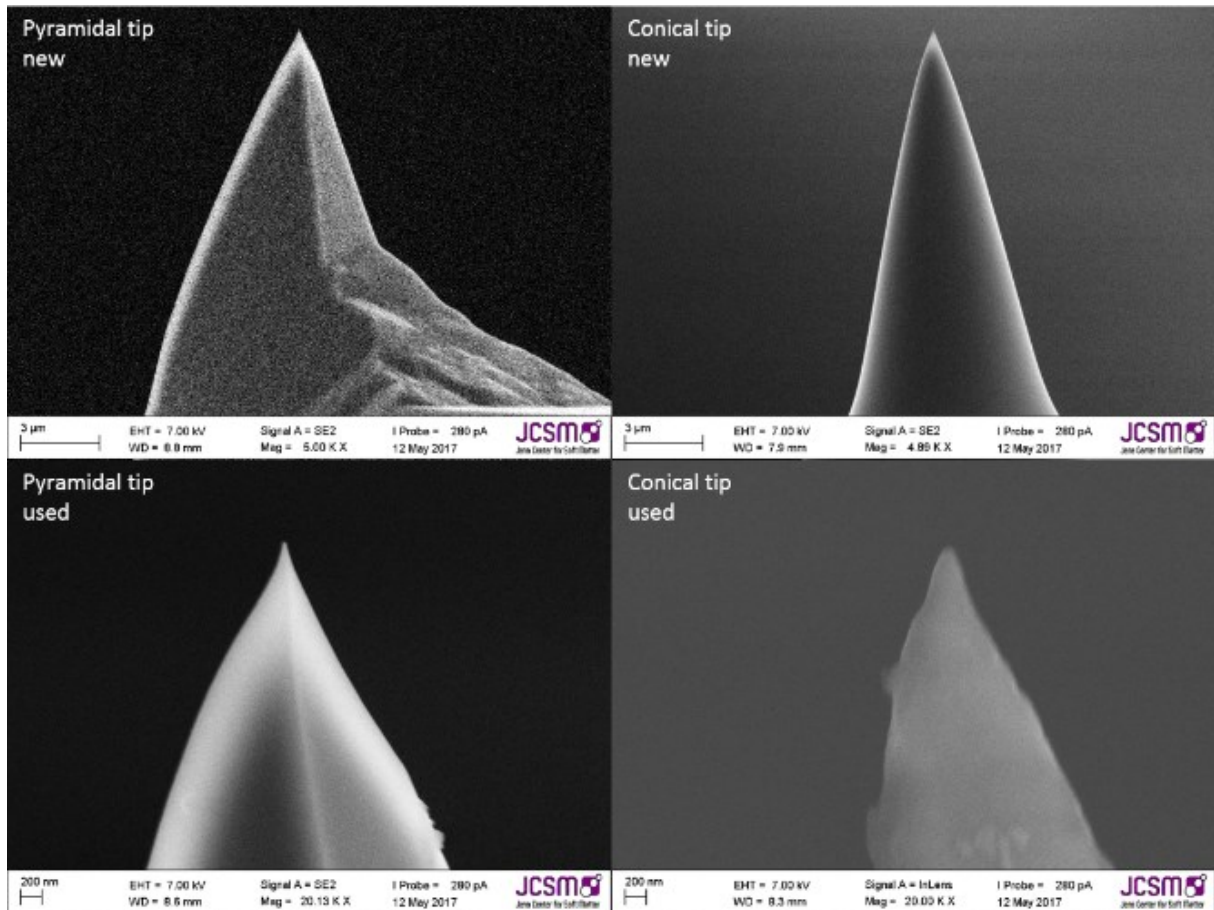


Figure 29: SEM images of the tips before and after manipulation of Au islands. The tip apices in of the pyramidal ContAIG by Budget Sensors and the conical CT300 by Team Nanotec show minimal wear after multiple manipulation scans in tapping mode.

The tip geometry of cantilevers used in the statistical displacement measurement set was a big concern regarding the influence of the pyramidal shape of the tip (Budget Sensors ConAIG) acting on the triangular symmetry of the particles manipulated. To rule out any directional control caused by this the same measurement set was performed using conically shaped tips (Nanotec CT300). There was no significant visible in the analysis of displacement angles, see below.

SEM images of the pyramidal and conical tips used for the experiments have been executed before and after manipulation to make sure that the degradation of the tips is minimal and no particles adhere to them, as seen in Figure 29.

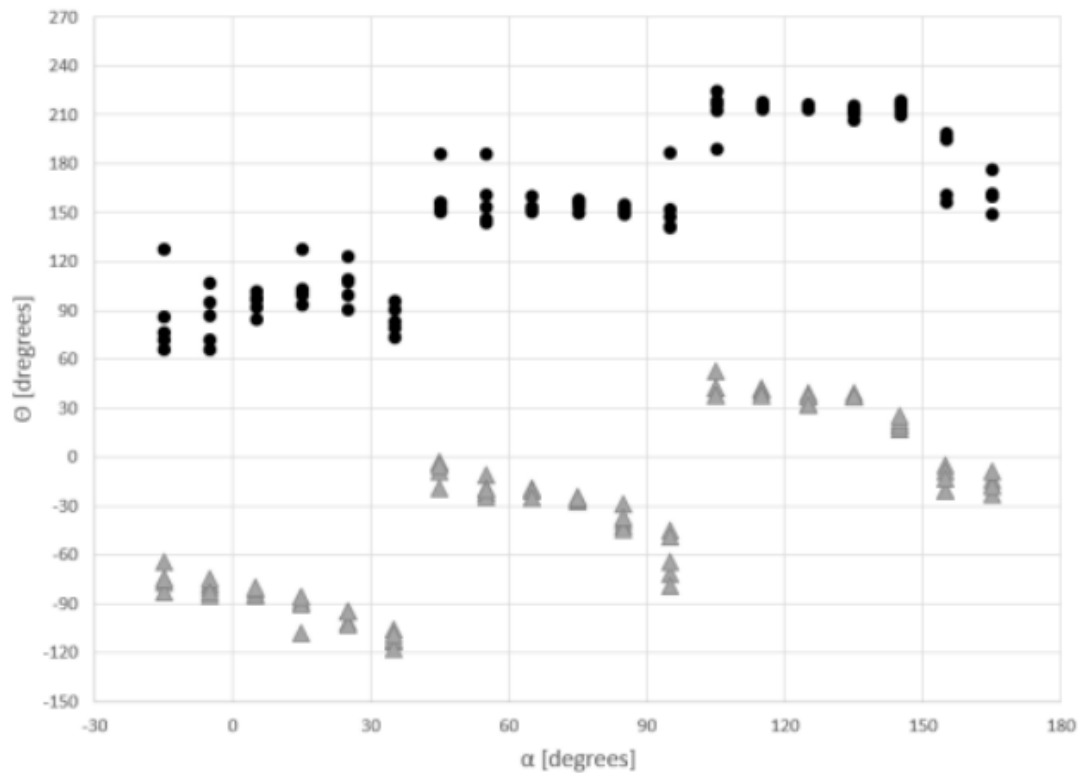


Figure 30: Preferential sliding direction of Au islands in tapping mode manipulation experiments using conical tips as a function of the scan direction, defined by the angles α for the angle of attack of the tip and θ as the angle of displacement and from Fig. 26. Directional locking occurs every 60° of θ confirming the negligible influence of the tip geometry on the manipulation directions. The downward scan is executed on a region where the islands have been previously manipulated by the upward scan. As a result, the manipulated islands are fewer, as their motion is hindered by clustering.

The diagram in Figure 30 shows the directional locking behavior of the gold nanoparticles when manipulated with a conical tip. As with the pyramidal tips the islands follow the crystallographic directions of the MoS_2 (θ) until the difference between the angle of approach α and the orientation of the substrate is big enough to switch to the next direction energetically suitable for the locking effect. This can be observed during manipulation with the slow scan direction oriented upwards (black circles) and also downwards (grey triangles). It is noteworthy that due to the technical operations of the JPK Nanowizard 4.0 AFM all downward manipulation scans were executed in the same area as the previous upward scans. Since these particles were already manipulated and partially formed immovable clusters of islands fewer islands were able to move freely over the substrate.

6.2 Theoretical Investigations and Simulations of the Au Island Pathways.

While the manipulation of other nanoparticles grown on MoS₂, as in Nita et al. [60] using amorphous Sb particles, have not shown any directional locking related to the substrate lattice, the results in chapter 6.1 show that there is evidence of tip induced rotation of nanoparticles. Due to the tip convolution of AFM imaging and the small size of the manipulated Au islands the resolution of single particles is not sufficient enough to completely rule out any rotation of islands during the displacement process. For these reasons MD simulations were deployed by Roberto Guerra to shed more light on the mechanisms behind the directional locking effect observed in experiments.

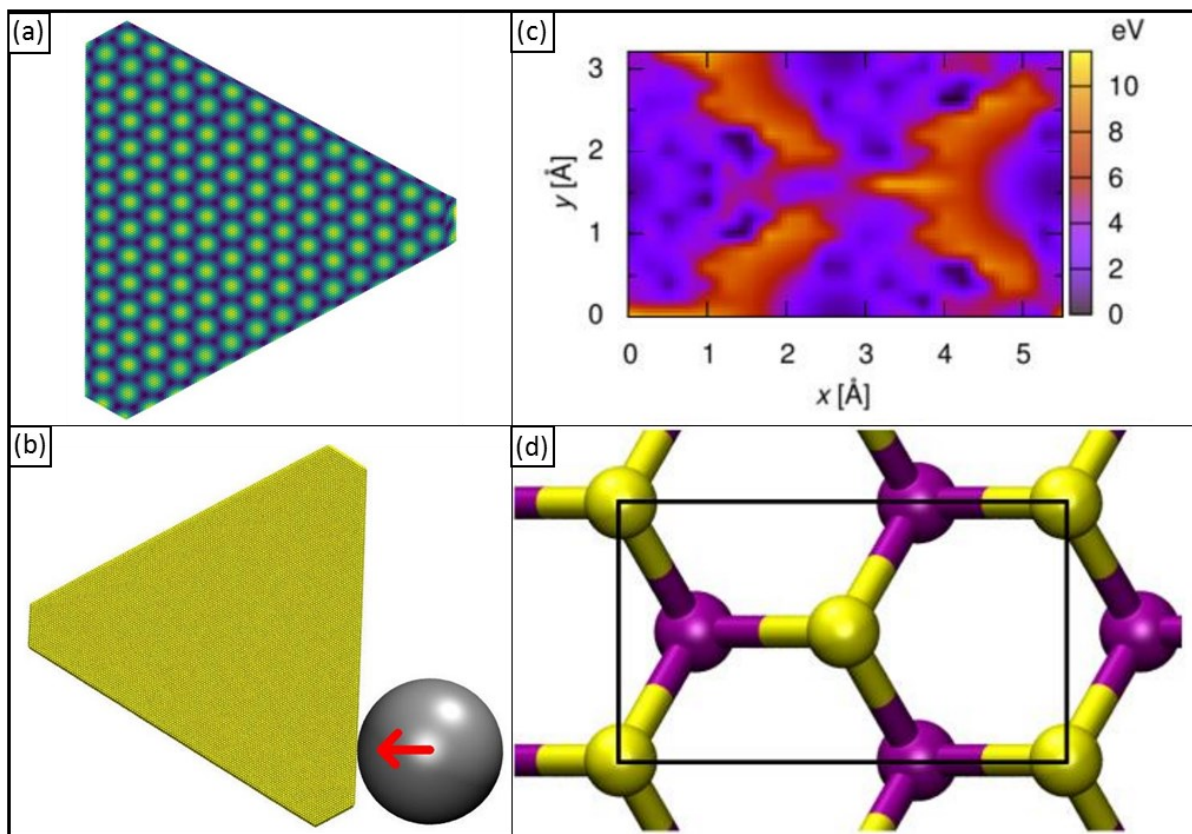


Figure 31: (a) Energy map of the Au-island contact face showing the solitonic pattern – corresponding to the moiré pattern in the unrelaxed system – arising due to the incommensurate interface with MoS₂. Each atom is colored as a function of its LJ interaction energy with the substrate, purple and yellow corresponding to low and high energy, respectively. Some distortion of the pattern at the boundary occurs due to relaxation effects.

(b) Sketch of a simulated repulsive cylinder (gray), mimicking the tip, pushing the island laterally as in experimental conditions. (c) A simulated PES map reporting the total potential energy (including the intra-island EAM potential plus the Au-MoS₂ Lennard-Jones energy) as a function of the Au-island constrained center-of-mass (x, y) coordinates. These (x, y) coordinates span the entire MoS₂ surface unit cell, while all other (internal) degrees of freedom are unconstrained and let relax in full at each point. (d) A sketch of the MoS₂ surface, with a black line delimiting the unit cell, and with Mo and S atoms represented in purple and yellow, respectively.

For the molecular dynamics simulations, a LAMMPS code was deployed [93] modelling an Au island fully reproduced by EAM potential [94] with a total of 63 615 gold atoms and a lattice spacing of 0.284 nm arranged in a solitonic pattern, as can be seen in Figure 31 (a). The island contains five fcc layers where the bottom layer with its 12 649 atoms forms a (111) face in contact with the substrate covers an area of $\approx 885 \text{ nm}^2$. The MoS₂ substrate was kept rigid in its bulk formation with a bond length of 0.316 nm. A Potential Energy Surface (PES) map has been simulated by recording the energy of the island in bulk fcc configuration in relaxation with a fixed center of mass (COM) at a discrete set of (x, y). A rotational energy profile was obtained in a similar fashion for different angles β , defined as a function of the COM distance from the starting point during manipulation, by depositing the Au island with the orientation of β and allowing atomic relaxation while at the same time nullifying the total torque to preserve β . For the gold-substrate interaction a 12-6 Lennard-Jones potential with $\epsilon = 22 \text{ meV}$ and $\sigma = 0.29 \text{ nm}$ was assumed [95].

In the MD simulations a truncated triangular island with an edge length of 40 nm sits in a relaxed equilibrium with its apex pointing in the armchair direction of the MoS₂ surface ($\beta = 0^\circ$). Without external forces acting on the simulated particle it will rotate spontaneously to align itself with the substrates crystalline direction, as can be seen in Figure 32 (c). Due to the substrates hexagonal lattice this sharp minimum of the angular energetics occurs at 0° and 60° , coinciding with the observed orientation of all grown Au islands in the experiments conducted. This would theoretically allow a rotation of up to 60° until the particle can lock into the next energy minimum. When manipulated in tapping mode in an experimental environment the triangular Au islands may experience a small rotation, but with the subsequent retraction of the tip the islands are allowed to return to their initial epitaxial orientation ($\beta = 0^\circ$).

For this possibility a simulation was launched featuring a repulsive cylinder mimicking the tip pushing the island in a lateral fashion, as can be seen in Figure 31 (b). When the tip is moved 6 nm with a velocity of 1 m/s the particle will rotate about 2° while its center of mass is moved by 5 nm. With the subsequent relaxation due to the tip retraction phase of tapping mode the particle will recover its initial alignment within ~ 1 ns. Extending this mechanism of movement and realignment leads to a displacement without any lasting rotation of the manipulated particles. It should be noted that the tip velocity in the simulations cannot be reduced much below the \sim m/s range. The imparted torque experienced by Au islands in the experiments is certainly much smaller since the tip velocity of about $2 \mu\text{m/s}$. With the fact in mind that the island orientation automatically adjusts its position after contact with the tip, the simulation can be operated with a lateral force $F \approx 20$ nN applied uniformly to all atoms of the simulated gold island. The angle of displacement γ defined by the average direction of motion of the particle is varied between 0° and 180° .

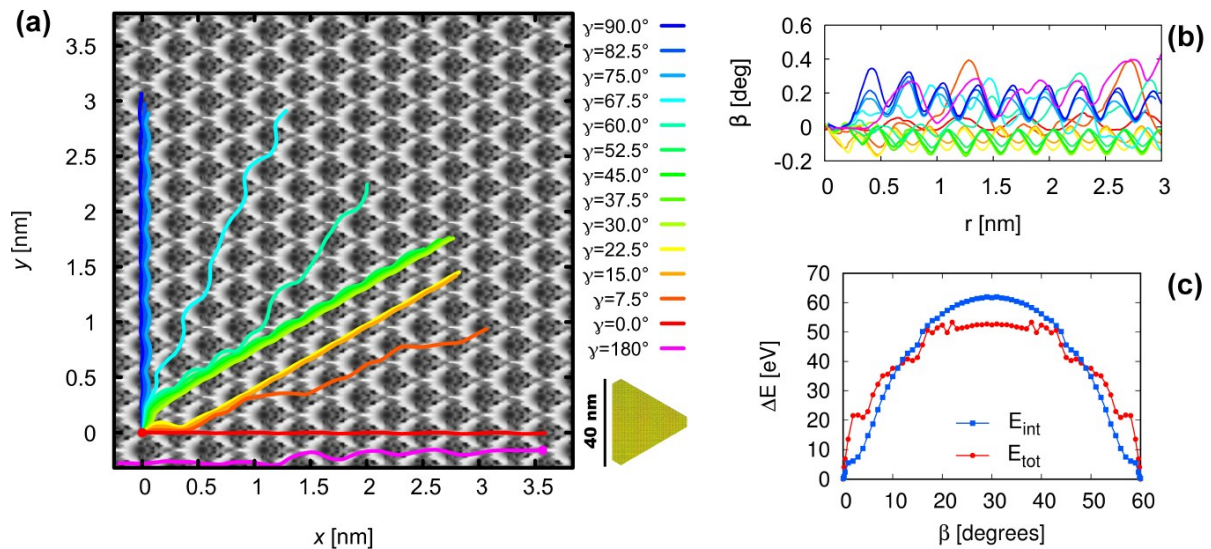


Figure 32: (a) Simulation of pathways of the island COM on the computed PES map of the MoS₂ surface (grayscale) for different directions of applied force γ . Inset: the initial configuration of the island. (b) Island orientation β as a function of the COM distance from the starting point during manipulation reported in panel (a). (c) Red dots represent a function of the island orientation angle β on MoS₂, the simulated total energy E_{tot} including Au-Au and Au-MoS₂ interaction energies. Blue squares represent the sole Au-MoS₂ interaction energy contribution E_{int} .

As shown in Figure 32 (a) with the varying angle of attack γ the simulated Au islands tends to prefer the zigzag direction of the substrate. When moving in $\gamma = 0^\circ$ or 180° the particle follows

the armchair direction $\theta = 0^\circ$ in an almost straight line, but just a slight change in the attack angle (copper colored path way of $\gamma = 7.5^\circ$) leads to a rather meandering path of the nanoparticle, switching between armchair and zigzag direction. In the range of $\gamma = 15^\circ$ and 52.5° the directional locking phenomenon occurs, trapping the displacement direction at $\theta = 30^\circ$ which corresponds with the zigzag direction of the MoS₂ substrate. This occurs again with $\gamma \geq 75^\circ$ where the next zigzag direction of the hexagonal structure acts as an attractor to the COM of the Au island.

These results confirm the directional locking effect observed in the experiments done on bulk MoS₂ and also highlight the preference of zigzag over armchair direction. The PES map of the substrate also indicates a strong rotational asymmetry which can be seen in the trajectory shape when the island is pushed in $\gamma = 0^\circ$ and $\gamma = 180^\circ$.

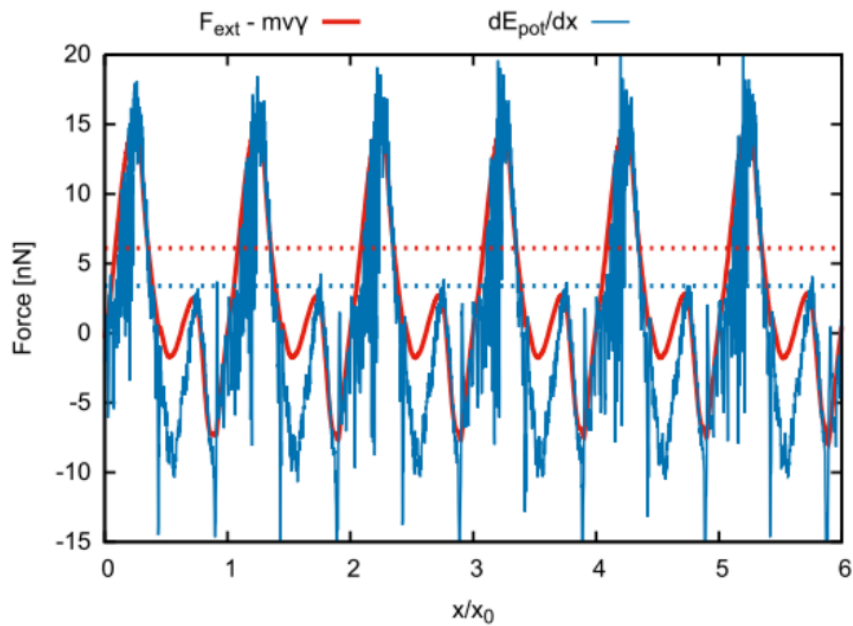


Figure 33: Force traces obtained for the simulated island advancing in direction $\vartheta = \gamma = 0$. The red-curve estimate is obtained by subtracting the center-of-mass viscous-force term from the total applied external force. The blue-curve estimate is the derivative of the Au-MoS₂ interaction potential along the sliding direction x . Displacements are normalized by $x_0 = 548$ pm, namely the x -size of the MoS₂ unit cell (see Fig. S3). Dotted lines at 6.1 nN and 3.4 nN mark the average values of their respective estimators, which should coincide in the adiabatic limit of vanishingly small island velocity. In the reported simulations, with the applied force $F \approx 20$ nN, the average island speed is in the 0.6–0.7 m/s range, depending on the sliding direction. For this specific angle $\vartheta = \gamma = 0$, the average speed is 0.7 m/s.

With a maximum simulated PES corrugation of 11.5 eV and the average friction force of about 4.5 nN during manipulation, the corresponding shear stress is $\tau \approx 5$ MPa. This is a much higher friction barrier than the observed 0.2 MPa of amorphous Sb islands sliding over MoS₂ by Nita et al [60], even when taking reduction of shear stress through thermolubric effects at room temperature in account. Another interesting movement behavior is observed in the simulation by monitoring the COM rotation β as a function of distance of the center of mass from the starting point r . As can be seen in Figure 32 (b) for all angles of attack γ the absolute rotation stays well below 0.5° but also show a regular wobbling motion with a small wave length of about 0.3 nm. This motion occurs in the range of values corresponding to perfect directional locking but it also happens when $\gamma = 7.5^\circ$ featuring two angular peaks when alternating the sliding direction between armchair ($\theta = 0^\circ$) and zigzag ($\theta = 30^\circ$) direction.

6.3 Nanomanipulation on Monolayer and Bilayer MoS₂

Using large MoS₂ triangles introduced in chapter 5.1.1 as a substrate for subsequent nanomanipulation on gold cluster brings inherent advantages with it. While experiments on bulk material required high resolution atomic scale imaging with STM or AFM to determine the lattice orientation, on synthetic monolayer MoS₂ the relevant armchair and zigzag directions can be determined by the shape of the monolayer [85]. This reduces set up time immensely by eliminating the needed cantilever and/or AFM head exchange to achieve atomic scale resolution. Since the MoS₂ crystals are randomly oriented on the Si/SiO₂ wafer a rotating stage to change the angle of the sample is not needed and crystals in the required direction can be found either with the use of the optical microscope attached to the AFM or with a large overview scan in the tens of microns.

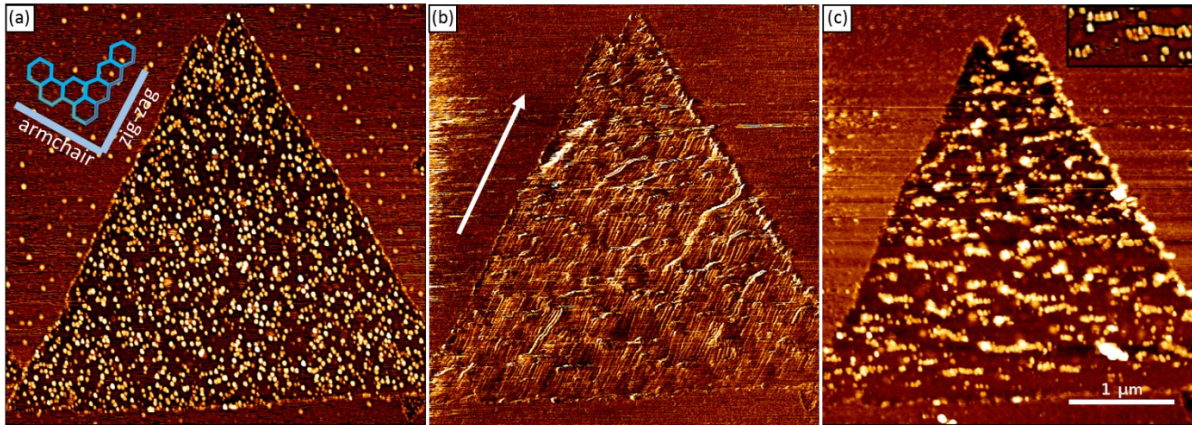


Figure 34: Typical manipulation sequence for the monolayer-MoS₂-Au-system (a) height image in tapping mode showing the initial positions of all Au islands (size a ~10 nm) on the MoS₂ triangle with an Au cluster density of $n = 6.5 \times 10 \mu\text{m}^{-2}$. The schematic in the top left corner illustrates the hexagonal structure and the two dominant crystallographic directions adjusted for the orientation of the island. (b) Lateral deflection image of the manipulation in contact mode (10 nN) with scan line spacing of 7.8nm using a stiff tapping mode tip with activated hover mode. The white arrow indicates the most prevalent displacement direction which coincides with the zigzag direction of the substrate. (c) Tapping mode image after manipulation showing the formation of regular bands of Au islands every 250 nm, parallel to the fast axis of the AFM. The close-up in the top right corner suggests a band formation by pushing triangular Au islands together with their initial growth orientation preserved.

As with bulk MoS₂, the phenomenon of directional locking applies also here to the manipulation of grown Au islands. Figure 34 illustrates a typical manipulation experiment of monolayer samples. With the full substrate triangle in view all crystallographic directions can be easily identified for later determination of displacement directions. First, a tapping mode image is acquired using a PPP-NCHAu cantilever by Nanosensors. With a low set point 22 nm it is ensured that nano islands remain in their initial growth location and all positions of particles are being recorded. Afterwards the manipulation sequence is executed with the same tip in contact mode with activated hover mode set to 50 nm. With that, manipulating forces will only act on Au islands while recording the trace signal on the fast axis (x axis) going from left to right. The tip will automatically retract 50 nm on the way back from right to left to its initial starting position of the scanned line, hence the forces experienced by nanoparticles are only coming from the same direction. While non-contact cantilevers with their short and therefore stiff beams are not the best tool for contact mode manipulation it allows the user to quickly image, manipulate and reimage a certain area without changing cantilevers and the subsequent calibration and localization of the manipulated area.

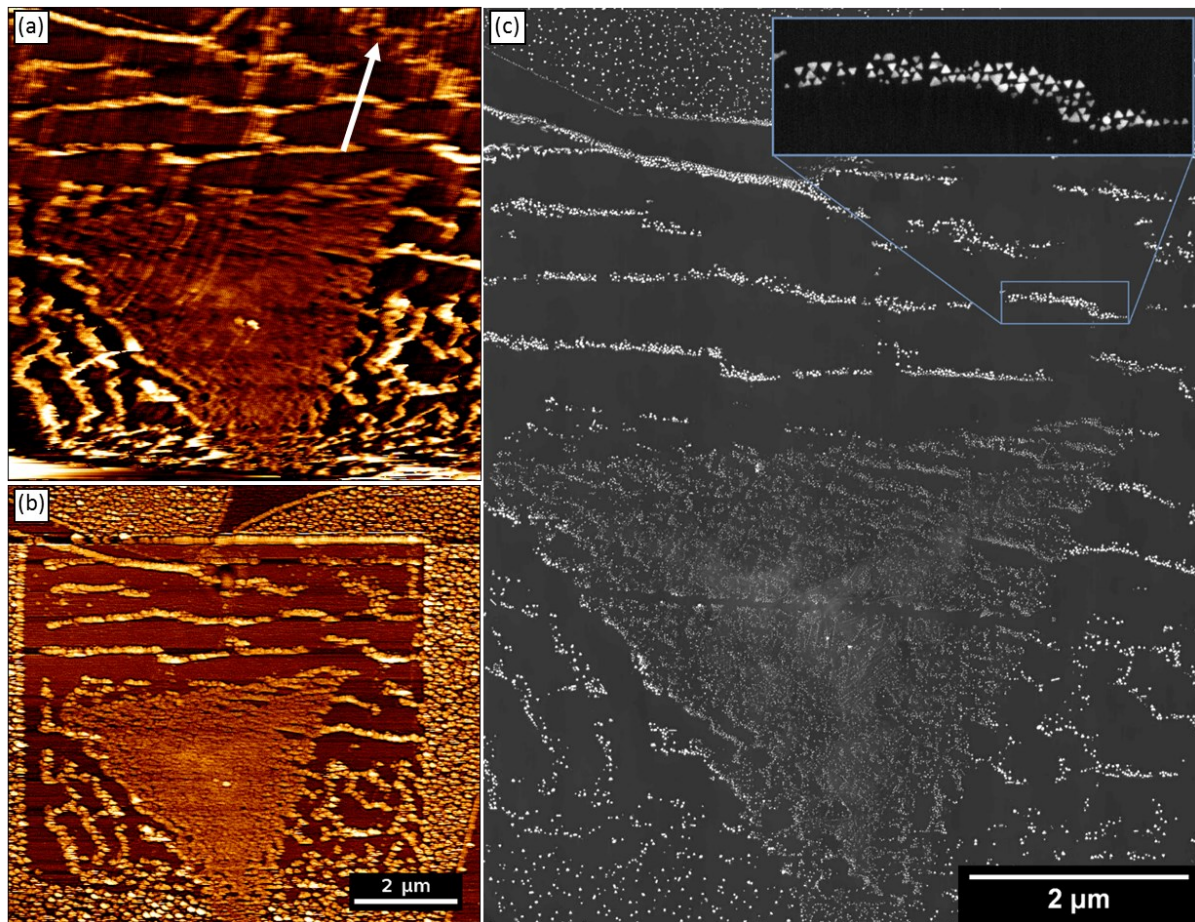


Figure 35: Manipulation on monolayer and bilayer MoS₂. (a) Topography image of the contact mode manipulation with a normal load of 29 nN, a line distance of 13.7 nm and 50 nm hover mode activated. The white arrow indicates the prevalent displacement direction, parallel to the armchair direction of the substrate. (b) Tapping mode image with a relative setpoint of 22.5 nm of the manipulation result. The Au islands on the monolayer appear to form bands with a distance of 550 nm to each other. Nanoparticles on the second layer appear much smaller and in higher density with almost no significant displacement by the tip. Cluster density and average size before manipulation: $n = 102 \mu\text{m}^{-2}$; $a = 17 \text{ nm}$ on the first MoS₂ layer; $n = 9 \times 10^2 \mu\text{m}^{-2}$; $a = 7.2 \text{ nm}$ on the second one. (c) SEM BSED image of the manipulated area. The actual size and density of particles is now visible (no tip convolution), showing bands of Au islands on the monolayer either parallel to the fast axis or to the zigzag direction of MoS₂. The close-up shows the displaced islands in epitaxial orientations with most of them not in direct contact with each other. Particles on the second layer show some displacement in a similar fashion but overall less movement due to the particle density.

Similar to the manipulation experiments on bulk MoS₂ the monolayer material exhibits still a direction locking effect along the crystallographic directions of the hexagonal structure. However, with the different substrate thickness comes a new phenomenon of the band formation of Au islands. These rows of particles form during manipulation in contact mode and can be over 10 μm long, depending on the size of the substrate crystal with inter-band spacing of around 500 nm. Smaller MoS₂ triangles exhibit also exhibit a smaller distance

between the striations of nano objects. The orientation of these appear to follow either a crystallographic direction of MoS₂ (zigzag or armchair) or form parallel to the fast axis of the AFM.

While post-manipulation tapping mode AFM images show a closely packed string of Au islands with a width of 1 to 3 particles, as can be seen in Figure 34 (c) close-up, the tip convolution of the AFM probe obscures the reality of the particle bands. High resolution SEM images (Figure 35 (c)) reveal that displaced particles packed in a line not only retain their epitaxial orientation from the growth process but also rarely connect to each other. The close-up shows a detailed image of the composition of an Au band with the nano objects at a distance of one to a few nanometers to each other. Multiple phenomena could be responsible for this effect. On one hand electrostatic repulsion among gold clusters might be the culprit, as studied by Ju et al. [96] using DFT to show the possibility of electron transfer from MoS₂ to Au clusters and the influence of Sulfur vacancies on the Au particle adsorption. Another reason for the nanoscale spacing might be the roughness of the Si/SiO₂ wafers used for the monolayer deposition. While the wafers are indeed very smooth, compared to atomic smoothness of crystalline materials they appear relatively rough, as is clearly visible in the cross-section TEM images obtained for this work. In Figure 20 (a) and also Figure 21 (a) the wafer shows a roughness of up to 2 nm which is a quarter of the Au islands height. A third aspect might be the effect of puckering mentioned in chapter 5.1 where a tip by scanning in contact with a few-layer lamellar surface creates so-called puckers around itself due to the low inter-layer forces and bending stiffness. Especially pronounced is the puckering on one or few layers of MoS₂, whereas thicker material is strengthened and exhibits less elastic deformation. The study by Cao et al. [97] recorded friction forces with a standard AFM tip, observing a bigger puckering effect with increasing normal load. In the case of the manipulation of Au islands on monolayer MoS₂ the situation is more complicated. While the tip scans with a normal load of $F_N = 50$ nN in contact mode the substrate area around the tip should show elastic deformation in shape of a wave in front of the tip. While a gold nanoparticle itself does not extrude a normal force into the underlying MoS₂, the deformation created by the tip might have an influence of the contact between tip apex and Au island. The then moving island could possibly create its own wake in front of it, with the van-der-Waals forces between gold and the substrate deforming the monolayer. In the case of an upcoming collision of the displaced nanoparticle with another this fold might stop the manipulated particle from connecting with the stationary Au island,

creating the gap observed with the SEM. However, this hypothesis is in need of more computationally extensive MD simulations to provide more insight.

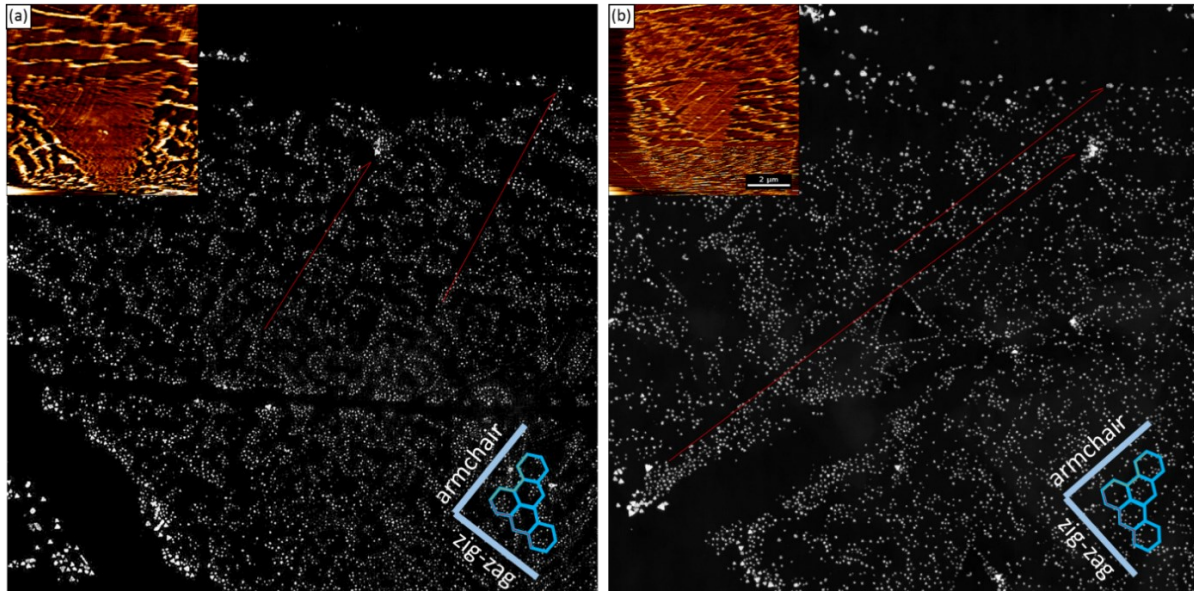


Figure 36: SEM images of the second layer of MoS₂ showing results of the manipulation sequence with the upper left corner showing the topographies of the AFM manipulation. (a) Au islands on the second layer are grown in relatively high density which inhibits far displacement and the formation of nanoparticle bends. Two trails of bigger Au islands travelling onto and over the bilayer can be observed. (b) Manipulation on another MoS₂ triangle. The red arrow indicates the pathway of a bigger Au island which then plowed through the dense but small gold particles of the second layer, eventually getting stopped by the pile-up.

The second layer of MoS₂ provides a very different environment for the growth of gold nanoparticles. With an average size of 7.2 nm and a density $9 \times 10^2 \mu\text{m}^{-2}$ for Au islands it is apparent that the second layer cannot provide the same mobility for gold atoms during the 30 min annealing time in the UHV chamber. To grow bigger clusters of gold the surface homogeneously covered with dispersed gold atoms needs to provide enough mobility to let atoms travel to a seed for a growing gold cluster which is evident for monolayered MoS₂ as well as for bulk. Reason for this might be the observed permanent dipole formation in odd number of layers of MoS₂ reported by Lavini et al. [83]. The higher particle density prohibits nanoparticles to travel relatively far distances without coming in contact with another, as for the case of monolayer MoS₂. This explains the lack of striation which stands in stark contrast to the first layer of the very same substrate flake. However, in Figure 35 (c) the upper right corner of the second layer triangle indicates the beginning of stripes of nanoparticles forming.

Interestingly in both cases of very large MoS₂-crystals with a developed second layer at the center, bigger Au islands possibly from the first layer have observed overcoming the step edge of 1.5 nm to traverse onto the second layer as indicated by the red lines in Figure 36. Here they travel directionally locked without getting repelled by the smaller gold crystals but rather plowing through them, creating a visible trail. In Figure 36 (b) two islands can be seen stuck in a pile of smaller gold clusters in their epitaxial orientation. But in difference to manipulation on a monolayer, the bilayer-nanoparticles appear to be in direct contact with the large islands and do not provide a gap.

7 Gold Nanowire Formation

7.1 Re-Annealing of Manipulated Au Islands

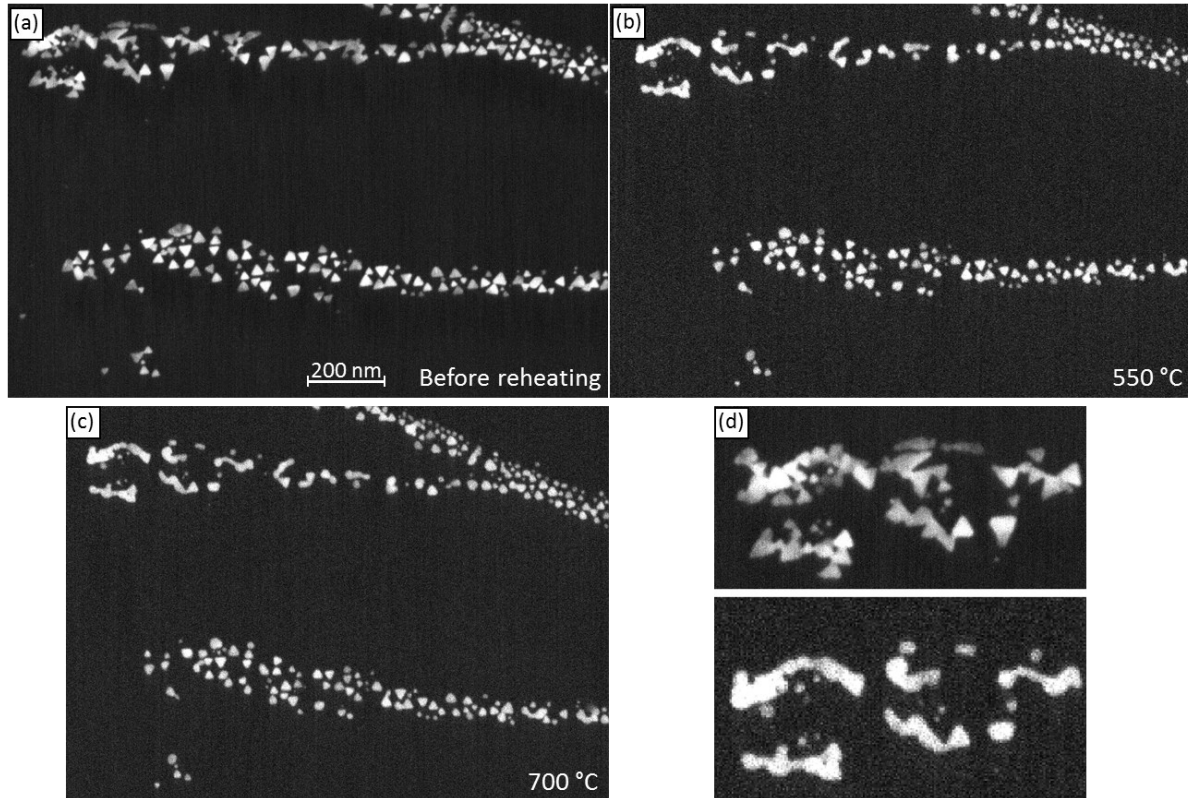


Figure 37: SEM images of the fusion experiment after manipulation (see Figure 35 (a) A band of Au islands on monolayer MoS₂ before reheating. Epitaxial orientation is clearly visible in well-shaped nanoparticles. The upper left corner shows less defined particles. (b) After reheating in the UHV chamber at 550 °C the lower Au stripe shows insignificant change to the particle structures. The upper band indicates a higher mobility of gold with the less well-defined gold crystals melting together. (c) Result of reheating the same area to a temperature of 700 °C shows no change to the previous temperature. (d) A close-up of the area with most significant change after reheating to 550 °C shows the formation of small nanowires with lengths of 150 to 200 nm.

Size dependent melting temperature of nanoparticles is a well-studied phenomenon in science finding a logarithmic increase of the melting point with the volume of metallic nano objects. Gold clusters of a size of 2.5 nm have been found to liquefy at a temperature of above 700 °C, while bulk gold melts at 1064 °C in atmospheric pressure [98]. One of the factors for this behavior is the fraction of atoms at the surface of a body which changes with the volume of said body since the surface scales with the radius r^2 and the volume with r^3 . While inner-body atoms can exist in a low energy state forming all necessary bonds with each other to

create a highly coordinated crystal lattice, corner-, edge-, and surface-atoms exhibit a higher degree of free energy and therefore an affinity to form other bonds with adsorbate molecules for example. This low stabilization caused by the inherent low coordination is one of the main factors for catalytic activity. With a higher percentage of atoms at the surface, edges and corners the point phase transition becomes less sharp and well-defined. Rather than individual phases it is easier to understand the behavior of nanoclusters as molecules with coexisting structural isomers over a range of temperatures. This becomes visible for the observed nanoparticles, showing a loss of their geometric shape, rounded off corners and generally reconfiguring into a more spherical shape. Especially less-defined Au clusters with an inherently less stable configuration and therefore higher degree of free energy become more mobile and even melt together to form nanowires with lengths between 150 to 200 μm . However, the results of the re-annealing experiments suggest that better ordered gold crystals with distinct triangular shape and spacing of one to two nanometers in between each other appear to experience a smaller amount of gold mobility brought by the reheating process in UHV. Most of these islands cannot overcome their energetic barriers to let gold atoms escape the crystalline structure which inhibits the welding process between islands.

7.2 Nanoscratch-based Surface Modification

As discussed in the last chapter, the formation of joined nanowires through manipulation and subsequent reheating proves to be more difficult thanks to effects like electrostatic repulsion during displacement and thermal stability of well-crystallized nano islands. At this point the modification of the crystal substrate becomes a viable option to overcome these obstacles.

The parallel work performed by Özoğul et al. in our work group explores the behavior of monolayer and bulk MoS_2 substrate when scratched with a single-crystal diamond tip with normal forces between 1000 nN and 3000 nN and varying velocities [99]. It demonstrates that the high forces of at least 2 μN to break the surface layer of both bulk and monolayer material. Once the diamond tip penetrates the material a plowing-induced exfoliation phenomenon appears, similar to a ship bow gliding through water. Here, the sides of the tip force the broken-up layers to bend upwards, subsequently creating curls of MoS_2 or even exfoliating relatively large flakes of the lamellar material and folding them over. This process is much

more pronounced for bulk material since many more layers of MoS₂ will be penetrated and bent by the tip, going up to 10 nm (for 3 μN) into the material. The created agglomerates, curls and peels cover large areas up to 3 μm around the scratch, building up material in regime of up to 100 nm. Interestingly the hexagonal substrate ruptures along the crystallographic directions, namely armchair and zigzag direction, as can be clearly seen in Figure 38 (a) for bulk MoS₂ and for monolayer material Figure 39 (b) below.

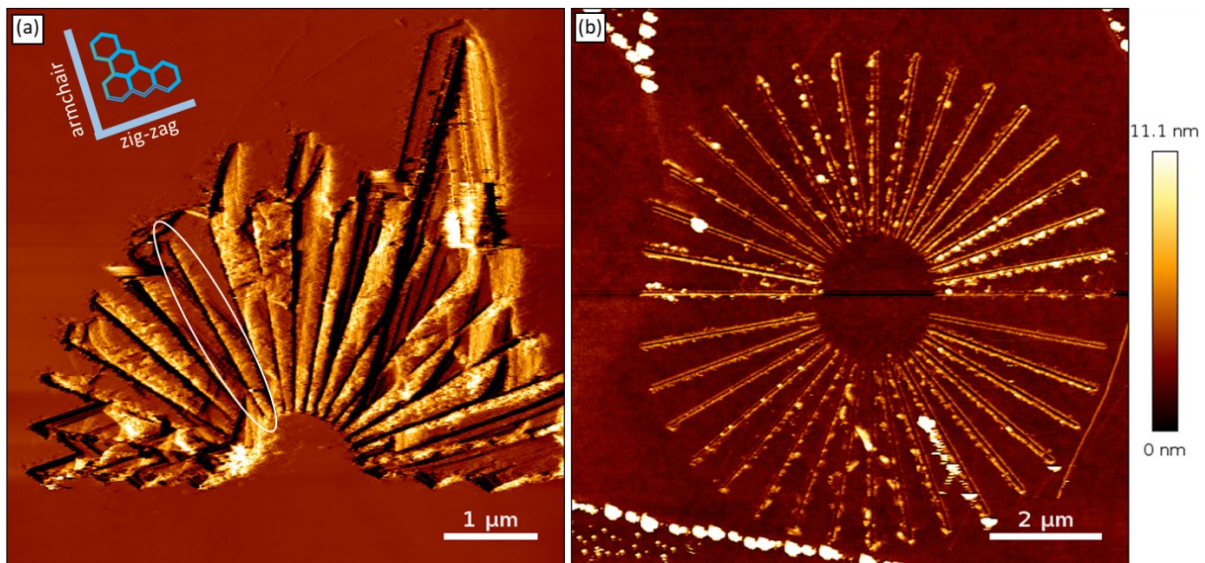


Figure 38: Radial nanoscratches with a single-crystal diamond tip. (a) Vertical Deflection image of a half circle (every 10°) of scratch profiles with a force of 2 μN on bulk MoS₂. Certain directions lead to a large amount of exfoliation up to 100 nm in height while others exhibit minimal damage around the trench (scratch parallel to armchair). (b) Topography image of a full circle (every 10°) of nanoscratches with 2 μN on monolayer MoS₂ showing similar signs of exfoliation with varying degree of surface damage depending on the orientation of the scratch profile. Due to the thickness of the material curls of MoS₂ does not exceed a height of 12 nm. (unpublished)

The extensive research in to scratch behavior and crack propagation done in [99] reveals many implications for any crystalline surface modification by nanoscratching. For bulk MoS₂ especially large spill outs have been observed with step edges created by folding over multiple layers of the lamellar material similar to pages of an open book. High interplanar strength and low binding forces in between the individual layers allow for sliding and bending, the very same reason MoS₂ is an excellent dry lubricant. However, in the case of scratch patterning of the surface this leads to high forces necessary to break the surface layer with a normal load of at least 2 μN. The tip subsequently penetrates multiple layers and acts as a plow which

causes the individual layers to rupture along the crystallographic directions with the weakest binding energy, namely armchair and zigzag direction [100]. Depending on the angle of the scratch and the preferred rupture lines this creates very large folds covering μm^2 and heights of up to 100 nm while the scratch itself is not deeper than 6 nm. In Figure 38 (a) a half circle of radial nanoscratches was performed using a D300 single-crystal diamond tip and a normal force $F_N = 2 \mu\text{N}$. While the scratches change with 10° in their orientation the spilled-out material folds in predominant directions due to the directionally locked rupturing, leaving behind a clear indicator to determine the crystallographic directions of the bulk material. It is also noteworthy that scratches performed in alignment with armchair or zigzag direction show almost no damage in the area surrounding the created trench. This can be seen in Figure 38 (a) highlighted in white.

Synthetically grown monolayer MoS_2 performs in a similar fashion when scratched with a diamond tip. Even though the tip can only break through a single layer before reaching the Si/SiO₂ wafer folds and chips of MoS_2 in preferred crystallographic directions have been observed. However, the surface damage to the modified area is much lower in comparison to bulk material, as Figure 38 (b) illustrates with a set of 36 radial scratches arranged in a full circle. As with bulk MoS_2 , scratches parallel to crystallographic directions leave very little agglomerated material next to the trench while other scratches show build-up with heights up to 12 nm.

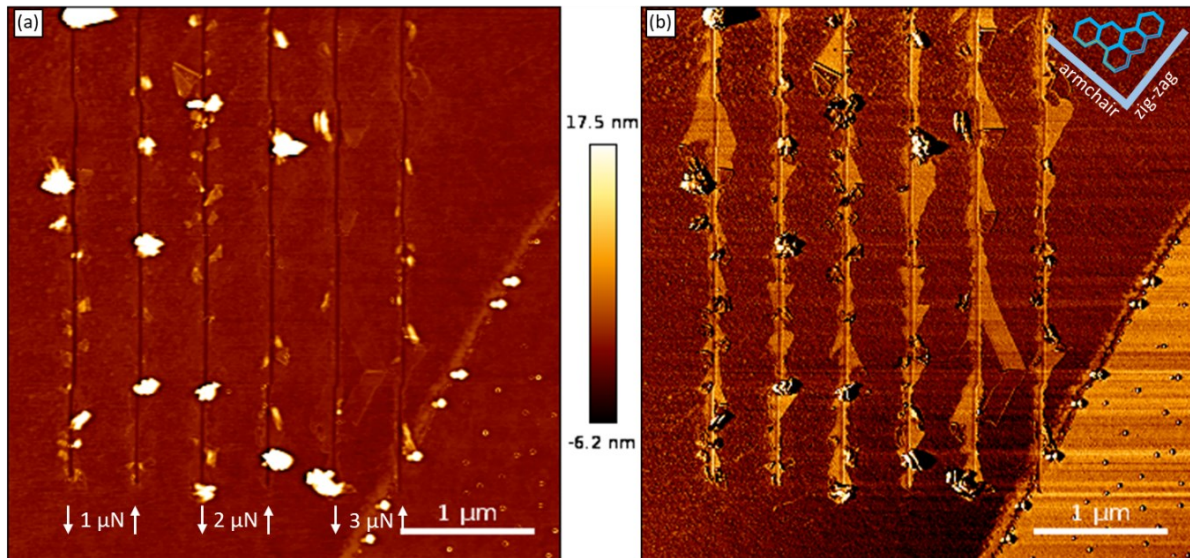


Figure 39: A set of 6 parallel scratches with a length of $5\ \mu\text{m}$ performed with varying forces and alternating directions at an angle of 30° to the zigzag direction of the monolayer MoS_2 substrate. (a) Topography image with a scan angle of 90° reveals build-ups with heights of up to $17\ \text{nm}$ in irregular fashion. (b) The phase image highlights the different materials, revealing the SiO_2 surface underneath peeled-off monolayer MoS_2 . The ruptures occur along crystallographic directions of the substrate and exfoliated material folds in an epitaxial manner onto the monolayer.

Taking a closer look at the exfoliation of a single layer during nanoscratch experiments, certain characteristic properties can be observed. The diamond tip is still in need of a high normal force F_N of $1\ \mu\text{N}$ to break through the monolayer, subsequently penetrating the Si/SiO_2 wafer to about $6\ \text{nm}$ pulverizing wafer material in the process. Once the tip reaches the required normal force, it acts as a plow cutting the monolayer with subsequent crack propagation consistent with previous research. Molecular Dynamics simulations by Wang et al. suggest a smaller surface energy in zigzag direction of MoS_2 leading to cracks preferring that specific angle [100]. Another noteworthy result is the influence of a changing scratch direction on the rupture process during mechanical stress. When extruding force along zigzag direction the fracture will run along the same direction. However, if the direction of the scratches is adjusted to another orientation cracks will propagate along the next zigzag-orientation closest to the force applied and in addition, a wrinkle made from buckled MoS_2 develops along the rupture on the opposite side of the zigzag fracture. This exact fracture behavior has been observed in [99] during plowing induced nanoexfoliation of mono- and multilayer MoS_2 , with curls and wrinkles developing on one side of the nanoscratch and fractures combined with exfoliation on the opposite side, hence confirming the zigzag direction of MoS_2 as the least destructive direction for surface modification. However, while this study suggests the

formation of curls on only one side of the scratch is due to the geometrical asymmetry of the diamond tip used to penetrate the layers, Wang et al. [100] attributes the effect to wrinkle formation depending on the angle of attack in relation to the crystal lattice orientation of MoS₂. The scratch experiments also confirm the modeled fracture propagation with cracks forming along the closest zigzag orientation in the general direction of the tip cutting through the material, showing a distinct triangular exfoliation pattern. Figure 39 (a) shows the topography after performing 6 nanoscratches with alternating scratch direction and varying normal forces F_N on monolayer MoS₂, while the phase signal in Figure 39 (b) highlights this effect very clearly with the propagation of cracks following the zigzag directions closest to the angle of attack of the diamond tip. The SiO₂ underneath gets revealed after the tip exfoliates the single layer and folds it over.

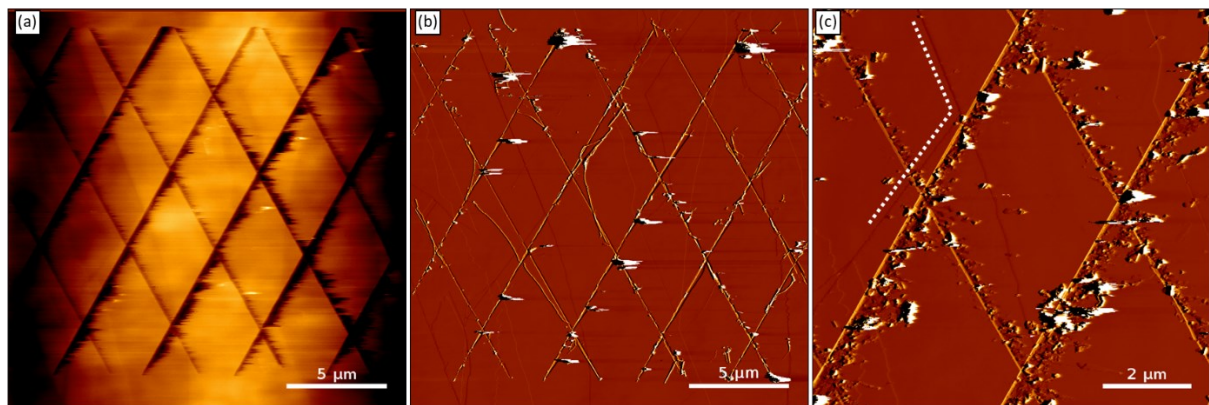


Figure 40: Nano pattern along the zigzag direction of the bulk MoS₂ substrate applied with a D300 single-crystal diamond tip with a normal force F_N of 2 μN and a velocity $v = 1 \mu\text{m/s}$. (a) topography image of the atomically smooth substrate surface showing no significant spill-out from the scratches. (b) The amplitude tapping mode image of the same region revealing a greater amount of surface contamination but in relatively small size. (c) Amplitude close-up image of the patterned surface with step edges (dotted white lines) in between as an indicator for the orientation of MoS₂ shows a misalignment of 7°.

Applying the gained knowledge about MoS₂ rupture and crack and wrinkle propagation to bulk material relatively clean scratches with force of 2 μN can be performed when the crystal orientation of the substrate is determined beforehand and the nanoscratches follow the zigzag direction, as can be seen in Figure 38. For this experiment a half circle of radial scratches was performed to determine the crystallographic directions of MoS₂ by crack propagation. The freely rotatable sample holder (Figure 26 (a)) was subsequently deployed to turn the substrate in alignment with the scratch directions. The result shows a nano-patterned surface

with scratches following the zigzag direction of MoS₂, although a misalignment of 7° to the crystal orientation occurred. The spill-out of the scratches is dramatically reduced compared to similar experiments with same forces and velocities at arbitrary angles. Close-up images the area surrounding the trenches exhibit agglomerates with sizes of around 25 nm created by the rupture. However, the typical nanoexfoliation covering multiple μm² and crack propagation away from the scratch are not present, leaving the rest of the surface relatively clean and flat for later modification. Although this method can provide a solution to the creation of large folds and run-away cracks, the user is restricted to the crystallographic features provided by the material used for modification. In case of MoS₂ this gives two possible scratch directions, with the zigzag direction being the most applicable one.

7.3 Au Island Manipulation on Patterned MoS₂

The results in the previous sections discussing the mechanics of MoS₂ rupturing and the accompanying phenomena suggest that CVD grown monolayer substrate appears to be the better option for scratch-based surface modification. Bulk material does provide an option for relatively clean scratches but is restricted to armchair- and zigzag directions of the surface for patterning. However, agglomerates of 50 nm in heights can still occur, while monolayer flakes of MoS₂ perform much more forgiving to less preferred crack propagation directions. Here, the spill-out of nonconform scratches remains under 20 nm of height and nanoexfoliation folds tend to lie flat on the monolayer. This makes it an acceptable substrate for surface modification with the intend to aid in the formation of Au island-based nanowires.

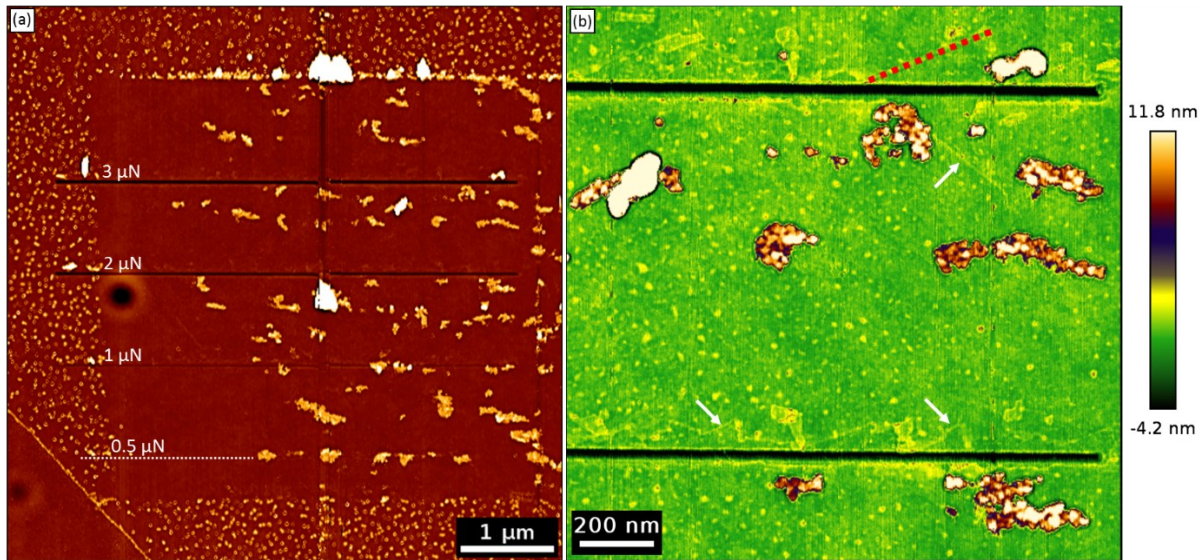


Figure 41: Result of Au island manipulation on a scratched MoS₂ monolayer. (a) Topography image at a scan angle of 90° showing the result of the manipulation of a 4.5 x 4.5 μm area with a setpoint of 50 nN and activated hover mode. Nanoscratches were performed from left to right at an angle of 45° to the edge of the monolayer MoS₂ substrate with varying normal forces F_N between 0.5 μN and 3 μN. The white dotted line indicates the scratch line of 0.5 μN which did not penetrate the monolayer. (b) False-colored close-up of the nanoparticle agglomeration around the 2 and 3 μN scratch line. Nanoexfoliations (thin yellow triangular shapes) alongside of the scratches following the zigzag direction of MoS₂ at an angle of 22° upwards or at 38° developing downwards from the scratch (red dotted line, white arrows as indicators). Au island have not been deposited in the trench but rather became immobile when encountering a MoS₂ fold or spilled-out material.

The tapping mode image above shows an example of the manipulation behavior of Au islands when encountering nanoscratches of different normal forces F_N . The surface modification was achieved with a D300 diamond tip scratching from left to right with a velocity v of 1 μm/s. With increasing normal force, a deeper and wider trench is created by the tip apex pulverizing the underlying SiO₂ of the wafer. As reported by Özoğul et al. [99] a normal load under 1 μN does not break the monolayer which can be seen in Figure 41 (a) for the scratch with $F_N = 0.5$ μN with the dotted white line indicating the scratch position. The remaining scratches exhibit typical features of nanoexfoliation and subsequent folding of the monolayer and wrinkle formation.

After surface patterning the same tip was used to manipulate the nanoparticles in contact mode and activated hover mode of 50 nm, scanning with a normal force F_N of 50 nN and line spacing of 9 nm. The Au islands were displaced at an angle θ of 41°, following the zigzag direction that also dominates the visible crack propagation. Contrary to the assumption that nano islands would get stuck in the trench when being manipulated across nanoscratches, the

experiment provides the opposite scenario. Even though the scratch with a force of 0.5 nN did not rupture the monolayer, it influenced the surface structure enough to provide a viable obstacle for displaced Au islands. Interestingly lower force scratches show a greater accumulation of nanoparticles directly on the line, while forces of F_N of 2 μN and above have no nano island deposition inside the trench lines. This might be caused by the tip damaging the rigid SiO_2 underneath the monolayer while MoS_2 reacts elastically to the normal force extruded. The 40 to 50 nm wide trenches cut by the diamond tip show a depth of 4 to 6 nm with a force of 2 or 3 μN respectively. Characteristic nanoexfoliation caused by the plowing of the tip is also present, typically located on the upper border of the scratch but also visible on the opposite side, as can be seen in Figure 41 (b) below the red dotted line. This area gives an insight in the mechanics of Au island displacement. While manipulated nanoparticles have been observed climbing over the step edge onto a bilayer of MoS_2 (see Figure 36) while maintaining the directionally locked trajectory, a second layer created by exfoliation and subsequent fold-over appears to provide an impassable obstacle which leads to accumulation of displaced Au islands along the fold. The height difference between the monolayer and the exfoliated flake deposited on top of it is around 0.6 nm with little change in the fold's topography, suggesting an atomically smooth interface between the substrate and the flake. But also borders of nanoscratches without exfoliation show features of 0.5 to 1 nm in height (indicated by white arrows in Figure 41 (b)) from the destructive plowing of the diamond tip. These ridges form a crest on both sides of the nanoscratch where no nanoexfoliation occurred which indicates a frayed edge of the monolayer due to ripping of the material. Au islands also form agglomerates with a distance of 10 to 12 nm from the ridge crest when pushed towards a trench, as can be seen for the nanoscratches with 2 and 3 μN of force. However, lateral deflection images of the manipulation scan show displacement pathways traversing over the nanoscratches and their ridges and exfoliations. In the areas between the surface modifications standard striation formation parallel to the fast axis of the manipulation scan takes place, as discussed in chapter 5.3. Due to the disruption of directional locking and a clean pathway usually provided by the highly ordered surface of MoS_2 , bands of Au islands appear to be much less organized, with a shorter stripe length of under 1 μm , a greater agglomeration instead of thin lines of islands and varying height distribution, suggesting an actual pile-up of particles instead of gold triangles keeping distance and epitaxial orientation when becoming immobile.

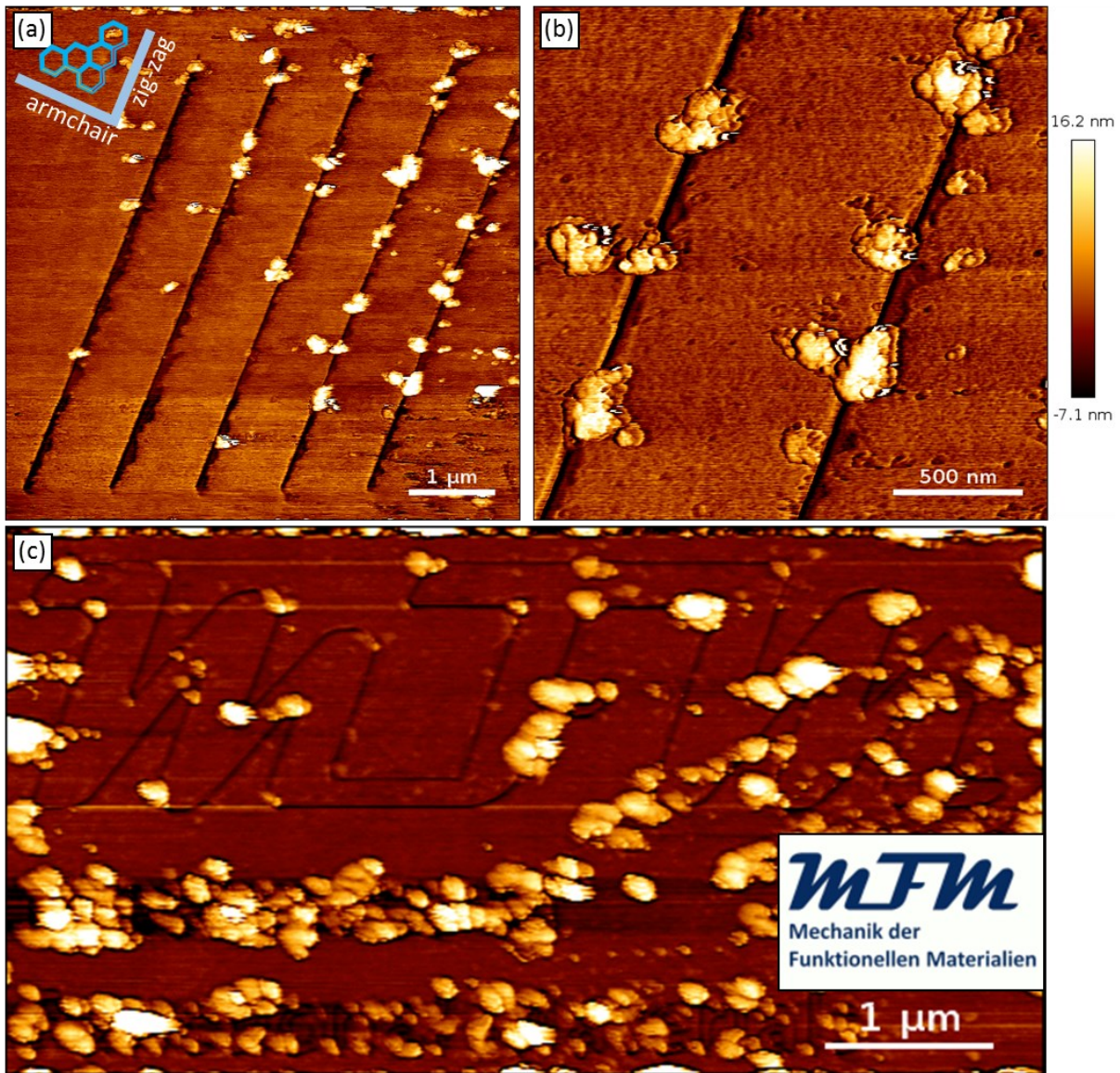


Figure 42: (a) Topography tapping mode image after the nanomanipulation of Au islands with a normal load $F_N = 50$ nN on a scratch-patterned surface ($F_N = 2$ μ N) along zigzag direction of the monolayer MoS_2 substrate. (b) Topography close-up of two trenches with embedded agglomerations of nanoparticles showing minimal signs of exfoliation or wrinkles. (c) Au islands displaced with a normal load of $F_N = 50$ nN over the scratched-in logo (“mFm”, normal force $F_N = 2$ μ N) of a well-known nanotribology work group. This experiment was conducted at the same orientation on the same 50 μ m MoS_2 flake as (a) and (b).

Another picture is painted when nanoscratches are applied in alignment with the crystallographic directions of the substrate using a D300 single crystal diamond tip. Figure 42 (a) and the close-up (b) present an exemplary case of five nanoscratches (left three downwards, right two upwards) with a normal force of $F_N = 2$ μ N at 1 μ m/s to create trenches around 6 nm deep and 40 nm wide at an angle of 67° with respect to the fast axis. All scratch ridges display minimal signs of nanoexfoliation with significantly less surface damage

compared to scratches along arbitrary angles. After patterning the surface, nanomanipulation was performed in contact mode with a normal load of $F_N = 50$ nN and activated hover mode, using the same D300 tip. Au islands were manipulated in a directionally locked manner following either two zigzag directions (parallel to scratches at 67° and at 7°) or the armchair direction with 37° in relation to the fast axis. In contrast to the case of arbitrarily angled scratches discussed in the previous chapter, Au islands agglomerate mostly inside the trenches in irregular dense shapes with height distributions suggesting a pile-up with particles sitting on top of each other in direct contact, as can be seen in the close-up topography image in Figure 42 (b). Displacement pathways of islands in lateral deflection images of manipulation scans also show islands traversing the scratched-in trenches in armchair direction. It is noteworthy that no Au island striation occurs in the area between the scratches compared to the experiments regarding Figure 41 with the same scratch spacing of $1 \mu\text{m}$, keeping the surface clean for later modifications.

The last chapters alluded to a complex interplay of phenomenon influencing the outcome of manipulation experiments in combination with scratch-based surface modification. However, future applications will require much more difficult and irregular structures than straight lines of scratches. A dominant feature will be intersecting nanowires in addition to corners and curves to utilize the full potential of nano electronics. To test out the modification and manipulation behavior the logo of the work group of Mechanics of functional Materials (mFm) was chosen, presenting a set of different feature from straight lines in different angles to corners, curves and a sub headline with 500nm tall letters. The manipulation was conducted with the same D300 tip as used for the nanoscratching, with $F_N = 50$ nN of normal force with hovering retrace of 50 nm and line spacing of 12 nm at a velocity v of $1 \mu\text{m/s}$. Clearly visible in Figure 42 (c), areas where nanoscratches meet to form a corner appear to have a high possibility to immobilize displaced Au island during manipulation. With almost all corners of the scratched letters occupied these locations can be seen as a nucleation point for subsequent pile-up of more arriving nanoparticles. While corners present a sharp change of the trench direction curves present a more gradual transition with a wider radius. However, Au islands manipulated over these features still tend to stop when encountering the curved nanoscratch. Accumulations of particles in said features display heights of 20 to 25 nm, suggesting a stacking mechanism of the gold crystals. The biggest agglomeration of gold particles is evidently on top of the scratched-in sub headline of the logo, with letters of the

size of 300 to 500 nm and individual features like curves and corners down to 20 nm in size. The feature density of these letters is very high, providing corners and curves ever few nanometers as obstacles for traversing Au islands, which increases the probability of immobilization considerably. Once an island is stopped by the surface disruption underneath it can act as a nucleus for further particle agglomeration due to the electrostatic repulsion mentioned in chapter 6.3. Accumulated particles display a height of 25 nm on average with an island height of ~ 6 nm, leading to the assumption that particles start to stack on top of each other at these locations. These results suggest not only a big influence of the orientation of nanoscratches in regard to the crystal lattice of the substrate on the immobilization of manipulated gold islands, but also the size and complexity of the patterns play a role in the amount and location of particle agglomerations.

8 Discussion

This work presents an insight into the use of CVD grown gold nanoclusters with sizes in the tens of nanometers on the metal dichalcogenide MoS_2 for the formation of nano structures via nanomanipulation with the AFM. With the attempt to provide another option for the creation of gold nanowires, this technique avoids well-known obstacles of other methods like mask-patterned deposition of gold where the sample is exposed to different chemical agents, leaving residues of said chemicals on the surface. Also, less time intensive ways of gold nanowire deposition, like drop-casting nanowires from a solution, present unintended problems by covering the sample with unorganized nanowires prone to cold welding when in contact.

But this approach also comes with its own inherent difficulties. Firstly, the material for surface functionalization must be considered. Molybdenum Disulfide provides an excellent base for later manipulation. With its many properties from multilayer crystallinity to optoelectronic effects, MoS_2 peaked interest in the nanotechnology research community in the last couple of years. Naturally and lab-grown monocrystals are atomically flat surfaces with a highly ordered pattern of atoms due to the six-fold symmetry of the hexagonal crystal lattice. With a mismatch of $\sim 8\%$ gold atoms can use the lattice as a pattern to crystallize into well-shaped

truncated triangles in epitaxial orientation without a high degree of size variation. The mismatch between both crystal structures also leads to very low forces in the range of F_N 2 to 20 nN needed to detach grown gold nanoparticles. Interestingly, different temperatures of gold deposition and annealing had less of an influence on the gold cluster growth as the MoS₂ itself. The number of layers plays an important role in the mobility of gold during the annealing process, possibly caused by permanent dipoles. CVD grown monolayer MoS₂ presents a similar picture to bulk material. However, the growth process can influence the crystal shape by element availability during the procedure which leads to different MoS₂ crystal shapes with concave crystal edges. Additionally, the growth of Au islands onto the monolayered material revealed a border effect with an average decrease in particle size while at the same time the increase in particle density suggests less mobility for the uniformly distributed gold atoms during annealing when positioned close to the MoS₂ crystal edge.

Besides the aforementioned factors on gold nanoparticle growth, the very even distribution of Au islands on the MoS₂ surface and the polarity of the triangle orientation made it possible to perform broad manipulation patterns with hundreds of individual island displacements at once for statistical analysis. Combined with the rotatable sample stage, a directional locking phenomenon was discovered which controls the direction of displacement when manipulated with contact mode or tapping mode. The geometry of the pyramidal tip did not have any influence on this effect, since conical tips revealed the same locking effect. Molecular Dynamics simulations provide some insight in the energetic mechanisms of the nanomanipulation by reproducing the displacement of a triangular, truncated gold island over a Potential Energy Surface mimicking MoS₂ in its atomic structure. The result confirms a locking effect of the displacement direction in armchair- and zigzag direction caused by the corrugated surface of Sulfur and Molybdenum placed in a hexagonal lattice. Simulations also show a “wobble” effect of the island when traversing epitaxially over the incommensurate surface, changing the island orientation by up to 0.5° and snapping back into original orientation every 3 Å, fitting the lattice parameters of the MoS₂ surface.

In contrast to bulk MoS₂, Au islands manipulated on monolayers formed striations of bands of agglomerated nanoparticles tens of μm long. This might be caused by the nanoroughness of the Si/SiO₂ wafer underneath the grown MoS₂ monolayer which effects on the smoothness of the single layer can be observed in the cross-section TEM images in chapter 5.3. The

nanoroughness of the wafer mimicked by the monolayer might provide enough surface alteration to act as an obstacle in certain locations, causing particles to stop and therefore creating another obstacle for the next Au island. At first look this seemed promising for the formation of a nanowires but unfortunately the high crystallinity of the Au islands and the spacing between accumulated nanoparticles potentially caused by electrostatic repulsion prevented most of the stripe of Au islands to melt together into a single unbroken nanowire. The re-annealing process with a maximum temperature of 700°C did fuse gold islands of less well-shaped irregular quality, suggesting a less stable crystal structure, yet the vast majority of Au islands are well crystallized and therefore energetically more stable. This energy barrier couldn't be overcome in the reheating experiment. Even though a nanowire with the length of 150 nm was created, the electrostatic repulsion hindering gold islands from getting in direct contact with each other also prohibits the formation of a single nanowire from the striation of Au islands left after nanomanipulation.

The modification of the MoS₂ surface using a single crystal diamond glued to the cantilever might provide an option to create manmade locations and patterns for particles to stop and agglomerate when manipulated en masse by a scan pattern. Nanoscratches need a normal force F_N of at least 1 μN to break the surface layer of the material. Here, the crystal lattice orientation plays a big role again, considering the rupture mechanics of the hexagonal material tearing apart preferentially along armchair- or zigzag direction. The difference between scratch direction and crystal orientation of MoS₂ determines the amount of damage done to the areas surrounding the created trench, ranging from very clean scratches to chipping and nanoexfoliation creating pileups in the hundreds of nanometers in height. However, this also provides a quick tool to determine the crystal orientation of bulk MoS₂ by scratching the surface to cause nanoexfoliation which inherently follows the crystal orientation of the folded material. On monolayer material similar effects of nanoexfoliation can be seen, although the damage to the surrounding area is much less severe with folds as flat as 1 nm. When manipulating gold particles over a scratched monolayer the direction of the trenches to the crystal orientation must be considered, with aligned scratches not only collecting agglomerates of Au islands much better but also preventing the formations of bands of gold particles in between the nanoscratches. Interestingly, even though a nanoscratch performed with a force lower than 0.5 μN did not break through the monolayer, nanoparticles still accumulated along the scratch line, suggesting a, alteration of the SiO₂ surface with the

monolayer of MoS₂ on top reacting elastically to the diamond tip. Agglomeration of particles inside the trenches show stacked Au islands in random orientations in direct contact with each other. This might solve the problem of electrostatic repulsion, bringing the gold crystals close enough together for re-annealing or cold welding. But not only orientation of the modification pattern is important. Scratched curves and corners have been proven to act as stopping points, as can be seen in the scratched logo. The sub headline completely covered in gold islands leads to the assumption that very small surface features consisting of many different directions and corners provide an excellent surface disruption to intentionally immobilize Au islands when the interface of Au island and the underlying MoS₂ surface is interrupted in multiple directions in the area covered by the gold crystal.

9 Conclusion and Outlook

The nanomanipulation of grown particles on crystalline surfaces is strongly influenced by the interacting crystal systems and their lattice directions. This, in combination with the electrostatic repulsion between gold islands, complicates the arrangement of Au islands into desired shapes and patterns. Additionally, the on monolayer MoS₂ forming striation pattern prohibits long distance displacement of particles. However, these obstacles can be diminished by modifying the MoS₂ surface via nanoscratches to provide a manmade stopping point for manipulated particles. Here again, one must consider not only the thickness of material but also the crystallographic directions the patterns are applied to. Monolayer MoS₂ might exhibit nanoexfoliation but due to just a single layer being ruptured the surface damage surrounding the scratch is much more manageable for later nanomanipulation experiments. Especially nanoscratch features in the tens of nanometers with high directional variation have been found to be very effective immobilization locations of traversing Au islands, stacking particles on top of each other in direct contact at the intended location.

Further research is needed to establish a method to reliably create long agglomerations of gold islands in the correct geometry and position. Conductive AFM measurements can be useful to determine if direct contact of Au islands will lead to cold welding as shown by Moreno-Moreno et al. [62] when connecting gold nanowires using AFM manipulation or

whether re-annealing is necessary to fuse the particles together into a single nanowire. With the help of numerical simulations and machine learning techniques surface modification and manipulation patterns could be useful to determine the right manipulation sequences outside of the standard raster scan pattern used by modern AFMs. Also, the phenomenon of directionally locked nanoexfoliation might provide another tool to remove specific areas of the monolayer MoS₂ for even more complex nanostructure compositions. Fractal scratch designs might hold the key to the full control of Au island deposition in the right thickness and density for the creation of complex gold nanostructures that can be utilized in the field of nanoelectronics.

List of Figures

Figure 1: Egyptians pulling a statue on a wooden sled.....	3
Figure 2: A sketch by Leonardo Da Vinci illustrating the relationship between contact area and normal load	4
Figure 3: Prandtl-Tomlinson model.....	7
Figure 4: (a) modern cantilever with tip under the SEM (b) used pyramidal tip (c) close-up of a used tip with a diameter of 553 nm.....	11
Figure 5 (a) Basic working principle of the AFM used in this work. (b) normal bending experienced by the cantilever in correlation to the normal force F_N . In tapping mode the bending is induced through excitement to oscillations. (c) torsional bending of the cantilever proportional to the lateral force F_L recorded by the PSD as lateral deflection left (L) to right (R)	13
Figure 6: JPK NanoWizard 4 standing on its table-top vibration isolation system, all housed in an insulated soundproof chamber.....	15
Figure 7: A sketch of a typical force-distance curve (hysteresis).....	19
Figure 8: Lennard-Jones potential shows the interaction between long range van-der-Waals forces attracting the tip to the surface with $d > 2 \text{ \AA}$ and short range Pauli-repulsion repelling the tip due to overlapping electron orbitals with $d < 2 \text{ \AA}$	20
Figure 9: QI mode manipulation image of Au islands into an already cleaned area (dotted square). (b) corresponding adhesion map of the manipulation reveals the trajectories of displaced particles with a high contrast between the low adhesion gold islands and the MoS ₂ substrate.....	28
Figure 10: (a) lateral deflection image with a size of 5x5 nm of contact mode measurements using ContALG with visible thermal drift (b) trace (red) and retrace (blue) profile of the lateral signal on the same scan line show the typical hacksaw tooth pattern for stick-slip events. (c) 2D autocorrelation map highlighting atomic position of the MoS ₂ surface (d) Fast-Fourier-Transformation (FFT) transforming X-Y representation of the signal into polar representation highlighting the periodicity and angle of the lateral signal data (e) Profile of the 2D autocorrelation map	30
Figure 11: (a) optical microscope image of grown MoS ₂ on SiO ₂ /Si substrates showing a high density of randomly oriented and sometimes intergrown triangular monolayers. (b) Raman spectrum measured on a crystal of MoS ₂	33
Figure 12: (a) height image of different monolayer MoS ₂ crystals in random orientations, partially grown together. (b) example of a MoS ₂ triangle with developed second layer grown from the center (c) schematic growth model showing the preferential growth directions (faces) developing the monolayer from a hexagonal structure to a triangle.....	34
Figure 13: (a) MoS ₂ sample mounted on the Molybdenum plate for gold deposition. (b) SEM backscattered electron image.....	35
Figure 14: (a) SEM, (b) AFM tapping mode, and (c) STM images of different areas of the Au/MoS ₂ sample in regions chosen for manipulation experiments. (d), (e) Atomic resolution of an Au island and the MoS ₂ substrate.....	37

Figure 15: (a) The strain of Au atoms and MoS ₂ in {111} respectively (b) Schematic model of atomic mismatch of the epitaxial growth of gold on MoS ₂	38
Figure 16: Au - MoS ₂ system showing compression of the substrate lattice underneath the grown Au crystal, while the immediate area around the island experiences stretching in its lattice	38
Figure 17: Dark field cross section achieved with HAADF-STEM of the monolayer MoS ₂ system	39
Figure 18: SEM image of monolayer MoS ₂ triangles after Au deposition	40
Figure 19: (a) SEM image of a smaller MoS ₂ triangle with a size of ~5 μm and CVD grown Au islands on top. (b) close-up of gold nanoparticles showing well-ordered orientation due to the epitaxial growth. (c) SEM image of another MoS ₂ crystal with a second layer in its center ...	41
Figure 20: (a) Cross section HAADF-STEM image of a single Au island with visible crystalline atomic structure sitting on top of a monolayer of MoS ₂ grown on a Si/SiO ₂ wafer. (b) Close-up of the monolayer consisting of two bands of Sulfur atoms (green) with Molybdenum in between. (c) In-plane distance between S atoms.....	42
Figure 21: (a) High resolution HAADF-STEM image showing Au atoms well-structured in the crystal lattice of a gold island, sitting on top of a monolayer of MoS ₂ . (b) Intensity profile of the electron probe showing the atomic positions of Au, S and Mo.	43
Figure 22: (a) Tapping mode topography image of a manipulation sequence at 60° sample rotation (b) vertical deflection image of the same sequence.....	45
Figure 23: Nanomanipulation sequence in tapping mode with (a) 2x2 μm image to record the initial positions of Au islands (b) Tapping mode manipulation image with a rel. set point of 8% and hover mode (c) Overview of the manipulated area recording displacement positions...	45
Figure 24: Combination of the sequence from Fig. 23.....	46
Figure 25: (a) Lock-in Phase image during manipulation 500 x 500 nm (b) Normalized power dissipation of the profile 1 (see (a)) showing power dissipated to the particle with respect to the substrate (c) Normalized power dissipation of profile 2 (see (a)).	47
Figure 26: (a) Rotatable sample holder with mounted MoS ₂ sample (b) Schematics of the manipulation experiment.....	48
Figure 27: Manipulation images arranged with respect to the crystallographic orientation and the dominating displacement directions	49
Figure 28: Preferential sliding direction of Au islands in tapping mode manipulation experiments as a function of the scan direction.....	50
Figure 29: SEM images of the tips before and after manipulation of Au islands	51
Figure 30: Preferential sliding direction of Au islands in tapping mode manipulation experiments using conical tips as a function of the scan direction	52
Figure 31: (a) Energy map of the Au-island contact face showing the solitonic pattern (b) Sketch of a simulated repulsive cylinder (gray), mimicking the tip, pushing the island laterally as in experimental conditions. (c) A simulated PES map reporting the total potential energy. (d) A sketch of the MoS ₂ surface	53
Figure 32: (a) Simulation of pathways of the island COM on the computed PES map of the MoS ₂ surface (b) Island orientation β as a function of the COM distance from the starting point during manipulation reported in panel (a). (c) Red dots represent a function of the island orientation angle β on MoS ₂ , the simulated total energy E _{tot} including Au-Au and Au-MoS ₂	

interaction energies. Blue squares represent the sole Au-MoS ₂ interaction energy contribution E_{int} .	55
Figure 33: Force traces obtained for the simulated island	56
Figure 34: Typical manipulation sequence for the monolayer-MoS ₂ -Au-system (a) height image in tapping mode showing the initial positions of all Au islands (b) Lateral deflection image of the manipulation in contact mode (c) Tapping mode image after manipulation showing the formation of regular bands of Au islands.	58
Figure 35: Manipulation on monolayer and bilayer MoS ₂ . (a) Topography image of the contact mode manipulation. (b) Tapping mode image of the manipulation result. (c) SEM BSED image of the manipulated area.	59
Figure 36: SEM images of the second layer of MoS ₂ showing results of the manipulation sequence with the upper left corner showing the topographies of the AFM manipulation. (a) Au islands on the second layer are grown in relatively high density which inhibits far displacement and the formation of nanoparticle bends. (b) Manipulation on another MoS ₂ triangle.	61
Figure 37: SEM images of the fusion experiment after manipulation (a) A band of Au islands on monolayer MoS ₂ before reheating (b) After reheating in the UHV chamber (c) Result of reheating the same area to a temperature of 700°C. (d) Close-up of the area.	63
Figure 38: Radial nanoscratches with a single-crystal diamond tip. (a) Vertical Deflection image of a half circle of scratch profiles (b) Topography image of a full circle (every 10°) of nanoscratches on monolayer MoS ₂	65
Figure 39: A set of 6 parallel scratches on the monolayer MoS ₂ substrate. (a) Topography image with a scan angle of 90° (b) The phase image highlights the different materials.	67
Figure 40: Nano pattern along the zigzag direction of the bulk MoS ₂ substrate (b) The amplitude tapping mode image of the same region (c) Amplitude close-up image.	68
Figure 41: Result of Au island manipulation on a scratched MoS ₂ monolayer. (a) Topography image at a scan angle of 90° showing the result of the manipulation (b) False-colored close-up of the nanoparticle agglomeration.	70
Figure 42: (a) Topography tapping mode image after the nanomanipulation of Au islands along zigzag direction of the monolayer MoS ₂ substrate. (b) Topography close-up of two trenches with embedded agglomerations of nanoparticles. (c) Au islands displaced over the scratched-in logo	72

List of Tables

Table 1: Used cantilevers and their characteristics	18
Table 2: Gold deposition conditions and properties of grown Au islands.....	36

Bibliography

- [1] CADORET, GENEVIÈVE ; SMITH, ALLAN M.: Friction, not texture, dictates grip forces used during object manipulation. In: *Journal of Neurophysiology* Bd. 75, American Physiological Society (1996), Nr. 5, S. 1963–1969
- [2] HAN, HYUN YONG ; SHIMADA, AKIHIRO ; KAWAMURA, SADA0: Analysis of friction on human fingers and design of artificial fingers. In: *Proceedings - IEEE International Conference on Robotics and Automation*. Bd. 4 : IEEE, 1996, S. 3061–3066
- [3] CHATTERJEE, SUDIPTA: *Tribological properties of pseudo-elastic nickel-titanium*, 2008 — ISBN 9780549844372
- [4] FISHBANE, PAUL M.; GASIOROWICZ, STEPHEN; THORNTON, STEPHEN T.: *Physics for Scientists and Engineers*. extended e. : Pearson Prentice Hall, 1993 — ISBN 978-0-13-663246-7
- [5] NEWBERRY, PERCY E.: *El Bersheh (Band 1): The tomb of Tehuti-Hetep*, 1894
- [6] LIEFFERINK, R. W. ; WEBER, B. ; BONN, D.: Ploughing friction on wet and dry sand. In: *Physical Review E* Bd. 98, American Physical Society (2018), Nr. 5, S. 052903
- [7] HUTCHINGS, IAN M.: Leonardo da Vinci's studies of friction. In: *Wear* Bd. 360–361, Elsevier Ltd (2016), S. 51–66
- [8] DOWSON, DUNCAN: *History of Tribology* : John Wiley & Sons, 1998 — ISBN 186058070X
- [9] AMONTONS, G.: *“De la resistance caus”ee dans les machines* : Mémoires de l'Académie Royale, A, Chez Gerard Kuyper, 1699
- [10] URBAKH, MICHAEL ; KLAFTER, JOSEPH ; GOURDON, DELPHINE ; ISRAELACHVILL, JACOB: The nonlinear nature of friction. In: *Nature* Bd. 430, Nature Publishing Group (2004), Nr. 6999
- [11] HOLMBERG, KENNETH ; SIILASTO, ROOPE ; LAITINEN, TARJA ; ANDERSSON, PETER ; JÄSBERG, ARI: Global energy consumption due to friction in paper machines. In: *Tribology International* Bd. 62, Elsevier (2013), S. 58–77
- [12] HOLMBERG, KENNETH ; ERDEMIR, ALI: Influence of tribology on global energy consumption, costs and emissions. In: *Friction* Bd. 5 (2017), Nr. 3, S. 263–284
- [13] RAI-CHOUHDURY: *Handbook of Microlithography, Micromachining, and Microfabrication. Volume 1: Microlithography* : Spie Press Book, 1997 — ISBN 9780819497864
- [14] NOVOSELOV, K. S. ; GEIM, A. K. ; MOROZOV, S. V. ; JIANG, D. ; ZHANG, Y. ; DUBONOS, S. V. ; GRIGORIEVA, I. V. ; FIRSOV, A. A.: Electric field in atomically thin carbon films. In: *Science* Bd. 306, Science (2004), Nr. 5696, S. 666–669

- [15] TANS, SANDER J. ; VERSCHUEREN, ALWIN R.M. ; DEKKER, CEES: Room-temperature transistor based on a single carbon nanotube. In: *Nature* Bd. 393, Nature Publishing Group (1998), Nr. 6680, S. 49–52
- [16] HATZAKIS, M.: Electron Resists for Microcircuit and Mask Production. In: *Journal of The Electrochemical Society* Bd. 116, The Electrochemical Society (1969), Nr. 7, S. 1033
- [17] POPOV, V.L. ; GRAY, J.A.T.: Prandtl-Tomlinson model: History and applications in friction, plasticity, and nanotechnologies. In: *ZAMM - Journal of Applied Mathematics and Mechanics / Zeitschrift für Angewandte Mathematik und Mechanik* Bd. 92, John Wiley & Sons, Ltd (2012), Nr. 9, S. 683–708
- [18] SOCOLIUC, A. ; BENNEWITZ, R. ; GNECCO, E. ; MEYER, E.: Transition from stick-slip to continuous sliding in atomic friction: Entering a new regime of ultralow friction. In: *Physical Review Letters* Bd. 92, American Physical Society (2004), Nr. 13, S. 134301
- [19] MATE, C. MATHEW ; MCCLELLAND, GARY M. ; ERLANDSSON, RAGNAR ; CHIANG, SHIRLEY: Atomic-Scale Friction of a Tungsten Tip on a Graphite Surface. In: *Physical Review Letters* Bd. 59, Springer, Dordrecht (1987), S. 226–229
- [20] BOWDEN, F. P. ; LEBEN, L.: Nature of sliding and the analysis of friction [12]. In: *Nature* Bd. 141, Chemical Publishing Co (1938), Nr. 3572
- [21] SCHOLZ, C. H.: Earthquakes and friction laws. In: *Nature* Bd. 391, Nature Publishing Group (1998), Nr. 6662
- [22] GNECCO, ENRICO ; FAJARDO, OSCAR Y. ; PINA, CARLOS M. ; MAZO, JUAN J.: Anisotropy effects in atomic-scale friction. In: *Tribology Letters* Bd. 48, Springer (2012), Nr. 1, S. 33–39
- [23] ROTH, RAPHAEL ; GLATZEL, THILO ; STEINER, PASCAL ; GNECCO, ENRICO ; BARATOFF, ALEXIS ; MEYER, ERNST: Multiple slips in atomic-scale friction: An indicator for the lateral contact damping. In: *Tribology Letters*. Bd. 39 : Springer, 2010, S. 63–69
- [24] PERSSON, BO: *Sliding Friction - Physical Principles and Applications* : Springer-Verlag, 2000 — ISBN 978-3-540-67192-3
- [25] F. P. BOWDEN, FRANK PHILIP BOWDEN, DAVID TABOR: *The Friction and Lubrication of Solids*, 1950 — ISBN 9780198507772
- [26] MO, YIFEI ; SZLUFARSKA, IZABELA: Roughness picture of friction in dry nanoscale contacts. In: *Physical Review B - Condensed Matter and Materials Physics* Bd. 81, American Physical Society (2010), Nr. 3, S. 035405
- [27] GOTSMANN, B. ; LANTZ, M. A.: Quantized thermal transport across contacts of rough surfaces. In: *Nature Materials* Bd. 12 (2013), Nr. 1, S. 59–65
- [28] LIU, YUN ; SZLUFARSKA, IZABELA: Chemical origins of frictional aging. In: *Physical Review Letters* Bd. 109, American Physical Society (2012), Nr. 18, S. 186102
- [29] BAUMBERGER, TRISTAN ; CAROLI, CHRISTIANE: Solid friction from stick–slip down to pinning and aging. In: *Advances in Physics* Bd. 55, Taylor & Francis Group (2006), Nr. 3–4, S. 279–348
- [30] GREENWOOD, J. A. ; WILLIAMSON J. B. P.: Contact of nominally flat surfaces. In: *Proceedings of the Royal Society of London. Series A. Mathematical and Physical Sciences* Bd. 295,

The Royal Society (1966), Nr. 1442, S. 300–319

- [31] POPOV, VALENTIN L.: *Contact mechanics and friction: Physical principles and applications* : Springer Berlin Heidelberg, 2010 — ISBN 9783642108020
- [32] RITTER, CLAUDIA ; HEYDE, MARKUS ; STEGEMANN, BERT ; RADEMANN, KLAUS ; SCHWARZ, UDO D.: Contact-area dependence of frictional forces: Moving adsorbed antimony nanoparticles. In: *Physical Review B - Condensed Matter and Materials Physics* Bd. 71, American Physical Society (2005), Nr. 8, S. 085405
- [33] MO, YIFEI ; TURNER, KEVIN T. ; SZLUFARSKA, IZABELA: Friction laws at the nanoscale. In: *Nature* Bd. 457, Nature Publishing Group (2009), Nr. 7233, S. 1116–1119
- [34] LI, AO ; LIU, YUN ; SZLUFARSKA, IZABELA: Effects of interfacial bonding on friction and wear at silica/silica interfaces. In: *Tribology Letters* Bd. 56, Springer New York LLC (2014), Nr. 3, S. 481–490
- [35] RIEDO, ELISA ; LÉVY, FRANCIS ; BRUNE, HARALD: Kinetics of capillary condensation in nanoscopic sliding friction. In: *Physical Review Letters* Bd. 88, American Institute of Physics Inc. (2002), Nr. 18, S. 1855051–1855054
- [36] GANSER, CHRISTIAN ; CZIBULA, CATERINA ; TSCHARNUTER, DANIEL ; SCHÖBERL, THOMAS ; TEICHERT, CHRISTIAN ; HIRN, ULRICH: Combining adhesive contact mechanics with a viscoelastic material model to probe local material properties by AFM. In: *Soft Matter* Bd. 14, Royal Society of Chemistry (2017), Nr. 1, S. 140–150
- [37] RUINA, A.: Slip instability and state variable friction laws. In: *Journal of Geophysical Research* Bd. 88, John Wiley & Sons, Ltd (1983), Nr. B12, S. 10359–10370
- [38] BAUMBERGER, T. ; BERTHOUD, P. ; CAROLI, C.: Physical analysis of the state- and rate-dependent friction law. II. Dynamic friction. In: *Physical Review B - Condensed Matter and Materials Physics* Bd. 60, American Physical Society (1999), Nr. 6, S. 3928–3939
- [39] LI, QUNYANG ; TULLIS, TERRY E. ; GOLDSBY, DAVID ; CARPICK, ROBERT W.: Frictional ageing from interfacial bonding and the origins of rate and state friction. In: *Nature* Bd. 480, Nature (2011), Nr. 7376, S. 233–236
- [40] VORHOLZER, MATTHIAS ; VILHENA, J. G. ; PEREZ, RUBEN ; GNECCO, ENRICO ; DIETZEL, DIRK ; SCHIRMEISEN, ANDRÉ: Temperature Activates Contact Aging in Silica Nanocontacts. In: *Physical Review X* Bd. 9 (2019), Nr. 4, S. 1–10
- [41] ISRAELACHVILI, J. ; MIN, Y. ; AKBULUT, M. ; ALIG, A. ; CARVER, G. ; GREENE, W. ; KRISTIANSEN, K. ; MEYER, E. ; U. A.: Recent advances in the surface forces apparatus (SFA) technique. In: *Reports on Progress in Physics* Bd. 73 (2010), Nr. 3
- [42] BINNING, G. ; ROHRER, H. ; GERBER, CH ; WEIBEL, E.: Surface studies by scanning tunneling microscopy. In: *Physical Review Letters* Bd. 49, Springer-Ver-lag (1982), Nr. 1, S. 57–61
- [43] BINNIG, G. ; QUATE, C. F. ; GERBER, CH: Atomic force microscope. In: *Physical Review Letters* Bd. 56, American Physical Society (1986), Nr. 9, S. 930–933
- [44] SECRETDISC: *SEM images of AFM tips*.
- [45] HÖLSCHER, H. ; SCHWARZ, U. ; ZWÖRNER, O. ; WIESENDANGER, R.: Consequences of the stick-slip movement for the scanning force microscopy imaging of graphite. In: *Physical*

- Review B - Condensed Matter and Materials Physics* Bd. 57, American Physical Society (1998), Nr. 4, S. 2477–2481
- [46] RUGAR, D ; MAMIN, H J ; GUETHNER, P: Improved fiber-optic interferometer for atomic force microscopy. In: *Appl. Phys. Lett* Bd. 55 (1989), S. 2588 — ISBN 10.1063/1.100061
- [47] BHUSHAN, BHARAT: *Springer Handbook of Nanotechnology*: Springer-Verlag, 2004 — ISBN 978-3-662-54357-3
- [48] SADER, JOHN E. ; LARSON, IAN ; MULVANEY, PAUL ; WHITE, LEE R.: Method for the calibration of atomic force microscope cantilevers. In: *Review of Scientific Instruments* Bd. 66, American Institute of Physics AIP (1995), Nr. 7, S. 3789–3798
- [49] ALBRECHT, T. R. ; GRÜTTER, P. ; HORNE, D. ; RUGAR, D.: Frequency modulation detection using high-Q cantilevers for enhanced force microscope sensitivity. In: *Journal of Applied Physics* Bd. 69, American Institute of Physics AIP (1991), Nr. 2, S. 668–673
- [50] GIESSIBL, F. J.: A direct method to calculate tip-sample forces from frequency shifts in frequency-modulation atomic force microscopy. In: *Applied Physics Letters* Bd. 78, American Institute of Physics AIP (2001), Nr. 1, S. 123–125
- [51] SCHWARZ, UDO D. ; ZWÖRNER, OLIVER ; KÖSTER, PETER ; WIESENDANGER, ROLAND: Quantitative analysis of the frictional properties of solid materials at low loads. I. Carbon compounds. In: *Physical Review B - Condensed Matter and Materials Physics* Bd. 56, American Physical Society (1997), Nr. 11, S. 6987–6996
- [52] ÖZOĞUL, ALPER ; GRÄF, STEPHAN ; MÜLLER, FRANK A ; GNECCO, ENRICO: Reverse Stick-Slip on a Periodic Wedge-Shaped Micrograting. In: *Tribology Letters* Bd. 67 (2019), S. 29 — ISBN 0123456789
- [53] LÜTHI, R. ; MEYER, E. ; HAEFKE, H. ; HOWALD, L. ; GUTMANN SBAUER, W. ; GÜNTHERODT, H. J.: Sled-type motion on the nanometer scale: Determination of dissipation and cohesive energies of C60. In: *Science* Bd. 266, American Association for the Advancement of Science (1994), Nr. 5193, S. 1979–1981
- [54] SHEEHAN, PAUL E. ; LIEBER, CHARLES M.: Nanotribology and nanofabrication of MoO₃ structures by atomic force microscopy. In: *Science* Bd. 272, American Association for the Advancement of Science (1996), Nr. 5265, S. 1158–1161
- [55] DIETZEL, DIRK ; MÖNNINGHOFF, TRISTAN ; JANSEN, LARS ; FUCHS, HARALD ; RITTER, CLAUDIA ; SCHWARZ, UDO D. ; SCHIRMEISEN, ANDRÉ: Interfacial friction obtained by lateral manipulation of nanoparticles using atomic force microscopy techniques. In: *Journal of Applied Physics* Bd. 102, American Institute of Physics AIP (2007), Nr. 8, S. 084306
- [56] SCHIRMEISEN, ANDRÉ ; SCHWARZ, UDO D.: Measuring the friction of nanoparticles: A new route towards a better understanding of nanoscale friction. In: *ChemPhysChem* Bd. 10, Wiley-VCH Verlag (2009), Nr. 14, S. 2373–2382
- [57] HIRANO, MOTOHISA ; SHINJO, KAZUMASA ; KANEKO, REIZO ; MURATA, YOSHITADA: *Anisotropy of Frictional Forces in Muscovite Mica*. Bd. 67, 1991
- [58] RAO, A. ; GNECCO, E. ; MARCHETTO, D. ; MOUGIN, K. ; SCHÖNENBERGER, M. ; VALERI, S. ; MEYER, E.: The analytical relations between particles and probe trajectories in atomic force microscope nanomanipulation. In: *Nanotechnology* Bd. 20 (2009), Nr. 11

- [59] MOUGIN, K. ; GNECCO, E. ; RAO, A. ; CUBERES, M. T. ; JAYARAMAN, S. ; MCFARLAND, E. W. ; HAIDARA, H. ; MEYER, E.: Manipulation of gold nanoparticles: Influence of surface chemistry, temperature, and environment (vacuum versus ambient atmosphere). In: *Langmuir* Bd. 24 (2008), Nr. 4, S. 1577–1581
- [60] NITA, PAWEŁ ; CASADO, SANTIAGO ; DIETZEL, DIRK ; SCHIRMEISEN, ANDRE ; GNECCO, ENRICO: Spinning and translational motion of Sb nanoislands manipulated on MoS₂. In: *Nanotechnology* Bd. 24 (2013), Nr. 32
- [61] PIMENTEL, CARLOS ; PINA, CARLOS M. ; GNECCO, ENRICO: Epitaxial growth of calcite crystals on dolomite and kutnahorite (104) surfaces. In: *Crystal Growth and Design* Bd. 13 (2013), Nr. 6, S. 2557–2563
- [62] MORENO-MORENO, MIRIAM ; ARES, PABLO ; MORENO, CONSUELO ; ZAMORA, FÉLIX ; GÓMEZ-NAVARRO, CRISTINA ; GÓMEZ-HERRERO, JULIO: AFM Manipulation of Gold Nanowires to Build Electrical Circuits. In: *Nano Letters* Bd. 19 (2019), Nr. 8, S. 5459–5468
- [63] LU, YANG ; HUANG, JIAN YU ; WANG, CHAO ; SUN, SHOUHENG ; LOU, JUN: Cold welding of ultrathin gold nanowires. In: *Nature Nanotechnology* Bd. 5, Nature Publishing Group (2010), Nr. 3, S. 218–224
- [64] DIETZEL, D. ; FELDMANN, M. ; HERDING, C. ; SCHWARZ, U. D. ; SCHIRMEISEN, A.: Quantifying pathways and friction of nanoparticles during controlled manipulation by contact-mode atomic force microscopy. In: *Tribology Letters*. Bd. 39 : Springer, 2010, S. 273–281
- [65] LIU, ZHIGUO ; LI, ZHUANG ; WEI, GANG ; SONG, YONGHAI ; WANG, LI ; SUN, LANLAN: Manipulation, dissection, and lithography using modified tapping mode atomic force microscope. In: *Microscopy Research and Technique* Bd. 69, John Wiley & Sons, Ltd (2006), Nr. 12, S. 998–1004
- [66] *QI™ Mode - Atomic Force Microscopy - JPK BioAFM | Bruker*. URL <https://www.jpk.com/products/atomic-force-microscopy/qi-mode>. - abgerufen am 2020-08-27
- [67] CHHOWALLA, MANISH ; SHIN, HYEON SUK ; EDA, GOKI ; LI, LAIN JONG ; LOH, KIAN PING ; ZHANG, HUA: The chemistry of two-dimensional layered transition metal dichalcogenide nanosheets. In: *Nature Chemistry* Bd. 5, Nature Publishing Group (2013), Nr. 4
- [68] XU, MINGSHENG ; LIANG, TAO ; SHI, MINMIN ; CHEN, HONGZHENG: Graphene-like two-dimensional materials. In: *Chemical Reviews* Bd. 113, American Chemical Society (2013), Nr. 5
- [69] MAK, KIN FAI ; LEE, CHANGGU ; HONE, JAMES ; SHAN, JIE ; HEINZ, TONY F.: Atomically thin MoS₂: A new direct-gap semiconductor. In: *Physical Review Letters* Bd. 105, American Physical Society (2010), Nr. 13, S. 136805
- [70] WANG, QING HUA ; KALANTAR-ZADEH, KOUROSH ; KIS, ANDRAS ; COLEMAN, JONATHAN N. ; STRANO, MICHAEL S.: Electronics and optoelectronics of two-dimensional transition metal dichalcogenides. In: *Nature Nanotechnology* Bd. 7, Nature Publishing Group (2012), Nr. 11
- [71] SAIDI, WISSAM A.: Influence of strain and metal thickness on metal-MoS₂contacts. In:

- Journal of Chemical Physics* Bd. 141, American Institute of Physics Inc. (2014), Nr. 9, S. 094707
- [72] BOKDAM, MENNO ; BROCKS, GEERT ; KATSNELSON, M. I. ; KELLY, PAUL J.: Schottky barriers at hexagonal boron nitride/metal interfaces: A first-principles study. In: *Physical Review B - Condensed Matter and Materials Physics* Bd. 90, American Physical Society (2014), Nr. 8, S. 085415
- [73] BOKDAM, MENNO ; BROCKS, GEERT ; KELLY, PAUL J.: Large potential steps at weakly interacting metal-insulator interfaces. In: *Physical Review B - Condensed Matter and Materials Physics* Bd. 90, American Physical Society (2014), Nr. 20, S. 201411
- [74] DONNET, C. ; MARTIN, J. M. ; LE MOGNE, TH ; BELIN, M.: Super-low friction of MoS₂ coatings in various environments. In: *Tribology International* Bd. 29, Elsevier Ltd (1996), Nr. 2, S. 123–128
- [75] MARTIN, J. M. ; DONNET, C. ; LE MOGNE, TH ; EPICIER, TH: Superlubricity of molybdenum disulphide. In: *Physical Review B* Bd. 48, American Physical Society (1993), Nr. 14, S. 10583–10586
- [76] MARTIN, J. M. ; PASCAL, H. ; DONNET, C. ; LE MOGNE, TH ; LOUBET, J. L. ; EPICIER, TH: Superlubricity of MoS₂: crystal orientation mechanisms. In: *Surface and Coatings Technology* Bd. 68–69, Elsevier (1994), Nr. C, S. 427–432
- [77] FLEISCHAUER, PAUL D. ; BAUER, REINHOLD: Chemical and structural effects on the lubrication properties of sputtered MoS₂ films. In: *Tribology Transactions* Bd. 31, Taylor & Francis Group (1988), Nr. 2, S. 239–250
- [78] OVIEDO, JUAN PABLO ; KC, SANTOSH ; LU, NING ; WANG, JINGUO ; CHO, KYEONGJAE ; WALLACE, ROBERT M. ; KIM, MOON J.: In situ TEM characterization of shear-stress-induced interlayer sliding in the cross section view of molybdenum disulfide. In: *ACS Nano* Bd. 9, American Chemical Society (2015), Nr. 2, S. 1543–1551
- [79] LI, HE ; WANG, JINHUAN ; GAO, SONG ; CHEN, QING ; PENG, LIANMAO ; LIU, KAIHUI ; WEI, XIANLONG: Superlubricity between MoS₂ Monolayers. In: *Advanced Materials* Bd. 29, Wiley-VCH Verlag (2017), Nr. 27
- [80] ONODERA, TASUKU ; MORITA, YUSUKE ; NAGUMO, RYO ; MIURA, RYUJI ; SUZUKI, AI ; TSUBOI, HIDEYUKI ; HATAKEYAMA, NOZOMU ; ENDOU, AKIRA ; U. A.: A computational chemistry study on friction of h-MoS₂. Part II. Friction anisotropy. In: *Journal of Physical Chemistry B* Bd. 114, American Chemical Society (2010), Nr. 48, S. 15832–15838
- [81] SPEAR, JESSICA C ; EWERS, BRADLEY W ; BATTEAS, JAMES D: ScienceDirect 2D-nanomaterials for controlling friction and wear at interfaces. In: *Nano Today* Bd. 10 (2015), S. 301–314
- [82] LEE, CHANGGU ; LI, QUNYANG ; KALB, WILLIAM ; LIU, XIN ZHOU ; BERGER, HELMUTH ; CARPICK, ROBERT W. ; HONE, JAMES: Frictional characteristics of atomically thin sheets. In: *Science* Bd. 328, Science (2010), Nr. 5974, S. 76–80
- [83] LAVINI, FRANCESCO ; CALÒ, ANNALISA ; GAO, YANG ; ALBISETTI, EDOARDO ; LI, TAI DE ; CAO, TENGFEI ; LI, GUOQING ; CAO, LINYOU ; U. A.: Friction and work function oscillatory behavior for an even and odd number of layers in polycrystalline MoS₂. In: *Nanoscale* Bd. 10, Royal Society of Chemistry (2018), Nr. 17, S. 8304–8312

- [84] PEARSON, KRISTIN: Materials Data on MoS₂ (SG:194) by Materials Project (2016)
- [85] WANG, SHANSHAN ; RONG, YOUJIN ; FAN, YE ; PACIOS, MERCE ; BHASKARAN, HARISH ; HE, KUANG ; WARNER, JAMIE H.: Shape evolution of monolayer MoS₂ crystals grown by chemical vapor deposition. In: *Chemistry of Materials* Bd. 26, American Chemical Society (2014), Nr. 22, S. 6371–6379
- [86] DE YOREO, J. J.: Principles of Crystal Nucleation and Growth. In: *Reviews in Mineralogy and Geochemistry* Bd. 54, GeoScienceWorld (2003), Nr. 1, S. 57–93
- [87] DIETZEL, DIRK ; FELDMANN, MICHAEL ; SCHWARZ, UDO D. ; FUCHS, HARALD ; SCHIRMEISEN, ANDRÉ: Scaling laws of structural lubricity. In: *Physical Review Letters* Bd. 111, American Physical Society (2013), Nr. 23, S. 235502
- [88] ZHOU, YUZHONG ; KIRIYA, DAISUKE ; HALLER, E. E. ; AGER, JOEL W. ; JAVEY, ALI ; CHRZAN, D. C.: Compliant substrate epitaxy: Au on MoS₂. In: *Physical Review B* Bd. 93, American Physical Society (2016), Nr. 5, S. 054106
- [89] LU, JUNPENG ; LU, JIA HUI ; LIU, HONGWEI ; LIU, BO ; GONG, LILI ; TOK, ENG SOON ; LOH, KIAN PING ; SOW, CHORNG HAU: Microlandscaping of au nanoparticles on few-layer MoS₂ films for chemical sensing. In: *Small* Bd. 11, Wiley-VCH Verlag (2015), Nr. 15, S. 1792–1800
- [90] BUSCEMA, MICHELE ; BARKELID, MARIA ; ZWILLER, VAL ; VAN DER ZANT, HERRE S.J. ; STEELE, GARY A. ; CASTELLANOS-GOMEZ, ANDRES: Large and tunable photothermoelectric effect in single-layer MoS₂. In: *Nano Letters* Bd. 13, American Chemical Society (2013), Nr. 2, S. 358–363
- [91] GARCÍA, RICARDO ; TAMAYO, JAVIER ; SAN PAULO, ALVARO: Phase contrast and surface energy hysteresis in tapping mode scanning force microscopy. In: *Surface and Interface Analysis* Bd. 27, John Wiley & Sons Ltd (1999), Nr. 5, S. 312–316
- [92] LI, MENG ; SHI, JIALIN ; LIU, LIANQING ; YU, PENG ; XI, NING ; WANG, YUECHAO: Experimental study and modeling of atomic-scale friction in zigzag and armchair lattice orientations of MoS₂. In: *Science and Technology of Advanced Materials* Bd. 17, Taylor and Francis Ltd. (2016), Nr. 1, S. 189–199
- [93] PLIMPTON, STEVE: Fast parallel algorithms for short-range molecular dynamics. In: *Journal of Computational Physics* Bd. 117, Academic Press (1995), Nr. 1, S. 1–19
- [94] FOILES, S. M. ; BASKES, M. I. ; DAW, M. S.: Embedded-atom-method functions for the fcc metals Cu, Ag, Au, Ni, Pd, Pt, and their alloys. In: *Physical Review B* Bd. 33, American Physical Society (1986), Nr. 12, S. 7983–7991
- [95] FARMANBAR, MOJTABA ; BROCKS, GEERT: First-principles study of van der Waals interactions and lattice mismatch at MoS₂/metal interfaces. In: *Physical Review B* Bd. 93, American Physical Society (2016), Nr. 8, S. 085304
- [96] JU, WEIWEI ; LI, TONGWEI ; SU, XIANGYING ; LI, HAISHENG ; LI, XIAOHONG ; MA, DONGWEI: Au cluster adsorption on perfect and defective MoS₂ monolayers: Structural and electronic properties. In: *Physical Chemistry Chemical Physics* Bd. 19, Royal Society of Chemistry (2017), Nr. 31, S. 20735–20748
- [97] CAO, XING'AN ; GAN, XUEHUI ; LANG, HAOJIE ; YU, KANG ; DING, SHUYANG ; PENG, YITIAN ; YI, WANGMIN: Anisotropic nanofriction on MoS₂ with different thicknesses. In: *Tribology*

International Bd. 134, Elsevier Ltd (2019), S. 308–316

- [98] RODUNER, EMIL: Size matters: Why nanomaterials are different. In: *Chemical Society Reviews* Bd. 35, Royal Society of Chemistry (2006), Nr. 7, S. 583–592
- [99] ÖZOĞUL, ALPER ; TRILLITZSCH, FELIX ; NEUMANN, CHRISTOF ; GEORGE, ANTONY ; TURCHANIN, ANDREY ; GNECCO, ENRICO: Plowing-induced nanoexfoliation of mono-and multilayer MoS₂ surfaces. In: *Physical Review Materials* Bd. 4 (2020), Nr. 3, S. 2–7
- [100] WANG, XIAONAN ; TABARRAEI, ALIREZA ; SPEAROT, DOUGLAS E.: Fracture mechanics of monolayer molybdenum disulfide. In: *Nanotechnology* Bd. 26, Institute of Physics Publishing (2015), Nr. 17, S. 1–6

Acknowledgements

I have received tremendous support while conducting my research and during the finalization of this dissertation from academic advisors, colleagues, friends, and my family. I owe special thanks to:

- Prof. Dr. Enrico Gnecco, my supervisor, without whom this work could have never been realized. His continued support and enthusiasm in nanotribological issues gave me the chance to dive deeply into the field of nanoscience.
- Prof. Dr. Franciszek Krok and Arkadiusz Janas, for not only providing samples and measurements but also for being a constant partner throughout my whole time as a PhD student.
- Prof. Dr. Andrej Turchanin, Dr. Antony George and Christof Neumann, for spectacular samples and great discussions about new materials and research results.
- Dr. Roberto Guerra and Dr. Nicola Manini, for providing necessary simulations and insight in the modelled molecular systems.
- Prof. Dr. Carlos Pina, Dr. Carlos Pimentel and Dr. Patricia Pedraz Carrasco for a warm welcome to Madrid and inspiration during my research trip.
- Alper Özoğul, for constant support and help with any issue encountered on this long way, for reviewing sections of this work, and for being a true friend every single day.
- Anke Partschefeld, for always providing a place of rest and conversation.
- Finally, my wife Meighan, my parents and my dog Hazelene, for all the emotional support I ever needed, without I would have never finished this journey.

Eigenwörtliche Erklärung

Ich erkläre hiermit ehrenwörtlich, dass ich die vorliegende Arbeit selbständig, ohne unzulässige Hilfe Dritter und ohne Benutzung anderer als der angegebenen Hilfsmittel und Literatur angefertigt habe. Die aus anderen Quellen direkt oder indirekt übernommenen Daten und Konzepte sind unter Angabe der Quelle gekennzeichnet. Die nachstehend aufgeführten Personen haben mich bei der Auswahl und Auswertung unentgeltlich unterstützt:

- Prof. Dr. Franciszek Krok, Dr. Benedykt R. Jany und Arkadiusz Janas der Jagiellonen Universität Krakau durch Probenherstellung und Charakterisierung mit SEM, STM und HAADF STEM
- Prof. Dr. Andrej Turchanin, Dr. Antony George und Christof Neumann der Friedrich-Schiller-Universität Jena durch Probenherstellung
- Dr. Roberto Guerra und Dr. Nicola Manini der Universität Mailand durch MD Simulationen
- Prof. Dr. Enrico Gnecco und Alper Özoğul der Friedrich-Schiller-Universität Jena durch Beratung und Auswertung.

Weitere Personen waren an der inhaltlich-materiellen Erstellung der vorliegenden Arbeit nicht beteiligt. Insbesondere habe ich hierfür nicht die entgeltliche Hilfe von Vermittlungs- bzw. Beratungsdiensten (Promotionsberater oder andere Personen) in Anspruch genommen. Niemand hat von mir unmittelbar oder mittelbar geldwerte Leistungen für Arbeiten erhalten, die im Zusammenhang mit dem Inhalt der vorgelegten Dissertation stehen. Die Arbeit wurde bisher weder im In- noch im Ausland in gleicher oder ähnlicher Form einer anderen Prüfungsbehörde vorgelegt. Die geltende Promotionsordnung der Physikalisch-Astronomischen Fakultät ist mir bekannt. Ich versichere ehrenwörtlich, dass ich nach bestem Wissen die reine Wahrheit gesagt und nichts verschwiegen habe.

Jena, den 1.10.2020